UC San Diego
UC San Diego Electronic Theses and Dissertations

Title
Optical Frequency Comb Assisted Discrete Fourier Transform Processor

Permalink
https://escholarship.org/uc/item/1hw3v9qk

Author
Hu, Huan

Publication Date
2020

Peer reviewed|Thesis/dissertation

eScholarship.org Powered by the California Digital Library
University of California

UNIVERSITY OF CALIFORNIA SAN DIEGO

Optical Frequency Comb Assisted Discrete Fourier Transform Processor

A dissertation submitted in partial satisfaction of the requirements for the degree Doctor of Philosophy

in

Electrical Engineering (Photonics)

by

Huan Hu

Committee in charge:

Professor Stojan Radic, Chair
Professor Leonid Butov
Professor Miroslav Krstic
Professor Zhaowei Liu
Professor George Papen

2020

Copyright

Huan Hu, 2020

All rights reserved.

The Dissertation of Huan Hu is approved, and it is acceptable in quality and form for publication on microfilm and electronically:

Chair

University of California San Diego

2020

DEDICATION

To my father Pinghe Hu and my mother Xiyu Wan.

TABLE OF CONTENTS

SIGNATURE PAGE iii
DEDICATION iv
TABLE OF CONTENTS v
LIST OF FIGURES vii
LIST OF TABLES x
ACKNOWLEDGMENTS xii
VITA xv
ABSTRACT OF THE DISSERTATION xvi
Chapter 1 Introduction 1
1.1 Motivation 1
1.2 Dissertation structure 3
Chapter 2 Principles of Operation 5
2.1 Discrete Fourier Transform 6
2.2 Hybrid DFT Processor with Dual Combs 9
2.3 Comb Generation 12
2.4 Summary 14
Chapter 3 Demonstration of the Hybrid DFT Processor 15
3.1 Experimental impairments 16
3.2 DFT of sinc-shaped signal 21
3.3 DFT of BPSK signals 25
3.4 Summary 26
Chapter 4 Hybrid Broadband OFDM receiver 27
4.1 Principles of OFDM 28
4.2 OFDM receiver architecture 32
4.3 PPM signal demodulation 35
4.4 OFDM signal demodulation 38
4.5 Phase noise characteristics 39
4.6 Phase noise compensation 42
4.7 Summary 49
Chapter 5 Comb Assisted RF Receivers with Reduced Complexity 52

5.1 Hybrid DFT processor with variable frequency comb 52
5.2 Sub-Nyquist ultra-wideband sparse signal reception..... 67
5.3 Summary 82
Chapter 6 Conclusion..... 84
6.1 Future work 86
Chapter 7 Bibliography..... 90

LIST OF FIGURES

Figure. 2-1 (a) Spectral representation of a DFT processor with dual optical parametric combs. (b) Signal-LO pairs are separated by optical routers. Signal is down converted via coherent detection and sub-band filtering is done by detector element response bandwidth (δf). DC term (red circle) of the electrical signal is exactly the DFT coefficient f_{IF} at frequency f_{IF}. 10

Figure. 2-2 Optical parametric comb generation. MZM: Mach-Zehnder Modulator, PM: Phase modulator, PS: RF phase shifter, SMF: Single mode fiber, EDFA: Erbium doped fiber amplifier, HNLF: Highly nonlinear fiber, NOLM: Nonlinear optical loop mirror. 12

Figure. 2-3 25 GHz optical frequency comb spectrum. 14

Figure. 3-1 Optical DFT scheme for (a) parallel processing and (b) equivalent experimental setup with bandpass filter (BPF) and a single coherent detector. OFC_s and OFC_{LO} represent signal and LO optical frequency combs. 15

Figure. 3-2 Constellation of BPSK signal without/with I-Q skew. 18

Figure. 3-3 Schematic of a coherent receiver. 19

Figure. 3-4 Constellation of a sinusoidal signal before and after imbalance compensation. 21

Figure. 3-5 Transfer function of an MZM modulator biased at null point. Red line is the desired linear transfer function. 22

Figure. 3-6 Scheme of digital predistortion. The green triangle is an electrical amplifier. 23

Figure. 3-7 Waveform and spectrum of a time-limited sinc-shaped signal with and without predistortion. 24

Figure. 3-8 Spectrum recovery of the hybrid DFT processor for time-limited sinc-shape waveform. 25

Figure. 3-9 DFT computation of BPSK signal. (a) Input binary sequence of raised cosine shape. Red circle denotes the 25 points for DFT calculation. (b) Recovered 25-point DFT spectrum and (c) complex DFT coefficients. 26

Figure. 4-1 A comparison between FDM and OFDM. 29

Figure. 4-2 Block diagram of OFDM transmission system. S/P: serial to parallel conversion. P/S: parallel to serial conversion. D/A: digital to analog conversion. A/D: analog to digital conversion. 31

Figure. 4-3 Scheme of the hybrid DFT Processor. OFCs and OFC_{LO} are signal and LO optical frequency combs, respectively. I/Q: IQ optical modulator. MZM: Mach-Zehnder Modulator. WDM: Wavelength division multiplexer. S/H: Sample-and-hold circuit. ADC: Analog to digital converter. Each digitization block consists of 12 sample-and-hold units and a single ADC.... 32

Figure. 4-4 Spectrum of signal OFC. The spectral resolution is 0.02 nm..... 33

Figure. 4-5 (a) Recovered complex DFT coefficients from 6.8 GHz to 9.6 GHz of 503 identical symbols (blue dots). Red circle shows the DFT coefficients of the transmitted symbol. (b) Comparison of transmitted and DFT recovered waveform of a single symbol and (c) 20 symbols which has random pulse positions. (d) BER performance from experiments and simulation. . 36

Figure. 4-6 (a) Correlation matrix of phase noise over all 60 channels. (b) Variance of phase noise of each channel indicates a quadratic scaling over comb mode order. Channel 21 corresponds to the zero-order comb mode. Phase noise was measured at 19.8 dB SNR condition. 41

Figure. 4-7 Constellation of the 60th (15.8 GHz) channel before (left) and after (right) phase noise compensation with phase error on the 59th channel. (b) EVM of all 60 channels before and after phase noise compensation in a sequential nulling process. 44

Figure. 4-8 Error vector magnitude of comb-assisted OFDM receiver with sequential nulling method and pilot channels method compared to a back-to-back measurement and theory..... 47

Figure. 4-9 (a) two stage joint phase estimation scheme. $\Delta\theta i$ represents the phase noise estimation of i-th channel. (b) phase noise estimation of a symbol over all 60 channels. Blue line is phase estimated by Viterbi-Viterbi (V-V) and red line is estimated with V-V with cycle slip correction (V-V CSC). The yellow curve represents the true phase error for that symbol.48

Figure. 5-1 Spectral representation of a DFT processor with dual optical parametric combs.. 54

Figure. 5-2 (a) Optical parametric comb generation. (b) Output comb spectrum with 25 GHz and 24.9 GHz frequency pitch sharing the same setup except for a different clock. The spectral resolution is 0.02 nm and is measured at 1% tap..... 57

Figure. 5-3 Setups of variable frequency comb assisted OFDM receiver.. 60

Figure. 5-4 5.5GHz channel reception. (a) Recorded in-phase part of frequency shifted signal within a switch period. (b) captured effective DFT coefficients (left) and complex conjugate DFT coefficients (right) within 198 μs. (c) A recovered OFDM symbol waveform with captured DFT coefficients from 3GHz to 7.9GHz..... 63

Figure. 5-5 (a) EVM and (b) output SNR performance of OFDM receiver using a variable comb at various SNR conditions..... 65

Figure. 5-6 (a)Spectral representation of a DFT processor with dual optical frequency combs. (b) compressive sensing model illustration with $K = 2$ nonzero values in support s. 71

Figure. 5-7 Output comb spectrum with 25 GHz and 24.9 GHz frequency pitch sharing identical setup except for driving clock. The spectral resolution is 0.02 nm and is measured at 1% tap. OSNR is more than $40dB_{0.1nm}$. 74

Figure. 5-8 Setups of variable frequency comb assisted CS receiver. 75

Figure. 5-9 Sparse signal recovery of identical symbols. (a)50 complex DFT coefficients of identical symbols within a frequency toggling period with sparsity $K = 2$. (b) support recovery with only 17 randomly chosen DFT coefficients. (c) waveform recovery with the 17 DFT coefficients selected in (b). 77

Figure. 5-10 Simulated mean square error (MSE) of the recovered waveform from proposed CS receiver at various SNR and number of DFT coefficients (M) for sparsity (a) $K = 2$ and (b) $K = 4$ respectively. 79

Figure. 5-11 Simulated mean square error (MSE) of the recovered waveform from proposed CS receiver at various sparsity (K) and number of DFT coefficients (M). SNR is fixed at 20dB.. 80

Figure. 5-12 Mean square error (MSE) vs. number of DFT coefficients for recovered signals of different sparsity (K). Solid lines indicate experimental results and dashed lines are from Monte Carlo simulations. 81

LIST OF ABBREVIATIONS

ADC	Analog to digital converter
ASIC	Application-specific Integrated Circuits
AWG	Arbitrary waveform generator
CS	Compressed sensing
CW	Continuous wave
DAC	Digital to analog converter
DC	Direct current
DFT	Discrete Fourier Transform
DSP	Digital Signal Processing
FFT	Fast Fourier Transform
FPGA	Field Programmable Gate Arrays
FWM	Four Wave Mixing
HNLF	Highly nonlinear fiber
IDFT	Inverse Discrete Fourier Transform
IF	Intermediate frequency
IFFT	Inverse Fast Fourier Transform
IoT	Internet of things
LO	Local oscillator
MZM	Mach-Zehnder modulator
OFC	Optical frequency comb
OFDM	Orthogonal Frequency Division Multiplexing
OSNR	Optical signal to noise ratio
PAPR	Peak-to-average ratio
PM	Phase modulator
QAM	Quadrature-amplitude modulation
RF	Radiofrequency

SMF	Single-mode fiber
UWB	Ultrawide band
V-V	Viterbi-Viterbi
WDM	Wavelength division multiplexing

ACKNOWLEDGMENTS

I am grateful to all the people who offered help and inspiration.

First and foremost, I would like to express my deepest gratitude to my dissertation advisor, Prof. Stojan Radic, for his continuous support and guidance on research and life. As an intelligent and open-minded researcher, his passion and insight motivate me to explore new ideas and take on all the challenges. Despite getting rigorous academic training under his supervision, inspired by his encouragement and endless support, I learn the way to think independently and stay focused in complicated scenarios and tough times. Besides, I sincerely appreciate his consideration and understanding for my long-term career. I would also like to thank all my committee members: Professor Leonid Butov, Professor Miroslav Krstic, Professor Zhaowei Liu and Professor George Papen, for their constructive discussions and contributions into this dissertation.

I have been working in the Photonic Systems Group for the last five years and I truly feel lucky to work with people of intelligence, diligence and willingness to help. I want to thank Dr. Vahid Ataie, for guiding me to get started in this new research field of photonic systems. His highly efficient working style is impressive and motivates me to develop good habits to work and study. I would also like to acknowledge Dr. Daniel Esman and Dr. Eduardo Temprana for their hands-on support from operation of devices to code debugging. Indeed, as senior PhD students, they frequently set up “daily quiz” to help me review and gain an in-depth understanding of the basics related to my projects, helping me build a solid foundation for the following years. I must express my gratitude to Dr. Bill P.-P. Kuo, not only for his professional guidance, but also for sharing his own experience on research and life attitude. His advice eliminated my confusion and inspired me during the long journey towards a PhD degree. I want to thank Dr. Nikola Alic, for his support

on lab management, valuable academic discussions, and the laugh and joy he brought to the lab with his sense of humor. I also want to thank Dr. Evgeny Myslivets, who has extensive theoretical and experimental experience, for providing me countless help on every aspect of optical combs and systems. Thanks to Jin Zhang and Dr. Liangshun Han for their detailed explanation of silicon photonics and helpful discussions on career plans. A special thanks is to my friend and colleague Junshan Leng for his accompany, assistance and food, thus saving me from getting bored and starving in long-term experiments, especially in those late nights in the lab. Also, I would like to thank both past and present members of the lab for their source of encouragement and constructive comments: Dr. Andreas O. J. Wiberg, Dr. Ana Pejkic, Motohiko Eto, Elham Serahati, Nanzhe Hu, Dr. Kevin Young, Dr. Chris Huynh and Dr. Lan Liu.

Here, I would like to extend my appreciation to the friends outside of the lab for their help and support during this long journey: Youbin Mo, Yingwei Li, Dr. Jimeng Zheng, and many others not mentioned here.

Finally, I would like to thank my parents, mother Xiyu Wan and father Pinghe Hu, and my girlfriend Yuhong Chen, for their sacrifice, love and support.

Chapter 3, in part, is a reprint of the materials as it appears in *Optical Fiber Communication Conference (2017)* titled “Comb-assisted real-time Discrete Fourier Transform processor” authored by Huan Hu, Daniel Esman, Vahid Ataie, Eduardo Temprana, Bill Kuo, Nikola Alic and Stojan Radic. The dissertation author was the primary investigator and the primary author of this article.

Chapter 4, in part, is a reprint of the materials as it appears in *Journal of Lightwave Technology* volume 37, issue 4, 1280-1287 (2019), titled “Realtime comb-assisted discrete

Fourier transform processor" authored by Huan Hu, Vahid Ataie, Evgeny Myslivets, and Stojan Radic. The dissertation author was the primary investigator and the primary author of this article.

Chapter 4, in part, is a reprint of the materials as it appears in *Conference on Lasers and Electro-Optics Pacific Rim (2018)* titled "Realtime comb-assisted discrete Fourier transform processor" authored by Huan Hu, Vahid Ataie, Evgeny Myslivets, and Stojan Radic. The dissertation author was the primary investigator and the primary author of this article.

Chapter 4, in part, is a reprint of the materials currently being submitted for publication as it may appear in the IEEE Photonics Technology Letters, titled "Joint Phase Noise Compensation in Dual-comb Assisted OFDM Receiver" authored by Huan Hu, and Stojan Radic. The dissertation author was the primary investigator and the primary author of this article.

Chapter 5, in part, is a reprint of the materials as it appears in *Optics Express* volume 28, issue 4, 5658 (2020), titled "Hybrid OFDM receiver assisted by a variable frequency comb" authored by Huan Hu and Stojan Radic. The dissertation author was the primary investigator and the primary author of this article.

Chapter 5, in part, is a reprint of the materials as it appears in IEEE/OSA *Journal of Lightwave Technology* early access (2020), titled "Sub-Nyquist Ultra-wideband Sparse Signal Reception via Variable Frequency Comb" authored by Huan Hu and Stojan Radic. The dissertation author was the primary investigator and the primary author of this article.

VITA

2008 - 2012	Bachelor of Science in Physics,
	University of Science and Technology of China, China
2012 - 2014	Master of Science in Electrical and Computer Engineering,
	University of Alberta, Canada
2014 - 2020	Doctor of Philosophy in Electrical Engineering (Photonics),
	University of California San Diego, USA

PUBLICATIONS

Journal Articles:

Huan Hu and Stojan Radic, "Joint Phase Noise Compensation in Dual-comb Assisted OFDM Receiver." (submitted).

Huan Hu and Stojan Radic, "Sub-Nyquist Ultra-wideband Sparse Signal Reception via Variable Frequency Comb." Journal of Lightwave Technology (2020).

Huan Hu and Stojan Radic, "Hybrid OFDM receiver assisted by a variable frequency comb," Opt. Express 28, 5658-5668 (2020).

Huan Hu, Vahid Ataie, Evgeny Myslivets, and Stojan Radic, "Optical Comb Assisted OFDM RF Receiver," Journal of Lightwave Technology 37(4), 1280-1287 (2019).

Conference Proceedings:

Huan Hu, Vahid Ataie, Evgeny Myslivets, and Stojan Radic, "Realtime comb-assisted discrete Fourier transform processor." In 2018 Conference on Lasers and Electro-Optics Pacific Rim (CLEO-PR), pp. 1-2. IEEE, 2018.

Huan Hu, Daniel Esman, Vahid Ataie, Eduardo Temprana, Bill P-P. Kuo, Nikola Alic, and Stojan Radic, "Comb-assisted real-time discrete Fourier transform processor." In 2017 Optical Fiber Communications Conference and Exhibition (OFC), pp. 1-3. IEEE, 2017.

ABSTRACT OF THE DISSERTATION

Optical Frequency Comb Assisted Discrete Fourier Transform Processor

by

Huan Hu

Doctor of Philosophy in Electrical Engineering (Photonics)

University of California San Diego, 2020

Professor Stojan Radic, Chair

Discrete Fourier transform (DFT) has been one of the most fundamental tools in signal and image processing. With increasing demand of data traffic for applications such as media streaming, 5G communication and internet of things (IoT), broadband backend receivers require high performance DFT cores to meet the performance target. However, due to the tradeoff between bandwidth and precision of electronic digitizers and fundamentally limited computation capability of conventional silicon processors, it is challenging to perform DFT computation on broadband signals with all-electronic DFT processors. In this dissertation a new hybrid DFT processor relying on phase locked optical combs are introduced to circumvent these challenges.

The proposed processor combines signal digitization and DFT computation in a computation-free manner, and outputs complex DFT coefficients of broadband radio-frequency (RF) signals with high throughput, high precision and low power dissipation. Its capabilities are thoroughly demonstrated in a broadband orthogonal-frequency-division-multiplexing (OFDM) receiver. OFDM receivers are sensitive to phase noise, especially for signals with quadrature amplitude modulation (QAM). To improve the processing performance, several signal processing techniques are proposed and verified for phase noise suppression. To reduce the system complexity of the proposed DFT processor, a split-and-delay topology utilizing a single variable-pitch comb rather than two distinct phase-locked combs, could be used for DFT operation and is demonstrated in an OFDM receiver. In broadband RF signal reception, when a signal is sparse, using only a subset of captured high precision DFT coefficients is sufficient to fully capture the broadband signal. Without using high bandwidth electronic front-end, the new receiver operates in sub-Nyquist rate and eliminates main contributions to electronic noise and jitter in conventional techniques.

Chapter 1 Introduction

1.1 Motivation

We are in the data explosion era and have witnessed the exponentially growing demand for data traffic in applications such as media streaming, 5G communication and IoT. For example, global smartphone traffic increased by more than 50% per year[1] in recent years. In order to meet the performance targets of future mobile broadband systems, increase in spectrally efficient modulation formats such as orthogonal frequency division multiplexing (OFDM) will be adopted and high throughput DFT processor is required. Discrete Fourier transform has been one of the most fundamental tools in signal and image processing. Apart from serving as the processing core in OFDM communication systems, DFT has enabled powerful and efficient digital signal processing (DSP) algorithms for broadband communication systems such as time synchronization, signal detection, etc. In these applications, broadband RF signals must be digitized first and then processed in digital DFT processors.

Future high-performance signal processing demands progressively high data throughput, high precision and low dissipation DFT processor. Conventionally, high-rate, high-precision digital discrete Fourier processors are implemented in field-programmable gate arrays (FPGAs) and Application-specific integrated circuits (ASICs) platforms. However, as these also demand progressively higher data throughput and lower dissipation, the conventional (all-electronic) DFT processor faces both fundamental and practical challenges. Firstly, silicon DFT processor faces computation limit inherent with maximal transistor density, imposed by quantum and thermal effects [2]. This limit widely recognized after the breakdown of Moore's Law and Dennard scaling, has served as one of the principal motivations for renewed interest in

physically assisted processor topologies. In addition to a need for fast DFT processors, broadband RF receiver also mandates that received waveform is digitized by a full-rate analog-to-digital converter (ADC), which imposes basic dissipation limitations and requires a tradeoff between speed and quantization precision[3].

To address the first challenge, real-time DFT computation burden can be offloaded from electrical to optical domain. Several optical Fourier transform schemes have been proposed and include physically-generated DFT coefficients using dispersion management [4]–[6], cascaded delay interferometers [7] and arrayed waveguide grating routers [8], [9]. Recently, a silicon photonics DFT architecture was proposed to generate Fourier coefficients via mesh of on-chip Mach–Zehnder interferometers and phase shifters [10]. While such techniques offer a promise for high-capacity DFT operation, their precision remains limited and is accompanied by escalating structural complexity when DFT expansion grows. Consequently, these limitations prevent their practical use in both general and scalable DFT applications.

To address the second (quantization) challenge, RF channelized receivers were developed to map broadband signal onto narrow frequency bins via multiple filter banks and sampled with sub-rate ADC array[11]. However, such technique has its own set of implementation and performance challenges: increased noise due to a need for sub-rate tributary split and high filter isolation required to minimize signal leakage across the band. The bandpass output can also be frequency translated to the baseband via mixing with local oscillator (LO) signals, to allow for a single-stage lowpass filtering[12], but imposing the challenges of multiple LO synthesis and spurious mixing management. Alternatively, one can map high-bandwidth signal by quantizing it at full rate by photonically-assisted ADC[13]–[16]. However, even in photonically assisted quantizers capable of full-rate sampling, quantized signal still needs to be

mapped to the electronic domain. Ultimately, the performance trade-off is set by the precision of electronic ADC backplane and total number of (optical) sub-rate tributaries. In practical terms, by selecting higher resolution electronic ADC backplane, one necessarily increases the number of tributaries, increasing the complexity of the entire processor.

To address these concerns, in this dissertation a hybrid DFT processor based on dual phase-locked optical frequency combs was proposed and demonstrated in conjunction with high-throughput, high-precision architecture.

1.2 Dissertation structure

This dissertation designs, implements and tests a hybrid DFT processor relying on phase-locked optical frequency combs and experimentally demonstrates its applications in broadband RF signal reception and demodulation.

Starting with DFT computation in electronic domain, Chapter 2 introduces the operation principles of the hybrid DFT processor using dual phase-locked optical frequency combs. The performance of the DFT processor relies on generating mutually coherent combs with sufficiently high power, OSNR, high-frequency stability, and tone pitch tunability. The principles of optical parametric combs generation through shockwave engineering and the related theoretical background are introduced in this chapter.

Chapter 3 introduces the experimental implementation of the hybrid DFT processor and its performance characterization. The proposed DFT processor is a hybrid system consisting of both optical and electronic components and faces various practical impairments. To improve the performance of the DFT processor, detailed experimental impairment analysis and the corresponding compensation techniques are discussed to achieve high speed and flexible DFT computation.

With the hybrid DFT processor, an OFDM receiver is proposed and implemented in Chapter 4. The new OFDM receiver eliminates the need for high-speed ADCs and digital DFT processors in conventional architectures and capable of generating DFT coefficients of wideband RF signals in real-time. The performance is characterized by demodulation of a 4-QAM OFDM signal with 60 subcarriers positioned within 4 GHz - 15.8 GHz band and separated by 200MHz. It was observed that phase noise caused significant performance degradation in OFDM systems so that both blind and pilot-aided algorithms were developed for phase noise suppression. Besides, by further exploring the correlation of phase noise over different channels, a joint phase noise suppression algorithm is introduced for improved demodulation performance.

While the hybrid DFT processor is powerful for DFT computation with high throughput and high precision, the implementation is complex and costly. Chapter 5 focuses on reducing the hardware complexity of the hybrid DFT processor. Firstly, a new implementation scheme using split-and-delay topology is introduced and a single variable frequency comb, instead of dual frequency combs, can be used for DFT computation. It is experimentally demonstrated as a wideband OFDM receiver and realizes the equivalent of dual-comb assisted OFDM receiver operation. Secondly, when this DFT engine is used in a physically assisted wideband receiver, a subset of DFT coefficients is sufficient for sparse RF signal reception combined with compressed sensing algorithms, significantly reducing the hardware complexity in terms of optical carriers and coherent receivers.

Finally, Chapter 6 summarizes this dissertation and discusses future work.

Chapter 2 Principles of Operation

Fourier transform is one of the most important and powerful techniques in signal and image processing. A signal can be represented in frequency domain and this representation basically involves the decomposition of the signals in terms of exponential components. One of the most famous frequency decomposition experiments is to use a prism to break up white light into the colors of the rainbow, which is described by a paper from Isaac Newton in 1672. From physics we know that each color corresponds to a specific frequency of the visible spectrum, hence the analysis of light into colors is actually a form of frequency decomposition. Apart from its application in mathematics such as solving differential equations, Fourier transform offers an alternative perspective of signal in the frequency domain and eases the computation and implementation of signal processing algorithms.

Most of the signals encountered in science and engineering are analog in nature, which are represented as functions of a continuous variable such as time, and usually take on values in a continuous range. Considering an analog signal $x_a(t)$. The Fourier transform of $x_a(t)$ is

$$X_a(f) = \int_{-\infty}^{\infty} x_a(t) e^{-j2\pi f t} dt \tag{2.1}$$

such that $x_a(t)$ can be decomposed in the frequency domain, i.e. $x_a(t) = \int_{-\infty}^{\infty} X_a(f) e^{j2\pi f t} df$. The existence of Fourier transform requires that $x_a(t)$ has finite energy; that is $\int_{-\infty}^{\infty} |x_a(t)|^2 dt < \infty$. The signal can be of finite duration and extend its definition by zero-padding. Though signals can be processed directly by appropriate analog systems such as a prism for white light, modern signal processing techniques use an alternative way for signal processing for flexibility and accuracy considerations. Analog signals are quantized by analog-

to-digital converters (ADCs). Then digital processors are then used to process the digital signals and produce required information in digital domain. If the required output is in analog domain, digital-to-analog converters (DACs) are used to convert the processed digital signals to analog domain.

2.1 Discrete Fourier Transform

Frequency domain representation of a quantized discrete signal can be retrieved with discrete Fourier transform (DFT). Suppose a time-limited signal $x_a(t)$ is sampled at the sampling frequency F_s and represented as a discrete-time signal $x[n] = x(nT), n = 0, 1, 2 \ldots, N-1$ where $T = 1/F_s$ is the sampling interval and N is the length. The Fourier transform of $x[n]$ is

$$X(f) = \sum_{n=0}^{N-1} x[n] e^{-j2\pi n f/F_s}, 0 \leq f \leq F_s \tag{2.2}$$

which is the spectrum of discrete signal $x[n]$. The definition interval is limited by F_s due to the fact that $X(f)$ is actually periodic with periodicity F_s such that $X(f)$ at any frequencies exceeding $[0, F_s]$ can be retrieved with the equation (2.2). Notice that $X(f)$ is generally not equal to the spectrum $X_a(f)$ unless the sampling frequency F_s is larger than twice the signal bandwidth B, which is required by the Nyquist sampling theory. If $F_s < 2B$, then spectrum $X(f)$ contains the aliased frequency components of $X_a(f)$ and aliasing effect prevents it from recovering the original signal $x_a(t)$ with the discrete samples $x[n]$. In the absence of aliasing,

$$X_a(f) = \begin{cases} \frac{1}{F_s} X(f), & |f| \leq F_s/2 \\ 0 & |f| > F_s/2 \end{cases} \tag{2.3}$$

and frequency information of an analog signal $x_a(t)$ can be fully captured with discrete samples $x[n]$. When $X(f)$ is sampled at equally spaced frequencies $f = \frac{k}{N}F_s, k = 0, 1, 2, \dots, N-1$, the resultant samples are

$$X[k] = \sum_{n=0}^{N-1} x[n]e^{-j2\pi kn/N}, k = 0, 1, 2, \dots, N-1 \tag{2.4}$$

$\{X[k], k = 0, 1, 2, \dots, N-1\}$ is called discrete Fourier transform (DFT) of $\{x[n], n = 0, 1, 2, \dots, N-1\}$. $X[k]$ represents frequency sampling of the original analog signal $x_a(t)$. With $X[k]$ it is able to recover the sequence $x[n]$ with inverse discrete Fourier transform (IDFT)

$$x[n] = \sum_{k=0}^{N-1} X[k]e^{j2\pi kn/N}, n = 0, 1, 2, \dots, N-1 \tag{2.5}$$

In matrix representation, the DFT is represented as

$$\boldsymbol{X}_N = \boldsymbol{W}_N \boldsymbol{x}_N \tag{2.6}$$

where

$$\boldsymbol{x}_N = \begin{bmatrix} x[0] \\ x[1] \\ \vdots \\ x[N-1] \end{bmatrix}, \boldsymbol{X}_N = \begin{bmatrix} X[0] \\ X[1] \\ \vdots \\ X[N-1] \end{bmatrix},$$

$$\boldsymbol{W}_N = \begin{bmatrix} 1 & 1 & 1 & \cdots & 1 \\ 1 & W_N & W_N^2 & \cdots & W_N^{N-1} \\ 1 & W_N^2 & W_N^4 & \cdots & W_N^{2(N-1)} \\ \vdots & \vdots & \vdots & \vdots & \vdots \\ 1 & W_N^{N-1} & W_N^{2(N-1)} & \cdots & W_N^{(N-1)(N-1)} \end{bmatrix}, W_N = e^{-j2\pi/N} \tag{2.7}$$

The IFFT can be represented as

$$\boldsymbol{x}_N = \boldsymbol{W}_N^{-1}\boldsymbol{X}_N = \frac{1}{N}\boldsymbol{W}_N^{*}\boldsymbol{X}_N \tag{2.8}$$

In digital domain, DFT and IDFT are usually not computed directly. Instead, they are computed in much more efficient ways using fast Fourier transform (FFT) algorithms. The most commonly used FFT is the Cooley-Tukey algorithm. Assume FFT points N is a power of 2, from the definition of the DFT:

$$\begin{aligned} X[k] &= \sum_{n=0}^{N-1} x[n] W_N^{kn} \\ &= \sum_{m=0}^{\frac{N}{2}-1} x[2m] W_N^{2mk} + \sum_{m=0}^{\frac{N}{2}-1} x[2m+1] W_N^{(2m+1)k} \end{aligned} \tag{2.9}$$

Since $W_N^2 = W_{N/2}$, $X[k]$ can be expressed as:

$$\begin{aligned} X[k] &= \sum_{m=0}^{\frac{N}{2}-1} f_1[m] W_{\frac{N}{2}}^{mk} + W_N^k \sum_{m=0}^{\frac{N}{2}-1} x[2m+1] W_{\frac{N}{2}}^{mk} \\ &= F_1[k] + W_N^k F_2[k] \end{aligned} \tag{2.10}$$

where $F_1[k]$ and $F_2[k]$ are the $N/2$-point DFTs of the sequence $f_1[m]$ and $f_2[m]$ respectively.

The computation of N-point DFT requires N^2 complex multiplications. So the computation of $X[k], k = 0, 1, 2, \ldots, N-1$ with Eq. (2.10) requires two $N/2$-point DFT and additional N multiplication, which in total is $\frac{N^2}{4} \cdot 2 + N \sim \frac{N^2}{2}$. It is obvious that by dividing the original problem of computing N-point DFT into subproblem of computing $N/2$-point DFT, the complexity is reduced by half. By using such a divide-and-conquer method, the computation of DFT complexity finally reduced to $O(NlogN)$. This is so called the radix-2 FFT algorithm and a variety of other algorithms are proposed for FFT computation. An excellent introduction can be found in [17].

2.2 Hybrid DFT Processor with Dual Combs

Digital signal processing is generally preferred due to the flexibility and accuracy considerations. However, the performance of such digital signal processing scheme relies on ADCs and digital signal processors. Processing of signals with extremely wide bandwidths requires fast sampling rate ADCs and fast digital signal processors. For DFT computation, even using computation efficient FFT algorithms, the conventional, all-electronic DFT processors face both fundamental and practical challenges. Firstly, an all-electronics processor's throughput faces clock frequency scaling and maximal gate density restriction imposed by quantum and thermal effects [2], ultimately setting the upper bound for silicon processor speed. Secondly, due to a well-known tradeoff between speed and precision of the front-end quantizer [3], the precision of the all-electrical DFT computation will ultimately be limited at high throughputs, even if one resorts to high-rate, high-dissipation ADC. Indeed, while it is possible to map high-bandwidth signal by first quantizing it at full rate by photonically-assisted ADC[13], [14], [16], [18] and subsequently computing DFT coefficients in real-time, this approach is still subject to basic limitations, both in terms of precision and dissipation. In photonically assisted ADC that supports full-rate sampling, a sampled and quantized signal still must be mapped to electronic plane and the ultimate trade-off is set by electronic ADC precision vs. number of sub-rate tributaries. By selecting high-resolution electronic ADC in the backplane, one necessarily chooses large number of tributaries, increasing the complexity of the processor backplane.

Photonically assisted architectures aimed at high-speed operation and low power consumption can offload major computational burden from all-electrical processor onto photonic domain. Several optical Fourier transform schemes have been proposed previously and were based on dispersion management [4]–[6], cascaded delay interferometers [7] or arrayed

waveguide grating routers [8], [9]. Recently, a silicon photonics based architecture has been proposed for optical DFT computation through mesh of on-chip Mach–Zehnder interferometers and phase shifters [10]. However, these techniques are either precision limited or suffer from escalating structural complexity when DFT expansion grows, preventing their use in both general and scalable DFT computations. To address these, a photonic-assisted DFT pre-processor based on a dual phase-locked optical parametric combs was introduced and was shown in conjunction with high throughput, high precision and low power consumption [19], indicating practical viability of for hybrid (optoelectronic) architecture.

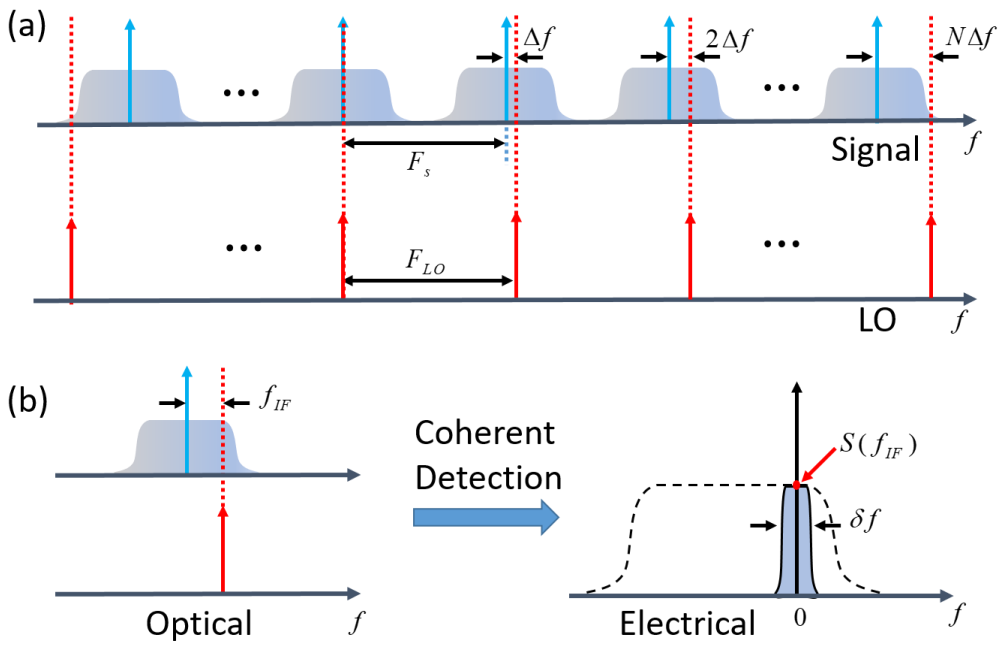

Figure. 2-1 (a) Spectral representation of a DFT processor with dual optical parametric combs. Blue and red arrows are the tones of signal comb and LO comb respectively. (b) Signal-LO pairs are separated by optical routers. Signal is down converted via coherent detection and sub-band filtering is done by detector element response bandwidth (δf). DC term (red circle) of the electrical signal is exactly the DFT coefficient $\mathbf{S}(f_{IF})$ at frequency f_{IF}.

With aid of dual, mutually coherent and frequency-Verniered combs, complex DFT coefficients of either optical or electrical signal can be extracted via parallel, sub-rate heterodyne detection[20], as illustrated in Figure. 2-1. When signal $s(t)$ is modulated onto optical comb

with frequency pitch F_s, a spectral copy is imposed on each comb tone. When comb tones possess sufficiently high optical signal-to-noise ratio (OSNR) and when modulation occurs in linear regime, it is possible to approximate signal copying by noiseless, distortion-free replication in spectral domain. The second, phase-locked comb, acts as a local oscillator (LO) array, possessing a different frequency pitch F_{LO} in order to accomplish spectral Vernier. Each signal-LO comb mode pair can be optically filtered by a wavelength division demultiplexer that has matched, coarse frequency grid and sent to a dedicated, sub-rate coherent detector. Consequently, each detector element will retrieve spectral information at targeted frequency offset, defined by the comb pitch offset $f_{IF} = n \cdot \Delta f$, where n is order number and Δf is frequency pitch offset ($F_{LO} - F_s$). A coherent detection of each comb mode pair is equivalent to heterodyne detection of a RF signal copy, resulting in frequency-shifted baseband signal $s(t)e^{-j2\pi f_{IF}t}$, filtered by the detector response. DFT coefficient $\boldsymbol{S}(f_{IF})$ centered at f_{IF} can be retrieved with a lowpass filter, effectively realized by the detector element response $\delta f (\geq \Delta f)$. As a result, the backplane is composed of sub-rate ADC array, rather than full-rate ADCs. This allows for ADC array precision can be qualitatively increased, enabling alias-free $\boldsymbol{S}(f_{IF})$ acquisition with low-complexity DSP. By capturing a complete set of signal-LO pairs, the recovery of the full-band spectrum $\boldsymbol{S^{full}}(f)$ is guaranteed with frequency domain sampling resolution set by the frequency pitch offset Δf.

Comb-assisted processor significantly relieves the complexity of DFT computation since it eliminates front-end quantization and full-rate, multiplicative implementation of conventional fast Fourier transform (FFT) algorithms [21]–[23]. Firstly, selected tones can be filtered simultaneously for parallel heterodyne detection so that DFT computation is effectively parallelized, enabling the rate scaling of the aggregate throughput. Secondly, only sub-rate of

the detected signal is needed, allowing for a low-rate ADC backplane with correspondingly high resolution. Thirdly, if optical-signal-to-noise ratio (OSNR) of the signal and LO combs are sufficiently high, an effective precision of DFT generation will be maintained. Finally, when comb pitch can be freely tuned, resolution and frequency range of DFT decomposition can be freely chosen and reconfigured in order to meet the input signal requirements. This is particularly important in flexible-band applications, where users should be able to change center frequency and instantaneous bandwidth in a rapid manner.

2.3 Comb Generation

The performance of DFT processor relies on generating mutually coherent combs with sufficiently high power and OSNR. Additionally, to guarantee the processor flexibility and performance, combs should have high frequency stability, and tone pitch tunability. Optical parametric combs generated through shockwave engineering combine all these attributes in a single, travelling-wave platform [24]. The principle of optical frequency comb generation at 25 GHz is introduced as follows (Figure. 2-2).

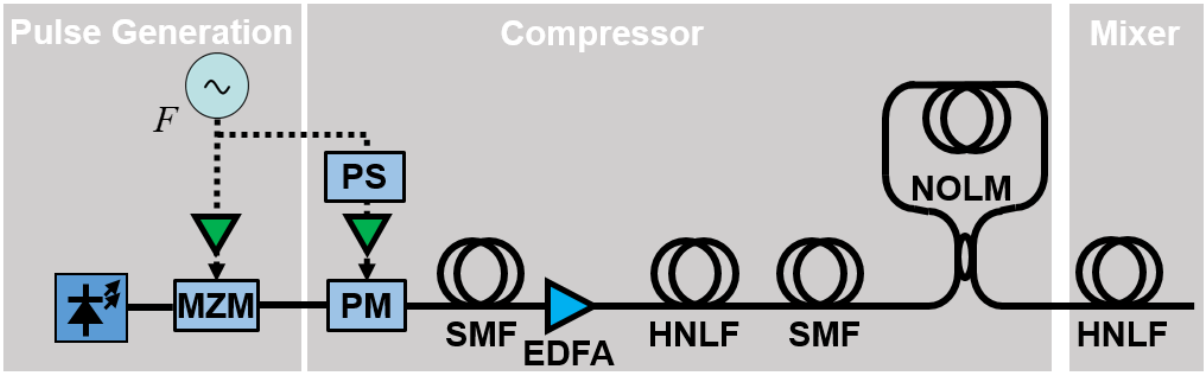

Figure. 2-2 Optical parametric comb generation. MZM: Mach-Zehnder Modulator, PM: Phase modulator, PS: RF phase shifter, SMF: Single mode fiber, EDFA: Erbium doped fiber amplifier, HNLF: Highly nonlinear fiber, NOLM: Nonlinear optical loop mirror.

With sufficient optical power and wideband phase matched condition, optical parametric combs are generated via four wave mixing (FWM) process over wide spectral range exceeding combined C and L band. To increase efficiency of FWM process in a mixer stage consisting of a highly nonlinear fiber (HNLF), shock wave with high peak power is created through a compressor stage which precisely manages initial frequency chirp and group velocity dispersion by controlling the phase modulation and physical properties of the fiber. Seed mixer pulses are initially generated modulating continuous-wave (CW) master laser by 25 GHz harmonic using a quadrature biased Mach-Zehnder modulator (MZM). A phase modulator (PM) driven by a half-wave delayed version of the modulation waveform induces a positive chirp and creates condition for subsequent compression. Negative single mode fiber (SMF) dispersion is tailored in order to take advantage of rising and falling pulse edges with differential group velocity. The narrow high-power pulse can be further compressed in a second compression stage. First, a positive Kerr-induced chirp is applied to the pulses in HNLF. Next, SMF with negative dispersion compress the pulses and create shockwaves with sufficient high peak power. The parasitic side lobes generated in this stage manifest as power fluctuations of the shockwaves and are suppressed by pulse shaping with a nonlinear optical loop mirror (NOLM). The compressed pulse is subsequently sent to the mixer stage consists of HNLF to generate broadband comb via efficient FWM. A coherently coupled comb can be generated in a similar fashion if the master CW laser is shared with identical mixer setup, but driven at a different frequency, guaranteeing high mutual coherence over all signal-LO tone pairs, which is essential for coherent detection in the backplane.

Figure. 2-3 illustrates the spectrum of an optical frequency comb generated through shockwave engineering spanning from 1525 nm to 1575 nm, fully covering C- and L- band in

optical communication. The power spectrum ripple is less than 3 dB and can be reduced down to less than 1 dB with fine tuning. The power per tone is around -6 dBm in this demonstration and can be boosted over 0 dBm within this setup and further boosted over 10 dBm combined with other techniques such as injection locking. The optical signal-to-noise-ratio (OSNR) is over 40dB defined within 0.1 nm bandwidth and the number of tones is more than 250.

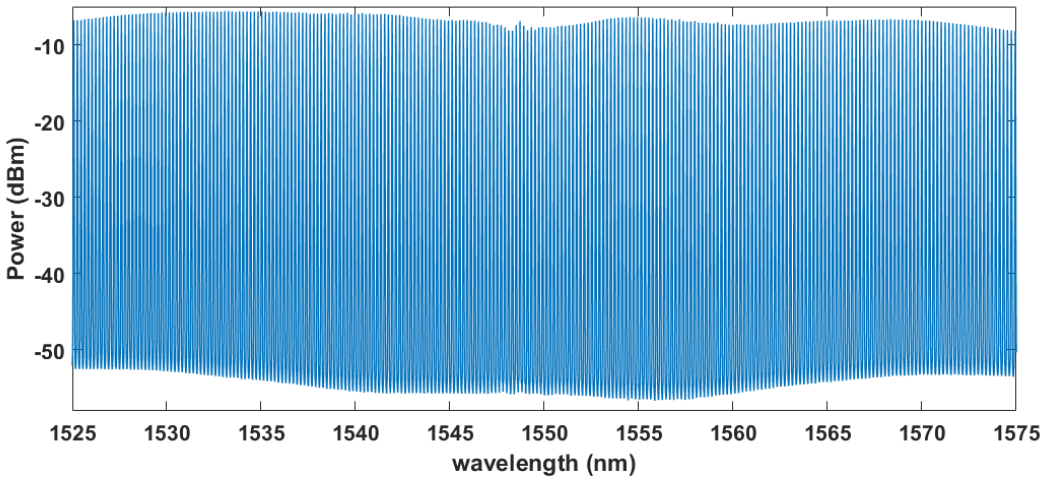

Figure. 2-3 25 GHz optical frequency comb spectrum.

2.4 Summary

At the start of this chapter concept of discrete Fourier transform (DFT) and its implementation in electronic signal processing systems are briefly introduced. Since high performance DFT processing requires high-speed ADCs and digital processors, which are the bottleneck of current electronic architectures, a novel hybrid opto-electronic DFT processor relies on dual mutual coherent combs is introduced and its principle of operation is discussed in Chapter 2.2. In the last, to make a high performance DFT engine, the principle of parametric optical frequency comb generation with shock-wave engineering is discussed in Chapter 2.3.

Chapter 3 Demonstration of the Hybrid DFT Processor

As discussed in Chapter 2, the hybrid DFT processor relies on two mutually coherent combs and it outputs complex DFT coefficients in a computation free manner. In this chapter experiments that directly demonstrate DFT operation of the proposed hybrid DFT processor are described. The detailed experimental setup and signal processing techniques will be covered.

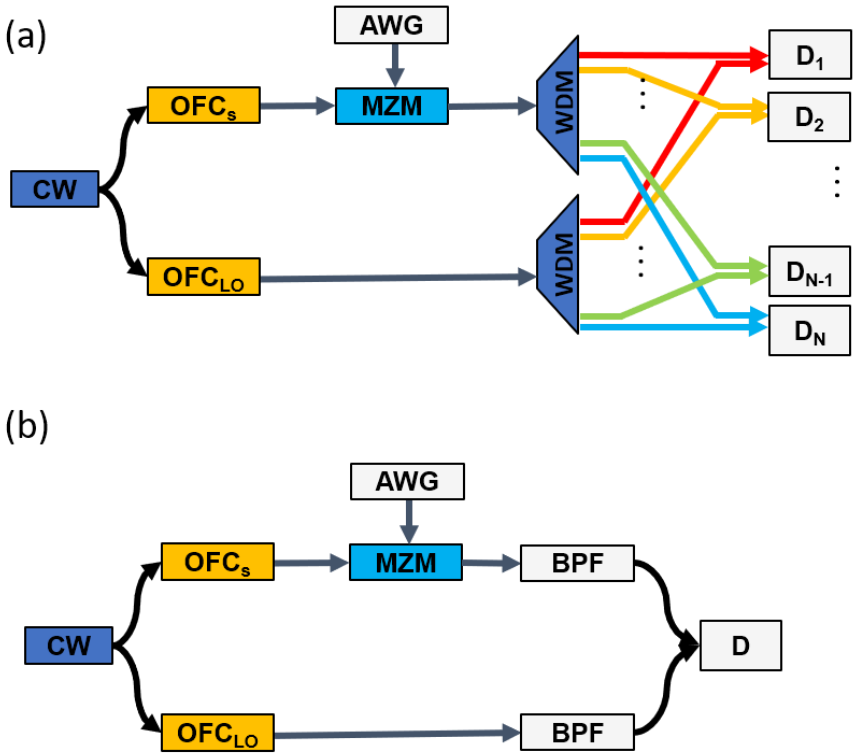

Figure. 3-1 Optical DFT scheme for (a) parallel processing and (b) equivalent experimental setup with bandpass filter (BPF) and a single coherent detector. OFC_s and OFC_{LO} represent signal and LO optical frequency combs. MZM: Mach-Zehnder modulator. CW: continuous-wave laser. WDM: wavelength demultiplexer. D: coherent detector. BPF: optical bandpass filter.

The optical DFT engine is illustrated in Figure. 3-1. Two phase-locked optical parametric combs possessed minimal OSNR in excess of 40 dB and 250 tones were generated from a single continuous wave (CW) seed laser possessing a linewidth of 5 kHz that was

centered at 1558.9 nm. Signal and LO comb pitch frequencies were 24.98 GHz and 25 GHz, respectively, providing for DFT resolution of 20 MHz. The first WDM is used to filter out the whole electrical signal spectrum modulated on an individual signal comb tone. The second WDM is used to filter out the corresponding LO tone for heterodyne detection. An array of coherent detectors D_1 to D_N, each consisting of a 90-degree hybrid, balanced detectors and an ADC, can be used to record the DFT coefficients simultaneously. This scheme is corresponding to a parallel demonstration, resulting in real-time DFT computation in parallel. To demonstrate the operational principle and measure DFT processor performance without fully populated backplane array, the WDM block was replaced by optical tunable bandpass filter and used to sweep the band and select corresponding signal-LO tone as shown in Figure. 3-1(b). By repeating the receiver stimulus, its operation was characterized using a single coherent detector rather than a coherent detector array.

3.1 Experimental impairments

To achieve superior performance using the hybrid DFT processor, practical experimental impairments must be taken into careful considerations. The most significant system impairments include but not limited to I-Q skew, DC offset, receiver imbalance, etc. and they can be compensated both in physical and digital domains in this experiment.

Timing mismatch between the in-phase and quadrature tributaries are also known as the IQ skew and it comes from different path length of optical and electrical links. IQ skew can significantly degrade the system performance if uncompensated in the coherent receiver[25]. Figure. 3-2 illustrates the constellation plot of coherent detection of binary-phase-shifted-key (BPSK) modulated signal. In the absence of IQ skew, the symbols are linearly aligned in the constellation plane. Here the sampling rate is higher than symbol rate so that the transients

between BPSK symbols are also captured. With IQ skew, the symbols are mismatched and detection penalty is imposed. The phase rotation of the symbols originates from time-varying polarization due to random birefringence. In coherent lightwave communication, several algorithms are proposed for IQ skew compensation in digital domain[26], [27]. In this experiment, IQ skew mainly comes from the physical pathlength mismatch from I and Q port of coherent receivers to ADCs (real-time oscilloscope) and the compensation can be performed in physical domain. By modulating a band-limited Gaussian noise signal $w(t)$ on optical carrier and use homodyne detection with the coherent receiver, signals captured from I and Q port can be represented as $I(t) = w(t)\cos(\phi) + n_1(t)$ and $Q(t) = w(t+\tau)\sin(\phi) + n_2(t)$ respectively. ϕ represents the phase rotation due to optical path length mismatch and τ is the time mismatch or skew delay. Cross-correlation between $I(t)$ and $Q(t)$ can be computed and the corresponding peak position indicates the I-Q skew. Usually the practical skew delay is less than a sampling period so that upsampling is required prior to cross-correlation. With the estimated I-Q skew, the delay of oscilloscope can be tuned to physically compensate the I-Q skew. Otherwise, digital I-Q skew compensation should be taken into consideration.

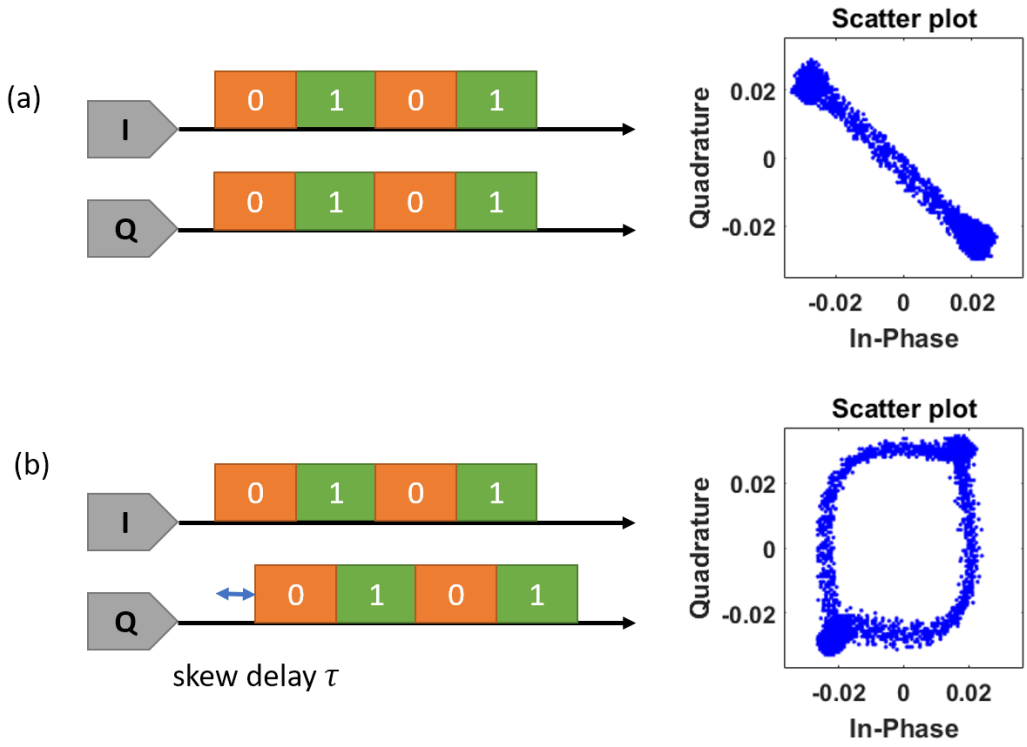

Figure. 3-2 Constellation of BPSK signal without/with I-Q skew.

DC-offset represents a direct-current offset term for both I and Q port in coherent receivers. In the hybrid DFT processor, that means a constant complex bias term added into the complex DFT coefficient and has to be subtracted. DC offset is common in direct conversion receivers due to mixer leakage, even-order nonlinearity, coupling issues, etc. DC-offset can be easily mitigated using pilot symbols. In order to have an accurate estimation of the DC-offset in complex plane, pilot symbols are preferred to have a uniform phase distribution over 0 to 2π, which is compatible with most current modulation formats such as quadrature amplitude modulation (QAM) and phase-shift-key (PSK) modulation. In this experiment, pilot symbols have sinusoid waveform and the average value of the digitized symbols can be estimated as DC-offset.

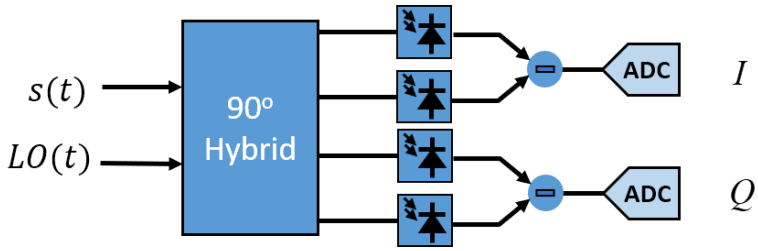

Figure. 3-3 Schematic of a coherent receiver.

As shown in Figure. 3-3 a 90-degree optical hybrid is a key component to provide phase diversity of optical coherent receiver. It mixes the incoming optical signal $s(t)$ with the local oscillator (LO) laser $LO(t)$ in such a way that different vectorial additions of LO and the incoming signal are obtained. In mathematics, the two pairs of outputs are $\frac{1}{\sqrt{2}}s(t)+\frac{1}{\sqrt{2}}LO(t)$ and $\frac{1}{\sqrt{2}}s(t)-\frac{1}{\sqrt{2}}LO(t)$, $\frac{1}{\sqrt{2}}s(t)+\frac{1}{\sqrt{2}}j\cdot\ LO(t)$, $\frac{1}{\sqrt{2}}s(t)-\frac{1}{\sqrt{2}}j\cdot LO(t)$. The outputs are sent into two balanced photodetectors such that the differential photocurrents are extracted and the corresponding electrical signals are $R\left(\left|\frac{1}{\sqrt{2}}s(t)+\frac{1}{\sqrt{2}}LO(t)\right|^2-\left|\frac{1}{\sqrt{2}}s(t)-\frac{1}{\sqrt{2}}LO(t)\right|^2\right)=2R\cdot real(s(t)\cdot LO^*(t))$ and $R\left(\left|\frac{1}{\sqrt{2}}s(t)+\frac{1}{\sqrt{2}}j\cdot LO(t)\right|^2-\left|\frac{1}{\sqrt{2}}s(t)-\frac{1}{\sqrt{2}}j\cdot LO(t)\right|^2\right)=2R\cdot imag(s(t)\cdot LO^*(t))$ respectively where R is the responsivity of the photodetectors. So that the real and imaginary part of $s(t)LO^*(t)$ are extracted and captured by two ADCs. The 90-degree phase shift is provided by the difference of accumulated optical phase in two paths of the LO signal. The optical hybrid is typically constructed using all-fiber or planar waveguide technology [28]. And free-space micro-optics-based 90-degree optical hybrid has been developed, which is passive and does not need any active control. However, the phase difference of two output signals may be deviated from 90-degree when the optical hybrid is imperfect. A phase offset from 90-degree is called a conjugate misalignment. Besides, the balanced detection uses two sets of balanced detectors and followed amplifiers, resulting in unidentical responsivity.

This phenomenon is called quadrature imbalance or simply receiver imbalance. Imbalance of coherent receivers causes amplitude and phase errors in captured I and Q data.

It is shown that the quadrature imbalance can be corrected with digital signal processing[29]. Assuming incoming signals with phase $\theta(t)$ and AC-coupled photodetectors, two received signals can be written as

$$I(t) = a \cdot \cos(\theta(t)),$$
$$Q(t) = b \cdot \sin(\theta(t) + \phi) \tag{3.1}$$

where ϕ is the conjugate misalignment which is an offset from 90 degrees and $I(t)$ and $Q(t)$ are the in-phase and quadrature signals respectively. Their relationship can be written as

$$\frac{I^2}{a^2} - \frac{2IQsin(\phi)}{ab} + \frac{Q^2}{b^2} - \cos^2(\phi) = 0 \tag{3.2}$$

In other words, the constellation diagram of the digitized received signals forms an ellipse in general and is circular without quadrature imbalance. The quadrature imbalance can be compensated with ellipse fitting method which finds the least square ellipse that best fitted to the constellation of the digitized received signal[30]. With pilot symbols, the ellipse parameters, which are major axis of $2a_0$, minor axis of $2b_0$ and the rotation angle of ρ respect to I axis described in equation (3.2), can be estimated. The corrected I and Q data can then be obtained by a simple transformation

$$I' = \frac{Icos(\rho) + Qsin(\rho)}{a_0}$$
$$Q' = \frac{-Isin(\rho) + Qcos(\rho)}{b_0} \tag{3.3}$$

In this experiment, a sinusoidal signal generated from signal generator is used as pilots and the corresponding compensation is shown in Figure. 3-4.

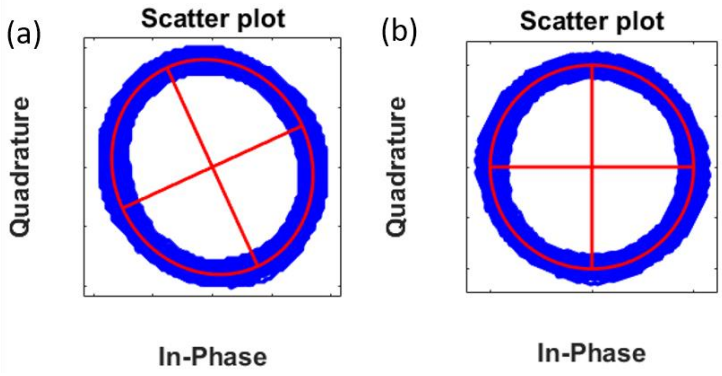

Figure. 3-4 Constellation of a sinusoidal signal before and after imbalance compensation.

The optical and electrical link nonlinearity is significant and will be discussed along with the experimental results in chapter 3.2. Other practical experimental impairments are also critical in many scenarios such as chromatic dispersion, and frequency and phase response optical and electrical components but have less impact in this experiment and not discussed in detail here.

3.2 DFT of sinc-shaped signal

In the first demonstration DFT coefficients of signals with waveform of time-limited sinc function were generated. An electrical sinc-shape signal with 50ns duration and 200MHz bandwidth centered at 1GHz was generated from an arbitrary waveform generator (AWG) and amplified by an electrical amplifier. The amplified electrical signal was modulated onto signal comb through a Mach-Zehnder modulator biased at null-point for subsequent DFT computation.

Significant degradation due to two kinds of link nonlinearity was observed in this experiment. The first nonlinearity originates from the nonlinear response of the electrical amplifier. An amplifier is an analog system that takes a small amplitude signal as an input and produces a large amplitude signal as output. When signals have large amplitude and are modulated on optical carriers, the optical signal has higher optical power and higher optical

signal to noise ratio, improving the signal to noise ratio (SNR) after photodetection. However, the amplification is generally nonlinear, especially for large input signals, causing distortion and sidebands. The second nonlinearity originates from the nonlinear transfer function of MZM modulators. MZM is generally built with $LiNbO_3$ waveguides with a push-pull configuration. When applying voltage $V(t)$ on an MZM, the output field is expressed as

$$E(t) = E_0 \sin\left(\kappa V(t) + \phi_b\right) \tag{3.4}$$

where E_0 is the field of input light source, ϕ_b is the bias and κ is related to modulation efficiency. When biased at null point, ϕ_b is approximately 0 such that the transfer function is sinusoidal as shown in Figure. 3-5. This transfer function is nonlinear and only approximately linear in a limited input voltage range where V is small. However, when the input voltage is small, the output optical power is weak, resulting in limited signal power and signal to noise ratio and hindering the photodetection performance.

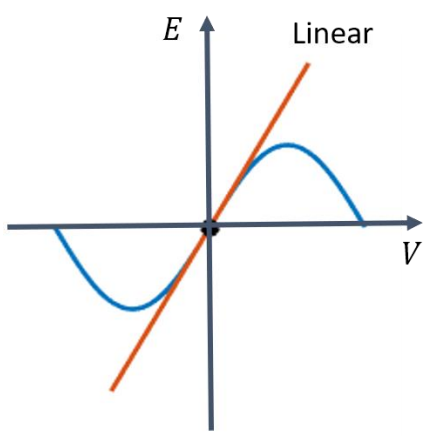

Figure. 3-5 Transfer function of an MZM modulator biased at null point. Red line is the desired linear transfer function.

The tradeoff between optical signal power and nonlinearity can be circumvented by predistortion of the input signal. In this experiment digital predistortion was used to mitigate nonlinear system transfer functions including but not limited to amplifier nonlinearity and

modulator nonlinearity. The objective is to generate a predistorted waveform $s_p(t)$ from AWG such that the coherent detected signal is desired $s(t)$ after going through a nonlinear system $F(\cdot)$, i.e. $s(t) \approx F(s_p(t))$. The coherent detection scheme is shown in Figure. 3-6. With an initial input $s(t)$ the output of coherent detection is $F(s(t))$. By normalization and synchronization, the result $y(t)$ was compared to $s(t)$ and the difference $y(t) - s(t)$ was feedback to AWG to generate a predistorted version of $s(t)$, which was $s_p^{(1)}(t)$, such that the mean square error between corresponding output $y^{(1)}(t)$ and $s(t)$ is reduced. The superscript indicates number of iterations. Many off-the-shelf algorithms are available and can be applied for high performance nonlinearity mitigation[31]. If the difference $y^{(1)}(t) - s(t)$ is above threshold then it was fed back for better predistortion performance. This process was iterated multiple times until the output is sufficiently close to the desired signal $s(t)$.

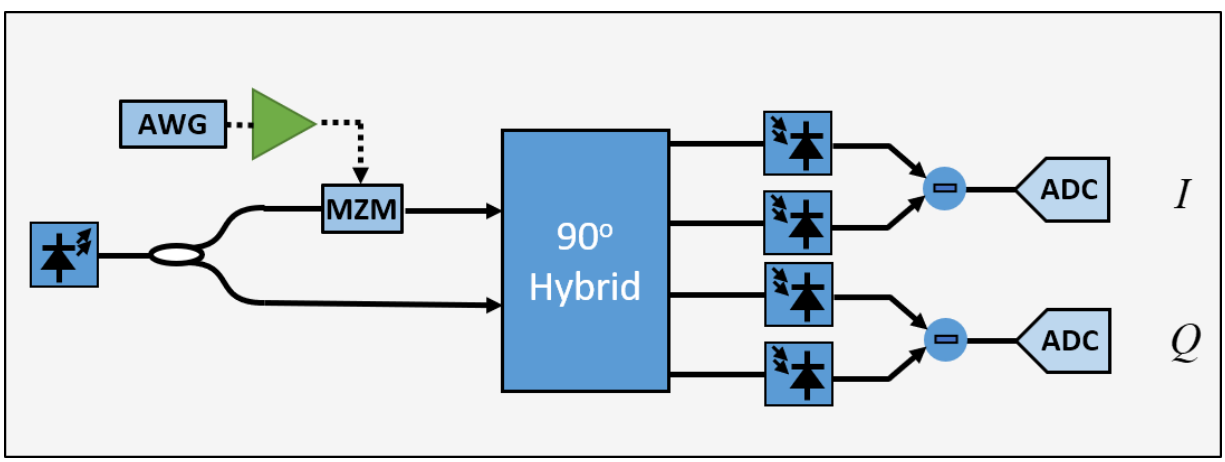

Figure. 3-6 Scheme of digital predistortion. The green triangle is an electrical amplifier.

In this experiment, the time-limited sinc-shape waveform was predistorted such that after coherent detection, a sinc-shape waveform is guaranteed. Figure. 3-7 illustrates the signal waveform and spectrum with and without predistortion and the system output of the predistorted signal matches the ideal signal well. The sidelobes due to distortions are significantly reduced

by more than 20dB. Other than digital predistortion, analog predistortion techniques are applicable for compensating nonlinearity from amplifiers and modulators [32], [33] but not adopted here due to hardware complexity.

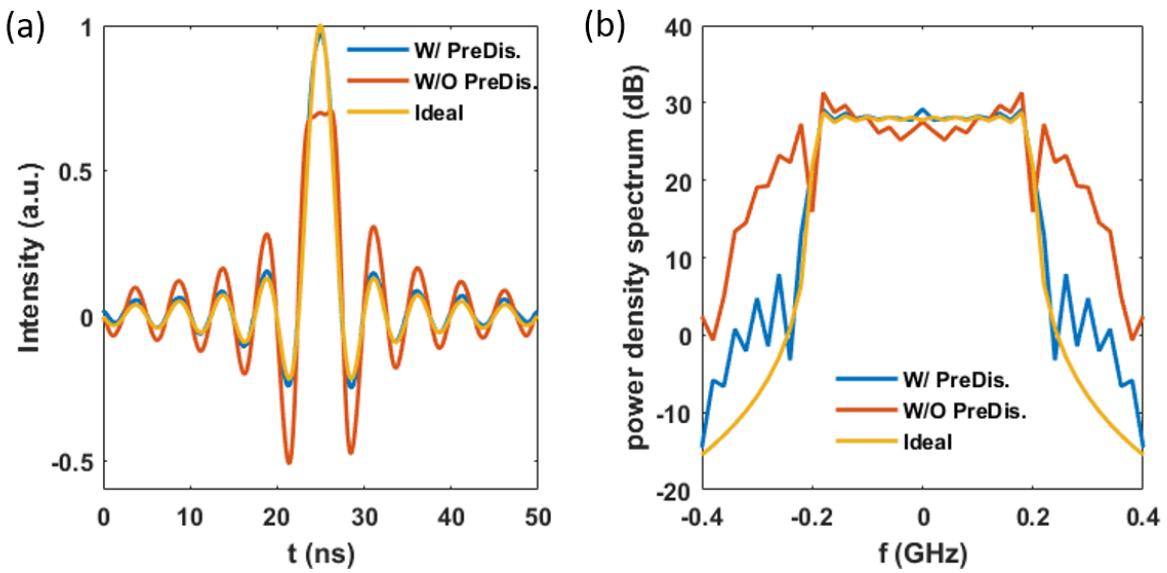

Figure. 3-7 Waveform and spectrum of a time-limited sinc-shaped signal with and without predistortion.

With digital predistortion, the predistorted time-limited sinc-shaped signal was generated by a 10 GS/s AWG as an electrical input signal for DFT computation. At the receiver, a 50 GS/s ADC was digitally filtered down to 20 MHz to get the DC term of the detected signal. However, it has to be emphasized that a minimum of 20 MS/s ADC is sufficient to capture output data, which is far below full utilization of current ADC. The spectrum recovered with the hybrid DFT processor is shown in Figure. 3-8 and the experimental results match the ideal spectrum well, validating the DFT operation of the proposed hybrid DFT processor.

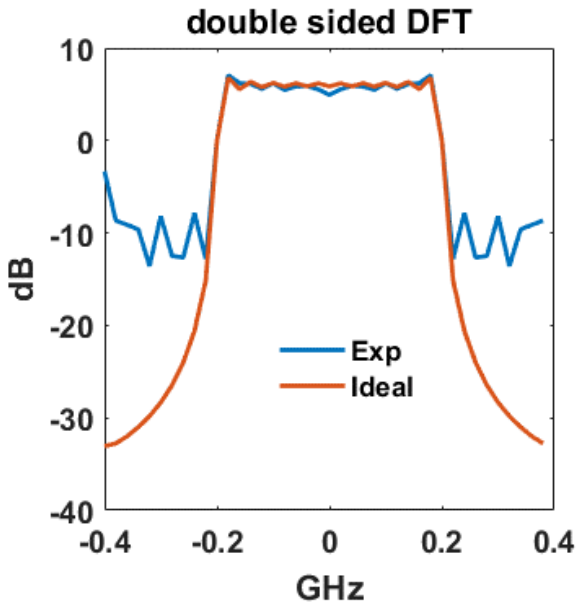

Figure. 3-8 Spectrum recovery of the hybrid DFT processor for time-limited sinc-shape waveform.

3.3 DFT of BPSK signals

The performance characterization of the hybrid DFT processor can be extended to BPSK signals. A 25-bit-long raised cosine filtered binary sequence at 0.5 Gbps with 200MHz bandwidth, was generated by a 10 GS/s arbitrary waveform generator (AWG) as an electrical input signal for DFT computation. The 25-point recovered DFT spectrum is shown in Figure. 3-9(b). The DFT engine output was actually a set of complex DFT coefficients (Figure. 3-9(c)), which is useful for advanced signal processing like convolution and filtering. In summary, the experimental data matched the ideal DFT results and a 25-point DFT at 500 Million-DFT-point per second throughput is achieved requiring slow, 20 MS/s ADCs. The mismatch at isolated points was attributed to non-ideal phase recovery and residual nonlinear effects.

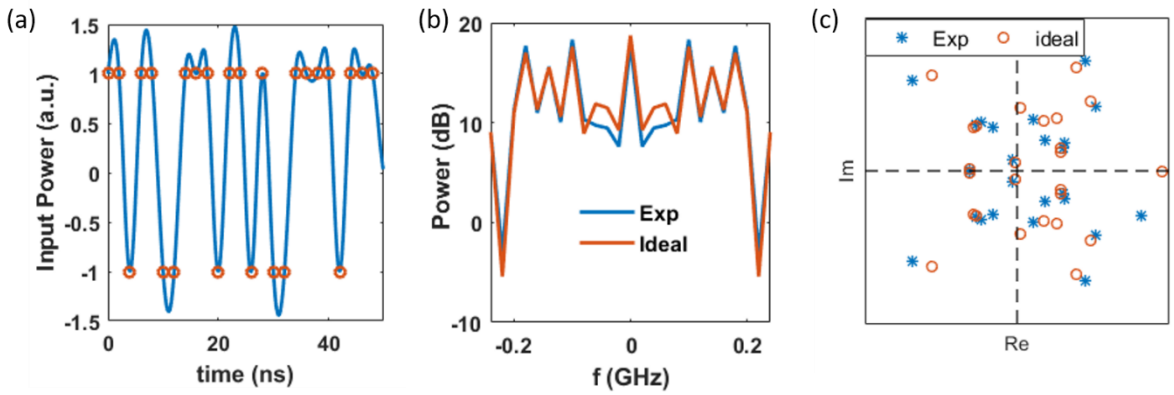

Figure. 3-9 DFT computation of BPSK signal. (a) Input binary sequence of raised cosine shape. Red circle denotes the 25 points for DFT calculation. (b) Recovered 25-point DFT spectrum and (c) complex DFT coefficients.

3.4 Summary

A comb-assisted discrete Fourier transform processor is demonstrated for time-limited sinc-shaped signals and BPSK signals and their performance are characterized. The experimental implementation and practical experimental impairments have been discussed thoroughly. In principle, the new DFT processor poses significant advantages over the existing photonic-assisted Fourier transform scheme in terms of flexibility and precision. Moreover, this processor has the potential to circumvent the performance-dissipation limit of current all-electronic DFT processors and operate with combined high throughput, higher precision and lower power consumption.

Chapter 3, in part, is a reprint of the materials as it appears in *Optical Fiber Communication Conference (2017)* titled "Comb-assisted real-time Discrete Fourier Transform processor" authored by Huan Hu, Daniel Esman, Vahid Ataie, Eduardo Temprana, Bill Kuo, Nikola Alic and Stojan Radic. The dissertation author was the primary investigator and the primary author of this article.

Chapter 4 Hybrid Broadband OFDM receiver

Orthogonal frequency division multiplexing (OFDM) is a widely used signaling format in wireless communication and ultra-wideband radio-frequency applications. An OFDM transceiver relies on DFT processor that matches both the resolution and the bandwidth of the wireless link. A conventional wide-band OFDM receiver necessarily relies on high-speed analog to digital converters (ADC) followed by a Fourier processing core. Both fundamental and practical ADC considerations that include bandwidth-resolution tradeoff, impose strict limits on high precision digitization of the wideband OFDM signal. In addition to the quantization barrier, computational complexity of high-speed DFT processor leads to high dissipation levels in conventional receivers. This chapter demonstrates an alternative OFDM receiver architecture that eliminates the need for high-speed ADC and digital DFT processor. The new design is based on hybrid, opto-electronic DFT processor, capable of generating DFT coefficients of wideband radio-frequency (RF) signal in real-time.

The basic concept of OFDM is introduced first in this chapter. Then a novel OFDM receiver architecture relying on dual-comb assisted DFT processor is discussed in 4.2. To characterize the performance of the proposed DFT processor, reconstruction and demodulation of signals with pulse-position-modulation (PPM) are discussed in chapter 4.3. In chapter 4.4 the OFDM receiver is demonstrated by demodulation of a 4-QAM OFDM signal with 60 subcarriers positioned within 4 GHz - 15.8 GHz band and separated by 200MHz. When used as OFDM receiver, the novel receiver suffered from phase noise due to residual phase noise of mutually coherent combs. In chapter 4.5, three methods are proposed for phase noise compensation and the corresponding receiver performance are discussed.

4.1 Principles of OFDM

Orthogonal Frequency Division Multiplexing (OFDM) is a multicarrier transmission technology for high data rate communication system. The OFDM concept is based on spreading high-speed data to be transmitted over several low rate carriers. The carriers are orthogonal to each other and frequency spacing between them are created by using the Fast Fourier transform (FFT).

OFDM originates from Frequency Division Multiplexing (FDM), in which the total bandwidth available in a communication medium is divided into a series of non-overlapping frequency bands, each of which is used to carry a separate signal. In FDM, the channels are placed sufficiently far apart so that the signal spectra do not overlap, and the resulting spectral efficiency is very low as compared with OFDM. FDM is first utilized to carry high-rate signals by converting the serial high-rate signal into parallel low bit streams. Such a parallel transmission scheme is costly to build when compared with high-rate single carrier scheme. On the other hand, high-rate single carrier scheme is more susceptible to inter-symbol interference (ISI). This is due to the short duration of the signal and higher distortion by its wider frequency band as compared with the long duration signal and narrow bandwidth subchannels in the parallel system.

OFDM is a multi-carrier modulation technique where data symbols are transmitted over a parallel collection of regularly spaced subcarriers, similar to FDM. However, the subcarriers have the minimum frequency separation required to maintain orthogonality of their corresponding time domain waveforms, yet the signal spectra corresponding to the different subcarrier overlap in frequency. The overlap of frequency results in efficient use of the available

bandwidth with much higher bandwidth efficiency than FDM, where a comparison is depicted in Figure. 4-1.

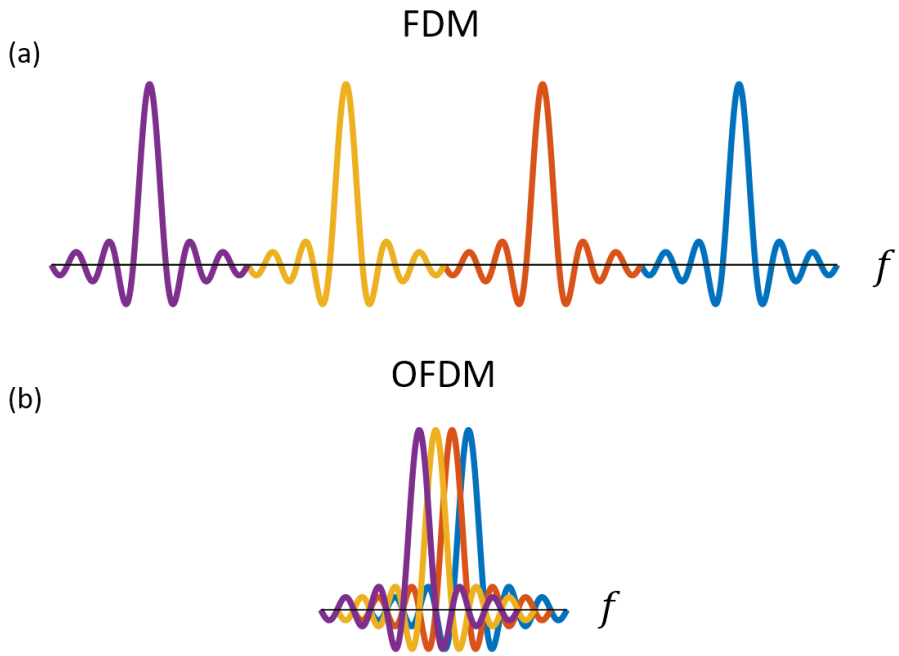

Figure. 4-1 A comparison between FDM and OFDM.

OFDM is simple to use on channels that exhibit time delay spread or, equivalently, frequency selectivity and has developed into a popular scheme for wideband digital communication, used in applications such as digital television and audio broadcasting, wireless networks and 4G/5G mobile communications.

The basic block diagram of OFDM transmission system is shown in Figure. 4-2 [34]. A block of binary bit streams is mapped to N data symbols $\{s_k, k = 0, 1, \dots, N-1\}$ from an appropriate signal constellation such as quadrature amplitude modulation (QAM) in parallel. The OFDM modulation is implemented as an N-point inverse discrete Fourier transfer (IDFT) on the block of N data symbols followed by a DAC. In practice, the IDFT can be implemented with the computationally efficient inverse fast Fourier transform (IFFT). The IDFT of the data block is

$$S_n = \sum_{k=0}^{N-1} s_k \exp\left(\frac{j2\pi nk}{N}\right), n = 0, 1, \dots, N-1 \tag{4.1}$$

yielding the time-domain sequence $\{S_n, n = 0, 1, \dots, N-1\}$. To mitigate the effect of ISI caused by channel delay spread, each block of N IFFT coefficients is typically preceded by a cyclic prefix, which is a replicate of the last several IFFT coefficients, or a guard interval such that the total duration of each OFDM symbol is greater than the channel length. The cyclic prefix or guard interval is useful for implementing time and frequency synchronization functions in the receiver, however, it results in a power and bandwidth penalty and can be eliminated in some specially designed OFDM implementations[35]. The resulting OFDM symbols are input to a digital-to-analog converter (DAC) to generate OFDM waveform. In many applications, such as wireless communication, the generated waveform is mixed with a carrier signal and upconverted to the desired transmission frequency band.

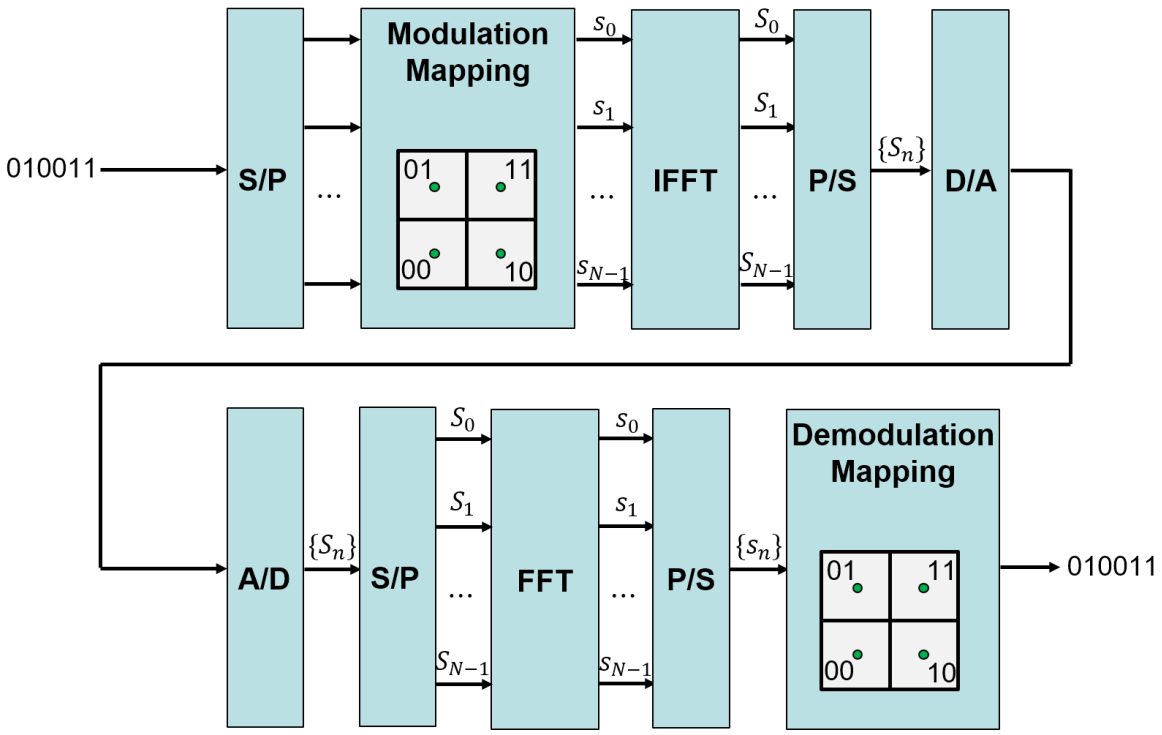

Figure. 4-2 Block diagram of OFDM transmission system. S/P: serial to parallel conversion. P/S: parallel to serial conversion. D/A: digital to analog conversion. A/D: analog to digital conversion.

At the receiver, the received signal is down-converted to baseband and sampled by an analog-to-digital converter (ADC). If guard interval is used, samples received during guard interval are discarded. Then the demodulation process is performed by converting each block of N received samples to the frequency domain using DFT and mostly implemented as FFT. When duration of each OFDM symbol is greater than the channel length, the received sequence is the linear convolution of the transmitted sequence of IFFT coefficients with the discrete-time channel. As a result, the effects of the ISI are completely and easily removed in frequency domain. Each of the N frequency domain samples is processed with a simple one-tap Frequency Domain Equalizer (FDE), which simply multiplies each FFT coefficient by a complex scalar, to recover the data symbols. The transmitted bit streams are then recovered using the same mapping.

4.2 OFDM receiver architecture

The key technology for current and future OFDM communication systems and UWB RF applications is the high-rate, high-precision DFT processor capable of mapping digitized waveform to Fourier domain in real-time. Currently, DFT is implemented in the form of FPGAs and ASICs platforms. However, the conventional, all-electronic OFDM receivers face both fundamental and practical challenges as discussed in chapter 1.1. Firstly, silicon DFT processor faces computation limit inherent with maximal transistor density, imposed by quantum and thermal effects [2]. Secondly, in addition to a need for fast DFT processors, wideband OFDM receiver requires a high-rate ADC, which imposes basic dissipation limitations and requires a tradeoff between speed and quantization precision[3]. To circumvent these two challenges the hybrid DFT processor with dual combs that have been discussed and demonstrated in Chapter 3. However, due to resources limitation, a single coherent receiver and optical tunable filters were used such that the parallel operation has not been truly demonstrated. This section describes a new hybrid DFT processor of sample-and-hold topology, operating in parallel and serving as the core of the proposed new OFDM receiver.

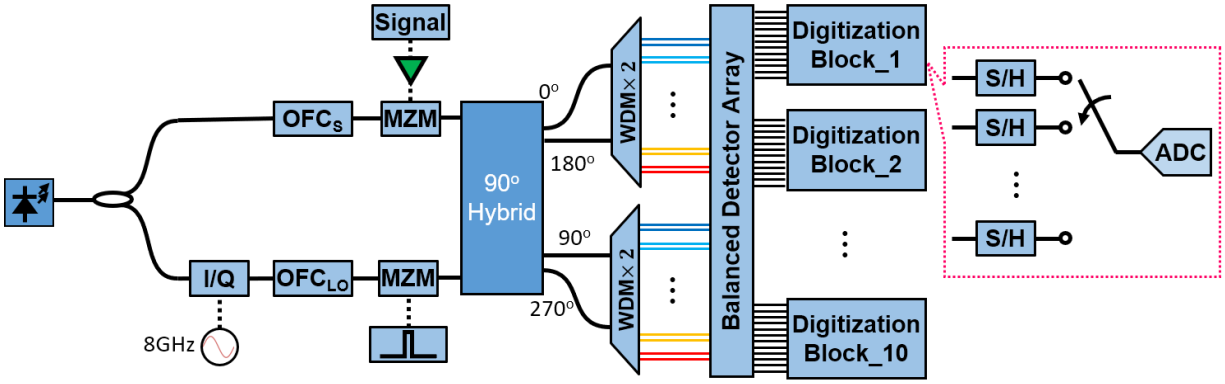

Figure. 4-3 Scheme of the hybrid DFT Processor. OFCs and OFC_{LO} are signal and LO optical frequency combs, respectively. I/Q: IQ optical modulator. MZM: Mach-Zehnder Modulator. WDM: Wavelength division multiplexer. S/H: Sample-and-hold circuit. ADC: Analog to digital converter. Each digitization block consists of 12 sample-and-hold units and a single ADC.

The topology of a hybrid DFT processor is illustrated in Figure. 4-3. The performance of DFT processor relies on generating mutually coherent combs with sufficiently high power, high OSNR, frequency stability, and tone pitch tunability. Two coherently coupled optical frequency combs (OFC_S and OFC_{LO}) with OSNR of 50 dB were generated from single continuous wave (CW) seed laser centered at 1549.3nm with shock wave engineering, which has been introduced in chapter 2.3. The signal and LO pitch were chosen to be 49.8 GHz and 50 GHz respectively, corresponding to DFT resolution of 200 MHz. The frequency tones of optimal performance fall into the spectral range spanning the seeding tone and the optical comb spectrum is shown in Figure. 4-4. The spectral ripple within the range is less than 1dB. In order to have highly coherent, flat and stable tones in the desired frequency range of DFT operation, The LO comb is up-converted by 8 GHz with an In-Phase Quadrature-Phase (IQ) optical modulator to accommodate with desired 4 GHz to 15.8 GHz frequency range of DFT operation, corresponding to 60 tones spanning from 1541.3 nm to 1565.3 nm.

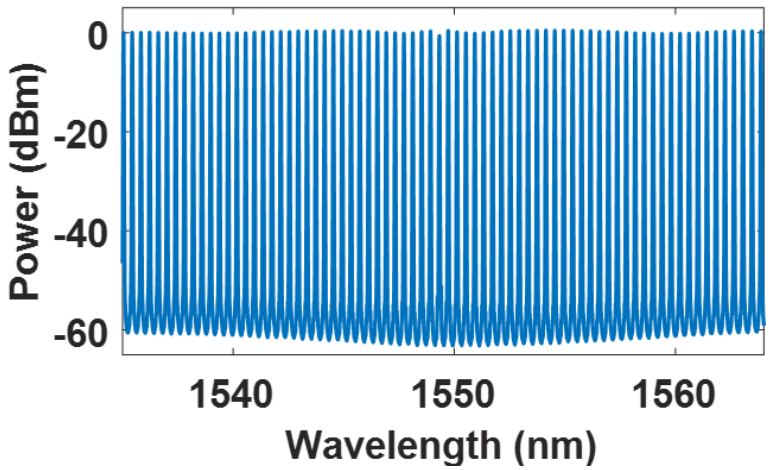

Figure. 4-4 Spectrum of signal OFC. The spectral resolution is 0.02 nm.

Signal copies were generated by modulating all comb tones by a Mach-Zehnder modulator (MZM), biased at null point. A single 90° hybrid was used to combine all signal

copies and LO carriers onto sub-rate coherent detection plane. 50 GHz pitched WDM was used to route signal-LO pairs corresponding to each DFT bin onto corresponding detection element. A balanced detector array (120 balanced detectors) converts each signal-LO optical tributary to real and imaginary terms of complex DFT coefficients.

Instead of using a fully populated backplane (120 ADCs), ten outputs of 12-block coherent detectors were multiplexed into a single ADC operating at 500 MS/s via sample-and-hold stage, followed by 12:1 multiplexer. As a consequence, simultaneously generated DFT coefficients are simultaneously digitized and buffered within the hold stage until sampled by the output ADC. This is fundamentally different than the architecture used in Chapter 3. The sampling process can be viewed in terms of sequential switching of a single ADC to 12 hold circuits in order to acquire 6 complex DFT coefficients. Ten ADCs were parallelized to capture full complement of 60 coefficients within 5 ns long reception window. The receiver window was opened periodically, defined by the hold time (500ns). Consequently, a 5ns long optical gate was used to modulate LO comb, allowing for effective heterodyne detection within the reception window. During each 5ns reception window, buffered analog signal from each block of 12 balanced detectors was quantized by ADC and DFT coefficients are streamed to the offline DSP. A potential concern with described setup is that the modulator bias point is sensitive to carrier wavelength excursion which, when coupled with constant bias configuration would impose receiver penalty. However, the architecture shown here is specifically designed to minimize this effect, and no measurable impairment was observed [36]. First, the shifted null-point bias voltage of a signal tone yields a constant electric field term on the modulated signal, allowing for simple backplane compensation. Second, when the shifted bias voltage exceeds the linear modulation region, the signal should be attenuated to avoid distortion, requiring higher

OSNR[37], [38] and higher power per carrier. Recognizing these requirements, both combs generated through shockwave mixing were engineered with high OSNR (50 dB) and power per tone (0 dBm) well above receiver sensitivity, allowing for a simple signal equalization.

4.3 PPM signal demodulation

In the first demonstration of the receiver operation, 8-PPM signal was generated from a pattern generator at 600 Mbps and decoded by the hybrid architecture described above. The bit sequence was synchronized with the 5ns optical gate and then up-converted to 8 GHz, amplified and modulated onto the signal comb. The first 16 symbols were used for calibration, with power and phase equalization applied [29]. When time-domain signal is real-valued, its Fourier transform is conjugate-symmetric in spectral domain. Consequently, for each received symbol, assuming that the signal spectral power density below 4 GHz is negligible, 60 retrieved DFT coefficients are sufficient to recover the time-domain signal with an equivalent sampling rate of 32 GS/s.

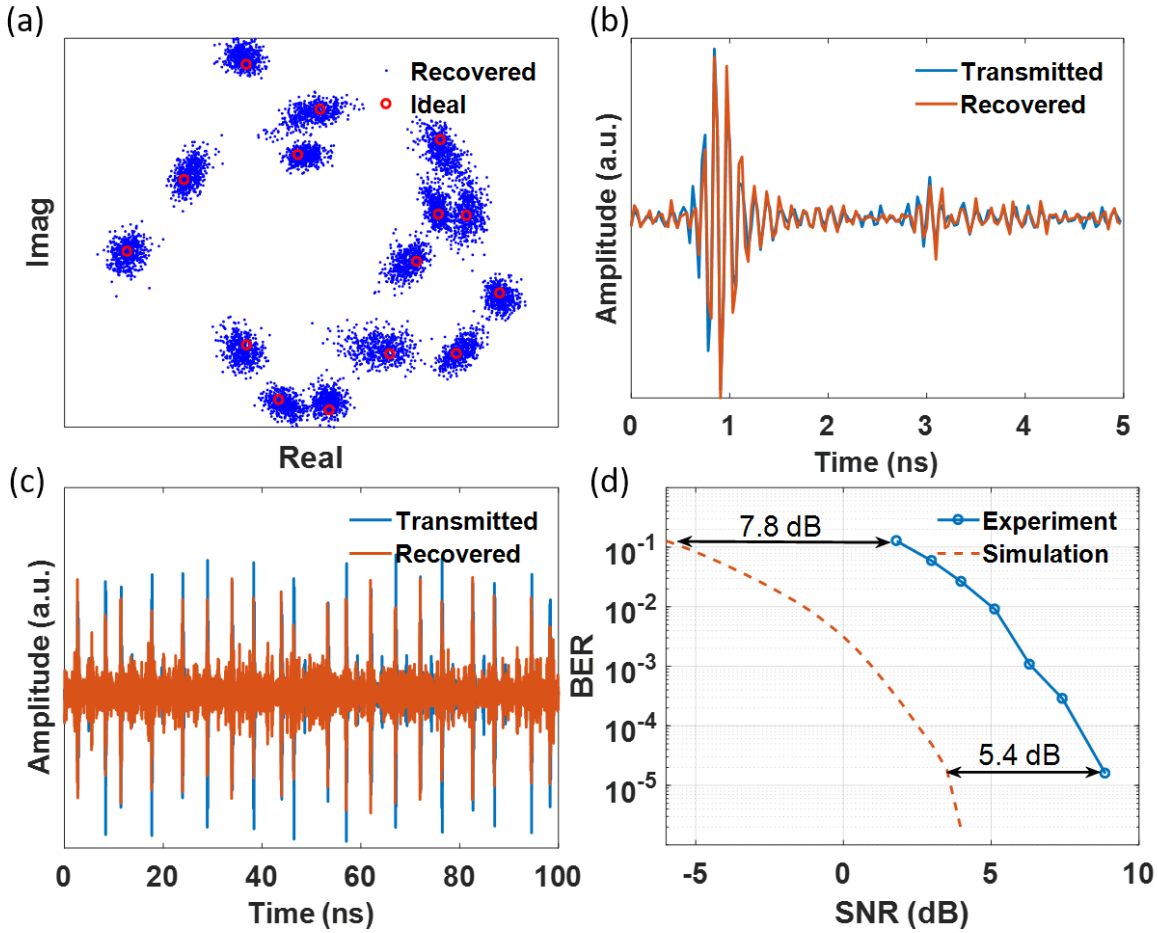

Figure. 4-5 (a) Recovered complex DFT coefficients from 6.8 GHz to 9.6 GHz of 503 identical symbols (blue dots). Red circle shows the DFT coefficients of the transmitted symbol. (b) Comparison of transmitted and DFT recovered waveform of a single symbol and (c) 20 symbols which has random pulse positions. (d) BER performance from experiments and simulation.

In the first set of experiments, each symbol had an identical pulse position and was expected to have DFT coefficients that do not vary during the reception. The performance of the hybrid DFT processor was then characterized by comparing DFT coefficients of the PPM channel recovered by the DFT processor to the calculated (ideal) DFT coefficients of the transmitted signal. For each of the received 503 symbols, 15 out of 60 DFT coefficients with the largest magnitude, located within 6.8 GHz - 9.6 GHz band, are plotted in Figure. 4-5 (a) (blue dots); distinct clusters indicate DFT coefficients at separate frequencies. Each cluster is close to the ideal DFT coefficients, indicating accurate DFT coefficient capture by the hybrid DFT

processor. As an example, a randomly selected symbol recovered from the captured DFT coefficients, closely matches the transmitted signal directly digitized by a real-time oscilloscope with 20 GHz bandwidth (Figure. 4-5 (b)), demonstrating the ability for high speed, high precision sampling using only sub-rate ADC and sub-optimal sample-and-hold backplane.

In the second experiment, 8-PPM symbols, with has a random pulse position, were transmitted at different noise levels and recovered from captured DFT coefficients using the hybrid processor. Figure. 4-5 (c) shows a comparison between transmitted and recovered waveform of the first 20 symbols at the SNR of 8.9 dB. The performance was further characterized by demodulating the PPM signal and measuring bit error rate (BER), as shown in Figure. 4-5 (d). The recovered waveforms are down converted to the baseband and low-pass filtered, with each bit demodulated by searching the peak position of the recovered pulse. The BER performance was evaluated by demodulating 42240 symbols at varied SNR levels (Figure. 4-5 (d)). As a comparison, idealized simulations (distortion-free modulator, receiver and ideal optical carrier) were carried out by adding band-limited Gaussian noise (3.9 GHz to 15.9 GHz) to the measured transmitted signal and repeated the same demodulation process to make the simulation as close to experiments. When compared to the simulated BER, the experiment showed a 5.4 dB penalty to maintain the same BER level in the high SNR region and a higher degradation in the low SNR region. Performance degradation with respect to idealized transceiver is easily accounted by recognizing the specifics of the experimental implementation. Firstly, the electronics backplane including transimpedance amplifiers (TIAs) and sample-and-hold circuits added additional noise in the DFT coefficients acquisition. Secondly, the phase noise that accompanied signal-LO tone pairs distorted the signal phase recovery. While, in principle, the spectral linewidth should be conserved for each tone [39] during the parametric

comb generation, the residual phase noise scales with tone orders in four-wave mixing process, when implementation does not incorporate noise-inhibition techniques. As a result, high order tones will be more noisy than the central ones, leading to higher inaccuracy of the captured DFT coefficients. It must be emphasized that this inaccuracy originated from the fluctuation of phase difference between a signal-LO tone pair rather than individual phase information of a single tone. Consequently, the phase difference was directly measured by directly beating signal comb and LO comb. The quadratic scaling of phase noise variance indicated linear scaling of the phase noise[40], [41]. Consequently, the phase noise cannot be neglected in OFDM receiver that makes full use of all available subcarriers and the phase noise compensation methods, either in physical or DSP domain must be considered. The latter type of compensation is discussed in chapter 4.5.

4.4 OFDM signal demodulation

Motivated by the fact that the new hybrid DFT processor directly generates the Fourier coefficients in a parallel manner, during the second demonstration OFDM-encoded signal reception was considered. Specifically, it was demonstrated by demodulation of 4-QAM OFDM signal with 60 subcarriers spaced at 200 MHz (from 4 GHz to 15.8 GHz). OFDM signal was generated using by 64 GS/s Digital-to-Analog converter (DAC) with 8-bit resolution and digital pre-compensation was applied to equalize RF power across all subcarriers. Additionally, white Gaussian noise was physically injected to the OFDM signal before detection to emulate target SNR at the receiver. A variable electrical attenuator was used to attenuate the noise power so that the SNR condition can be changed accordingly. The signal was captured during 5ns-long window every 500 ns and gated with the pulse that combined LO comb and signal paths. While no cyclic prefix is added to the OFDM signal, the receiver remained compatible with

conventional OFDM signals with cyclic prefix: it is merely sufficient to filter the prefix in time domain before performing physically assisted DFT decomposition. For each channel, 8000 symbols were captured and post-processed. After power and phase equalization [29], the outputs of DFT processor were used to reconstruct the transmitted symbols of a 4-QAM signal.

Phase noise causes significant performance degradation in OFDM systems by inducing common phase error (CPE) and intercarrier interference (ICI). The CPE term represents the common rotation of the whole constellation in the complex plane, while the ICI term is usually modeled as Wiener or Gaussian process, either by free-running local oscillators or phase-lock-loops. Multiple methods have been proposed to compensate the phase noise in either wireless [42]–[44] or optical communications [45]–[47]. However, the phase noise in hybrid OFDM receiver differs from the conventional OFDM receiver due to the specific physical process behind the noise generation in a parametric comb. Consequently to simplify performance analysis of the comb-assisted OFDM receiver, time and frequency synchronization are achieved in advance and minimal channel fading was held during all measurements. In the hybrid DFT processor, the phase decorrelation between selected pair of tones will add excess phase noise to the detected OFDM symbol and will necessarily degrade the overall channel performance such that phase noise compensation is required.

4.5 Phase noise characteristics

Apart from the proposed OFDM receiver, phase noise of the individual tone of an OFC is a critical concern since it is detrimental to system coherence for applications based on dual coherent OFCs architecture such as precise ranging[48], spectroscopy[49] and signal processing[50]. The frequency of the n-th order tone from the comb can be represented as $f_n = f_0 + n \cdot \Delta f$ where Δf is the frequency pitch and f_0 is the frequency of the seeding (master) laser

oscillator. The phase noise in dual OFCs originates from laser source and radio-frequency (RF) drivers[51], replicated to the new carriers defined by the seed f_0 and pitch frequency Δf respectively. To minimize phase noise transferred from the seed laser, OFC construction relies on low linewidth emitters. In dual comb applications, these requirements can be relaxed by generating Verniered combs mastered by a single laser source[24]. Similarly, to suppress carrier replication of phase noise from RF oscillators, it is necessary to rely on low phase noise RF components. However, any physically realizable RF component generates noise level that can be detrimental[52], since phase noise scales with increasing mode number[53], ultimately limiting practical use of OFC with high tone count.

In principle, the linewidth of a single parametric comb generated through shockwave engineering is preserved across all tones when high phase correlation between the beating tones is maintained [39]. However, residual phase decorrelation occurs in a dual-comb scheme because of multiple mechanisms that include, but are not limited to phase noise from the RF source used to generate the 50 GHz and 49.8 GHz carrier and 8 GHz up-conversion frequency, the path length mismatch between two comb paths and electronics backplane distortions originating from TIAs and sample-and-hold circuits. Unless the coherency across both combs is strictly controlled, the first term can become significant because the cascaded FWM process may lead to scaling of phase noise in the higher-order tone generation. The second term leads to the slow path-length variations in the fiber waveguide but can be easily eliminated. The third mechanism can lead to phase decorrelation and could be minimized by matching ADC and TIA performance with the photonic end of the processor.

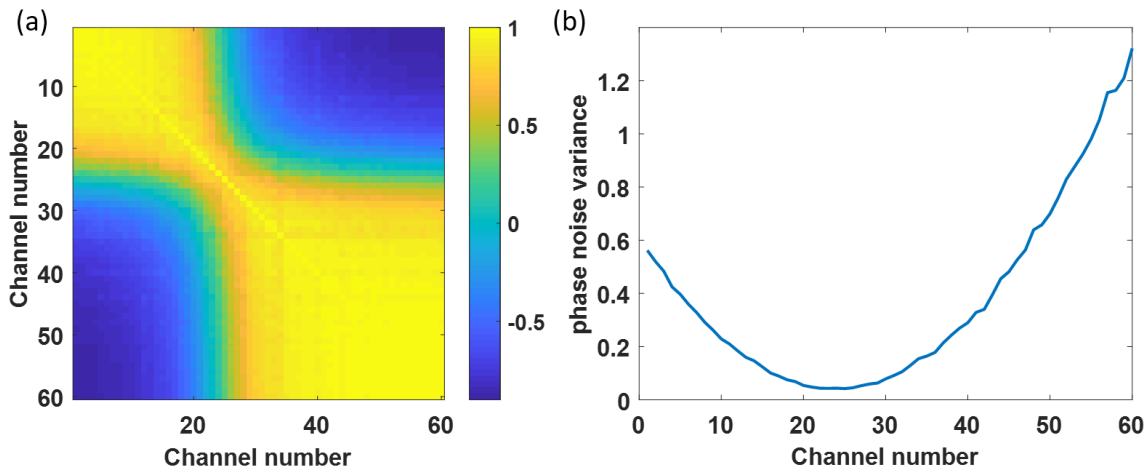

Figure. 4-6 (a) Correlation matrix of phase noise over all 60 channels. (b) Variance of phase noise of each channel indicates a quadratic scaling over comb mode order. Channel 21 corresponds to the zero-order comb mode. Phase noise was measured at 19.8 dB SNR condition.

The phase coherence of dual-comb has been studied before and matches the theoretical predictions[54]. The analysis of dual-comb topology that relies on shockwave engineering and subsequent tonal correlation is extended here. The phase of the n-th tone of two combs can be represented as $\theta_n^{(i)} = \psi_0^{(i)} + n \cdot \phi^{(i)}, i = 1$ or 2 [53] where ψ is the phase term originates from the seed laser and ϕ originates from RF components. When two combs are generated using a single seed laser, $\psi_0^{(1)} \approx \psi_0^{(2)}$. However due to aforementioned residual phase noise terms, the phase of the beating term of these two comb line is $(\psi_0^{(1)} - \psi_0^{(2)}) + n \cdot (\phi^{(1)} - \phi^{(2)})$, which is linear over comb mode order with an additive noise term. The calculated correlation matrix of the phase term is shown in Figure. 4-6(a) and the phase variance is shown in Figure. 4-6(b). In this experiment, the 21st channel corresponds to the zero-order comb mode. The correlation matrix pattern and the quasi-quadratic scaling of phase variance match well with previous reports on optical combs generated from cascaded modulators[54], validating the linear relation between phase noise and comb mode order with parametric combs generated through

shockwave engineering. To the best of the author's knowledge, it represents the first such study of noise inhibition in parametric combs generated by shockwave engineering.

4.6 Phase noise compensation

Phase noise suppression is essential for radio-frequency (RF) photonics utilizing high fidelity combs[50], [55]. While a variety of phase noise compensation approaches have been proposed in physical domain such as feedforward[56] and feedback[57] architectures, the complexity and computational cost of these implementations proved challenging in practical applications. Alternatively, phase estimation in digital domain was explored since it relaxed the requirement of tight phase-locking. The latter is one of the primary reasons for its widespread use in carrier phase estimation in lightwave communication systems [58], [59].

Conventional phase estimation is performed in a channel-by-channel manner. A single-channel phase estimation typically applies a time-averaging filter on the estimated phase to remove the effects of additive noise. One of the most common and simplest phase estimation algorithms is Viterbi-Viterbi (V-V) algorithm, suitable for M-ary phase shift keying (M-PSK) modulation and recently with M-ary quadrature amplitude modulation (M-QAM) when combined with PSK-partitioning techniques[60].

The phase noise is usually modeled as Wiener process. For 4-QAM modulated signals, V-V algorithm raises the received symbol to fourth power, estimates the common phase offset by taking average over a block of symbols, and unwrap the phase. The resulting phase ϕ is then divided by a factor of 4 and is the estimated phase in the middle of the block. Since ϕ is retrieved after phase unwrapping, it has multiple of 2π ambiguity and the final phase estimation has a phase ambiguity of multiple $pi/2$, which is called cycle slip. When phase noise is relatively large, the estimated phase has a high probability to suffer cycle slip.

The error due to cycle slip can be compensated by applying differential encoding of transmitted symbols, however, accompanied by coding penalty[61]. Cycle slip correction techniques were proposed[62] with a sliding average filter, but only applicable in low noise conditions. Other phase estimation methods, such as feedforward filtering[46] and blind phase search (BPS) algorithm[63] then proposed for improved estimation accuracy but significantly increased the computation complexity. Joint phase estimation methods were also proposed for multichannel phase estimation by applying BPS over all channels[64] with a decrease in computation cost for each channel. Unfortunately, even with these, the overall computation cost was not acceptable in practical receivers with high bandwidths.

Motivated by the fact that the phase noise on different channels are highly correlated, three low-complexity phase noise compensation algorithms, i.e. sequential nulling method, pilot channel method and two-stage joint phase noise compensation method, are proposed to suppress phase noise for the hybrid OFDM receiver. The corresponding principles and performance characterized by error-vector-magnitude are described as follows.

4.6.1 Sequential nulling method

In case when 4QAM modulation format is used, the degradation of the phase noise can be mitigated by applying M-th power algorithm (also known as Viterbi-Viterbi algorithm) [65]. However, in the proposed sub-sampling scheme, the system pauses for 500 ns until the next DFT sample window capture so that the continuous phase drift estimation may encounter unwrapping errors. Fortunately, the fact that the major phase noise is seeded by the FWM process suggests that the phase noise on different channels should be highly correlated, especially for neighboring channels. Motivated by this fact, one can directly estimate the phase error of a specific channel with the phase error of a neighboring channel. For example, the

knowledge of the exact phase error $\Delta\theta^{(59)}$ on the 59th channel, allows subtraction $\Delta\theta^{(59)}$ from the phase of 60th channel removal of decoding penalty, as shown in Figure. 4-7 (a). While retrieving the exact phase error of a symbol imprinted onto high order tones might pose the challenge, it is easy to recognize that a reference tone (seeding master tone) possesses minimal phase noise, allowing for sequential phase error estimation for all subsequent channels. Without backplane suppression of the phase noise, hybrid receiver construction should incorporate physical suppression of phase noise scaling.

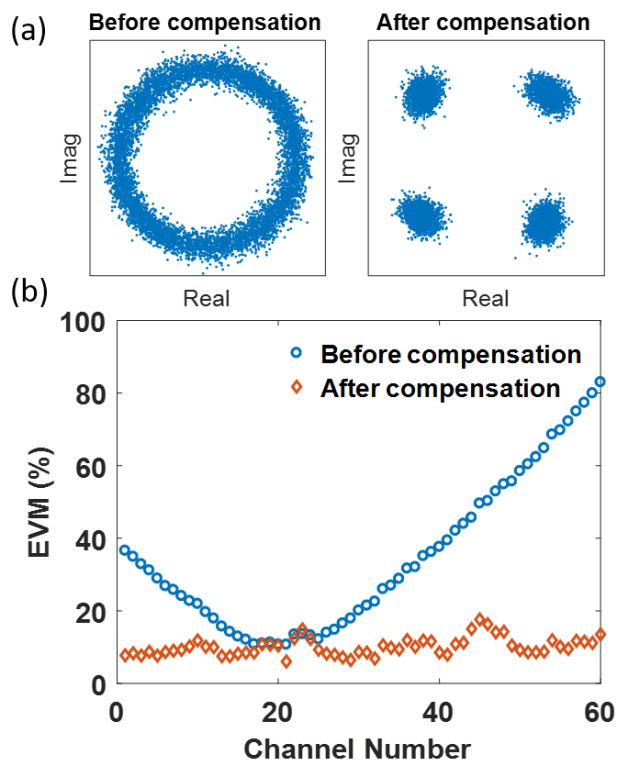

Figure. 4-7 Constellation of the 60th (15.8 GHz) channel before (left) and after (right) phase noise compensation with phase error on the 59th channel. (b) EVM of all 60 channels before and after phase noise compensation in a sequential nulling process.

In this example, the process was initiated with the seeding channel, i.e. 8 GHz channel (21st out of 60 channels of the receiver), and the phase error $\widehat{\Delta\theta}^{(21)}$ was estimated by mapping detected symbols to the closest modulation constellation. The common phase error (CPE) term

was compensated using 8 pilot symbols. Subsequently, $\widehat{\Delta\theta}^{(21)}$ was subtracted from the observed phase of 22nd channel $\theta^{(22)}$ and the modified symbols with phase $\theta^{(22)} - \widehat{\Delta\theta}^{(21)}$ were then mapped to the closest modulation constellation to estimate the phase error $\widehat{\Delta\theta}^{(22)}$. An identical process was repeated for all 60 channels and the same technique can be used for descending channel count down to the 1st channel. Figure. 4-7 (b) showed significant EVM reduction for all high order channels after phase noise compensation in the case when no additional white Gaussian noise was injected.

The inherent advantage of the phase noise compensation scheme described here is that only few pilots are required (8 out of 8000 symbols act as pilots) implying the ability to maintain low latency and low overhead. It is noted that only low complexity computational operations, phase detection and subtraction, are required. However, the phase noise compensation still represents a sequential nulling process that allows for incorrect phase error estimation to propagate over all subsequent channels. This estimation error can be severe at higher-order channels or, when estimates are poor, correspond to the low SNR condition. To improve the accuracy of phase error estimation, it is beneficial to apply additional phase recovery algorithms akin to M-th power method before extracting the phase error used for the subsequent channel.

4.6.2 Pilot channels method

Alternatively, similar to a traditional OFDM scheme, all symbols in selected channels served as pilots to improve phase recovery performance. As explained before, the phase noise on different channels should be highly correlated through FWM process so that a simple linear estimator could efficiently estimate phase error on each channel with the information of pilot channels.

More importantly, the phase error at the receiver end did not rely on the received signal logic state, implying that the linear estimator can be trained prior to the operation, thus greatly reducing the required computation load during real-time demodulation. In this experiment, the first (4 GHz) and the last channel (15.8 GHz) were selected as pilot channels and a linear estimator can be constructed as $\widehat{\Delta\boldsymbol{\Theta}} = \hat{A} \cdot \Delta\boldsymbol{\Theta}_{pilot}$ from an approximate linear model:

$$\Delta\boldsymbol{\Theta} = A \cdot \Delta\boldsymbol{\Theta}_{pilot} + \boldsymbol{\varepsilon}, \Delta\boldsymbol{\Theta}_{pilot} = \begin{bmatrix} \Delta\theta^{(1)} \\ \Delta\theta^{(60)} \\ 1 \end{bmatrix} \tag{4.2}$$

where $\Delta\boldsymbol{\Theta} = [\,\Delta\theta^{(2)}, \Delta\theta^{(3)}, \ldots, \Delta\theta^{(59)}]^T$ is an array of phase error on the 2nd channel to the 59th channel, A is a 58×3 matrix to transform phase noise on pilot channels to objective channels and $\boldsymbol{\varepsilon}$ is a noise term. $\hat{A}$ was an estimate of A and was calculated in advance with least square method from 8000 training symbols in the case of SNR = 19.8 dB.

The performance of the comb-assisted OFDM receiver is characterized by EVM measurement. For 4-QAM modulated signal, accompanied by the white Gaussian noise, the theoretical EVM performance can be directly calculated as [66]:

$$EVM \approx \sqrt{1/_{SNR}} \tag{4.3}$$

If all channels have the same SNR, the average EVM of all channels share the same relationship. As a comparison, back-to-back measurements were performed by directly quantizing and demodulating the OFDM signal with real-time oscilloscope possessing 20 GHz physical bandwidth and calculated the average EVM of all channels (Figure. 4-8). An excellent agreement between back-to-back measurement and theory verified the need for SNR equalization for each channel. With phase noise compensation described here, EVM of each channel was calculated by demodulating 8000 symbols and the average EVM of all channels was plotted in Figure. 4-8 for different noise levels. At high SNR region, the comb-assisted

receiver has roughly 3.6 dB penalty, when compared to ideal-receiver model. As SNR was decreased, the EVM performance with sequential nulling phase compensation worsened significantly due to higher probability of propagating incorrect phase error estimates over subsequent channels, allowing symbol errors to accumulate. With two channel pilots and pre-trained linear estimator, the phase noise were well compensated and EVM dropped entirely, in contrast to the sequential nulling method. Consequently, it is recognized that the residual SNR penalty of the OFDM receiver originated from the electronics backplane including TIAs and sample-and-hold circuits.

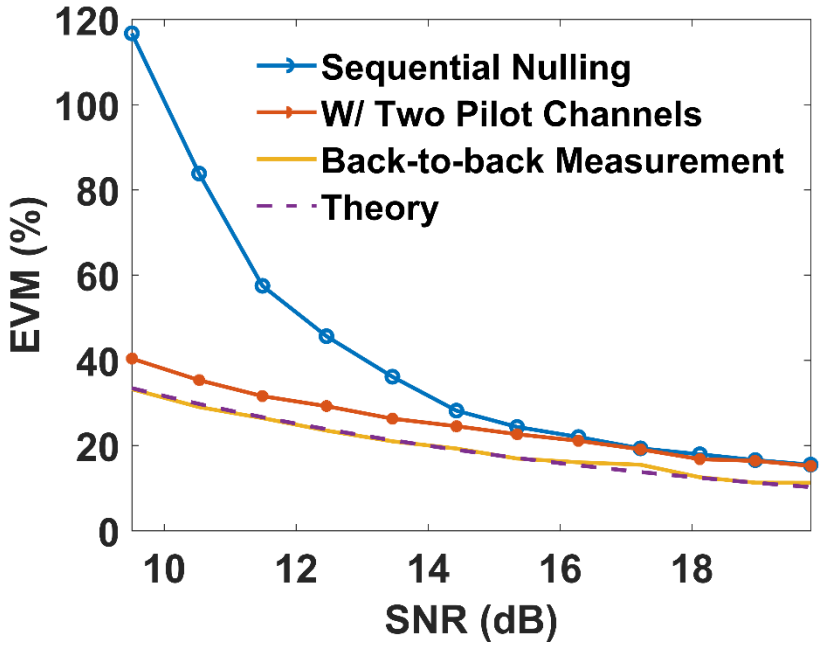

Figure. 4-8 Error vector magnitude of comb-assisted OFDM receiver with sequential nulling method and pilot channels method compared to a back-to-back measurement and theory.

4.6.3 Joint compensation method

The previous phase estimation methods, blind (sequential nulling method) and pilot-aided (pilot channels method), were both proposed by exploring the correlation of phase noise of each channel. However, blind phase estimation, though at low computation cost, failed at low

signal-to-noise ratio due to accumulated phase noise at high order tones. Pilot-aided phase estimation required at least two pilot channels, decreasing transmission rate and induced additional complexity due to pilot arrangement and linear estimator construction. In this section, a two-stage phase estimation scheme applicable to variable SNR conditions and without reliance on pilot channels is proposed.

Due to quadratic phase noise scaling (Figure. 4-6 (b)) over comb mode order, the simple V-V algorithm failed due to cycle slips when using high order tones. Recognizing the fact that the phase noise of all channels are correlated, especially for high order comb mode channels Figure. 4-6 (a)), here a two-stage joint phase estimation algorithm is proposed to correct cycle slip as shown in Figure. 4-9 (a).

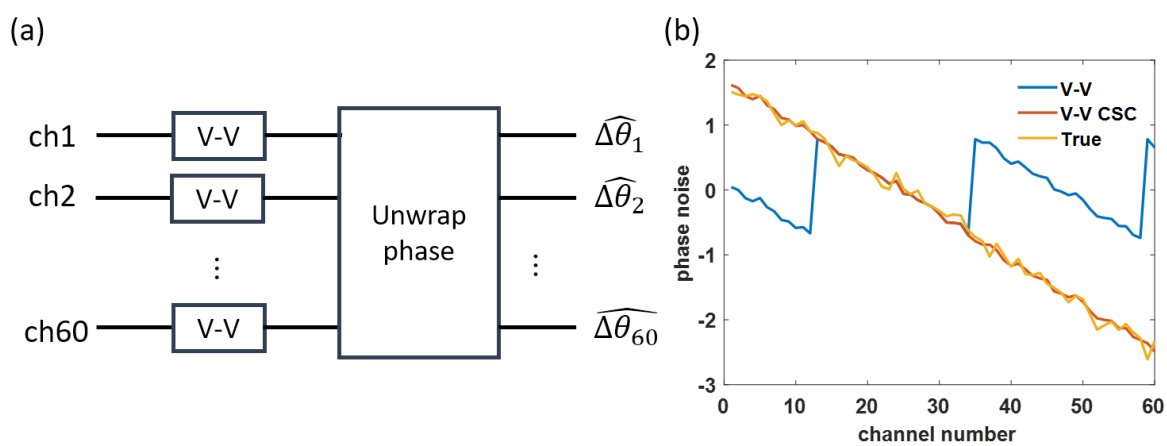

Figure. 4-9 (a) two stage joint phase estimation scheme. $\widehat{\Delta\theta_i}$ represents the phase noise estimation of i-th channel. (b) phase noise estimation of a symbol over all 60 channels. Blue line is phase estimated by Viterbi-Viterbi (V-V) and red line is estimated with V-V with cycle slip correction (V-V CSC). The yellow curve represents the true phase error for that symbol.

In the first stage, simple V-V algorithm was applied on each channel to estimate the phase noise. For low order channels, phase noise was small such that the probability of cycle slip is extremely low. For high order channels, since the phase noise scales quasi quadratically, cycle slip occurred at high probability. Figure. 4-9 (b) illustrates the phase noise of a specific

symbol suffered from cycle slip after applying V-V phase estimation (blue line). However, since phase noise are highly correlated, the true phase noise indicated a quasi-linear function of channel number. Therefore in the second stage, the estimated phase noise generated from the first stage was directly unwrapped. But unlike common phase unwrapping methods, the unwrapping starting at 21st channel, i.e. the channel with lowest phase noise. Specifically, estimated phase noise was unwrapped from channel 21 to channel 1 and channel 21 to channel 60 respectively and the two unwrapped phase noise estimation were concatenated. Unwrapping effectively corrected the cycle slips that occurred in the first stage and matches well with the true phase noise (Figure. 4-9 (b)).

As compared to the blind phase noise estimation method which was only applicable in high SNR conditions, the proposed method was robust within the whole SNR range under test. This method achieved similar performance compared to the pilot-aided method without using any pilot channels, avoiding pilot arrangement and transmission rate penalty. The effectiveness of this method relies on linear relation between phase of beating comb tones and comb mode order. Besides, the proposed method consists of simple V-V algorithm and phase unwrapping operations to correct cycle slips so the computation complexity and latency are very low and suitable for real-time implementation.

4.7 Summary

In this chapter a new wideband OFDM receiver relying on dual-comb assisted DFT processor is proposed and tested. Without the need for high bandwidth ADCs and high-throughput, high-precision digital DFT processor, DFT generation was performed during coherent detection with two high fidelity combs, circumventing full-rate quantization. Sample-and-hold circuits were used to digitize simultaneously generated DFT coefficients and time-

multiplex the output before decoding the payload. The precision of the DFT processor is characterized by reconstructing and demodulating an 8-PPM signal under varied SNR conditions. When the new hybrid DFT processor served as a core of the OFDM receiver, phase noise has to be suppressed to mitigate phase errors. Using sequential nulling method or pilot channels can effectively suppress phase noise and the corresponding performance was characterized by measuring EVM performance under various SNR conditions. However, the sequential nulling method is only applicable in the high SNR conditions and using pilot channels increases system complexity for pilot arrangement while inducing transmission rate penalty. A two-stage joint phase noise compensation algorithm is proposed to estimate the phase noise of each channel via Viterbi-Viterbi algorithm and jointly unwrap the estimated phase over all channels. Characterized by average EVM of recovered symbols, while not relying on pilot channels, the new method achieved comparable phase noise compensation performance with previous pilot-aided channels. While no physical mechanisms were used to suppress inherent phase noise across signal-LO combs, the throughput of such (raw) OFDM receiver can be further enhanced by deploying significantly more subcarriers and higher modulation format while maintaining flexibility and tunability.

Chapter 4, in part, is a reprint of the materials as it appears in *Journal of Lightwave Technology* volume 37, issue 4, 1280-1287 (2019), titled "Realtime comb-assisted discrete Fourier transform processor" authored by Huan Hu, Vahid Ataie, Evgeny Myslivets, and Stojan Radic. The dissertation author was the primary investigator and the primary author of this article.

Chapter 4, in part, is a reprint of the materials as it appears in *Conference on Lasers and Electro-Optics Pacific Rim (2018)* titled "Realtime comb-assisted discrete Fourier transform

processor" authored by Huan Hu, Vahid Ataie, Evgeny Myslivets, and Stojan Radic. The dissertation author was the primary investigator and the primary author of this article.

Chapter 4, in part, is a reprint of the materials currently being submitted for publication as it may appear in the IEEE Photonics Technology Letters, titled "Joint Phase Noise Compensation in Dual-comb Assisted OFDM Receiver" authored by Huan Hu, and Stojan Radic. The dissertation author was the primary investigator and the primary author of this article.

Chapter 5 Comb Assisted RF Receivers with Reduced Complexity

The hybrid dual-comb assisted DFT processor has been demonstrated in chapter 3 and an ultra-wideband OFDM receiver relying on the hybrid DFT processor is demonstrated and characterized in chapter 4. Comb-assisted processor significantly relieves the complexity of DFT computation since it eliminates full-rate front-end quantization and high-speed FFT computation. However, the system is still complex and costly, which motivates for reduced complexity implementations. Firstly, the DFT processor requires two mutually coherent high-fidelity combs utilizing identical comb generation principles but with different RF oscillators. It motivates the use of a single comb, with a split and delay topology equivalent to dual-comb operation, to implement the hybrid DFT processor. Secondly, the DFT computation of the proposed hybrid DFT processor is effectively parallelized by using parallel heterodyne detection, enabling the rate scaling of the aggregate throughput. But in many ultra-wideband scenarios, the full information of DFT coefficients are redundant. With compressed sensing algorithms, it is viable to use partial DFT coefficients for signal reception and processing, reducing the system complexity.

In this chapter, a new hybrid DFT processor assisted by a variable frequency comb is proposed and the dual-comb photonic front end was replaced by a single comb split into two switched paths to achieve spectral decomposition. The performance is characterized by demodulation of 4QAM modulated OFDM signals. Based on the new architecture, sub-Nyquist ultra-wideband sparse signal reception is demonstrated without using fully populated backend including optical comb tones, coherent receivers, etc.

5.1 Hybrid DFT processor with a variable frequency comb

OFDM also plays an important role in ultra-wide-band (UWB) radio frequency (RF) applications that include signal detection, remote sensing and waveform processing[67]–[69]. The key technology for current and future OFDM communication systems and UWB RF applications is the high-rate, high-precision digital DFT processor capable of mapping digitized waveform to Fourier domain in real-time. As described in previous chapters, the conventional, all-electronic OFDM receivers face both fundamental and practical challenges. Firstly, silicon DFT processor faces computation limit inherent with maximal transistor density, imposed by quantum and thermal effects [2]. This limit widely recognized after breakdown of Moore's Law and Dennard scaling, has served as one of the principal motivations for renewed interest in physically assisted processor topologies. In addition to a need for fast DFT processors, wideband OFDM receiver also mandates that received waveform is digitized by a full rate ADC which imposes basic dissipation limitations and requires a tradeoff between speed and quantization precision[3].

To address these concerns, photonic-assisted DFT processor based on a dual phase-locked optical parametric combs was proposed and demonstrated in conjunction with high-throughput, high-precision architecture [20], [50]. Following this approach, OFDM receiver based on dual-comb techniques eliminated a need for full-rate ADCs in order to demodulate wideband 4-QAM OFDM signals with simple digital signal processing (DSP) technique [20]. However, this approach still relied on dual Verniered combs that ultimately double the dissipation and complexity of single-comb systems.

To overcome this limitation, this section describes OFDM receiver in which DFT processor relies on a single frequency comb for the first time, to the best of the author’s knowledge. To eliminate two-comb architecture, a single comb is used in frequency switching

regime, effectively halving the complexity of the receiver. This work also directly experimentally demonstrates the tunability of a parametric comb generated through shockwave engineering, a feature generally prohibited by cavity-based comb devices. This approach is more general than OFDM decoding reported here and can be easily modified to address other applications that rely on use of dual-combs in detection[50], ranging[48], [70] and spectrometry[49], [71], [72]. The use of the new architecture as OFDM receiver is demonstrated by demodulating 4-QAM OFDM signal with 50 subcarriers positioned between 3 GHz and 7.9 GHz, separated by 100MHz. The receiver design is described, and the performance of the single variable comb assisted OFDM receiver is evaluated by measuring EVM at different levels of SNR across the entire operating band.

5.1.1 Principle of operation

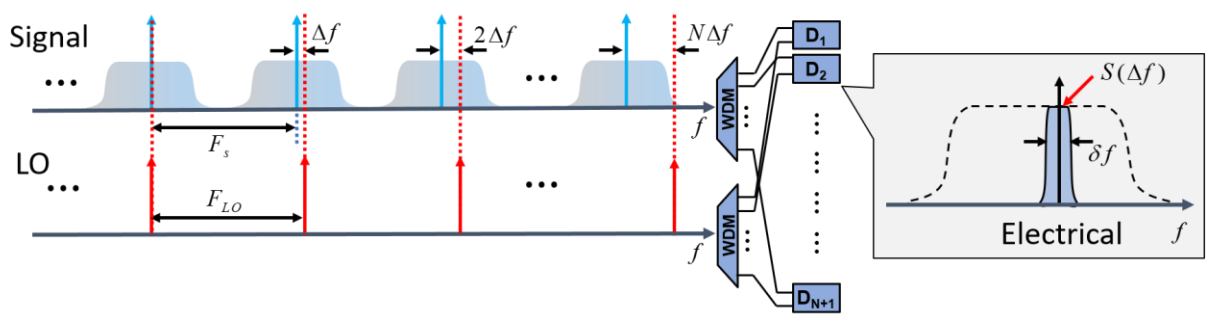

Figure. 5-1 Spectral representation of a DFT processor with dual optical parametric combs. Blue and red arrows are the tones of signal comb with F_s frequency pitch and LO comb with F_{LO} frequency pitch respectively. The input RF signal is modulated on signal comb and effectively replicated onto each comb tone, and the LO comb is used as a probe to select which frequency component of the signal is digitized. Two wavelength division demultiplexers split the replicated signal-LO pairs into individual coherent detectors and sub-band filtering is done by detector element response bandwidth (δf). DC term of down-converted signal represents the DFT coefficient (in the inset, $\boldsymbol{S}(\Delta f)$ is shown as an example of DFT coefficient at Δf).

With the aid of dual, mutually coherent and frequency-Verniered combs, complex DFT coefficients of either optical or electrical signal can be extracted via parallel, sub-rate heterodyne detection[20], as illustrated in Figure. 5-1. When signal $s(t)$ is modulated onto optical comb with frequency pitch F_s, a spectral copy is imposed on each comb tone. When comb tones

possess sufficiently high OSNR and when modulation occurs in linear regime, it is possible to approximate signal copying by noiseless, distortion-free replication in spectral domain. The second, phase-locked comb, acts as a local oscillator (LO) array, possessing a different frequency pitch F_{LO} in order to accomplish spectral Vernier. Each signal-LO comb mode pair can be optically filtered by a wavelength division demultiplexer that has matched, coarse frequency grid and sent to a dedicated, sub-rate coherent detector. Consequently, each detector element will retrieve spectral information at targeted frequency offset, defined by the comb pitch offset $f_{IF} = n \cdot \Delta f$, where n is order number and Δf is frequency pitch offset $(F_{LO} - F_s)$. A coherent detection of each comb mode pair is equivalent to heterodyne detection of a RF signal copy, resulting in frequency shifted baseband signal $s(t)e^{-j2\pi f_{IF}t}$, filtered by the detector response. DFT coefficient $\boldsymbol{S}(f_{IF})$ centered at f_{IF} can be retrieved with a lowpass filter, effectively realized by the detector element response $\delta f (\geq \Delta f)$. As a result, the backplane is composed of sub-rate ADC array, rather than full-rate ADCs. This allows for ADC array precision can be qualitatively increased, enabling alias-free $\boldsymbol{S}(f_{IF})$ acquisition with low-complexity DSP. By capturing a complete set of signal-LO pairs, the recovery of the full-band spectrum $\boldsymbol{S}^{\boldsymbol{full}}(f)$ is guaranteed with frequency domain sampling resolution set by the frequency pitch offset Δf.

If the input signal $s(t)$ is real, the DFT coefficients are conjugate symmetric, i.e. $\boldsymbol{S}(-f_{IF}) = \boldsymbol{S}^*(f_{IF})$. Consequently, if one toggles the frequency pitch of signal and LO combs, the detector element will capture the complex conjugate of the DFT coefficient. This means that, as long as the absolute value of frequency pitch offset is fixed, DFT coefficients can be fully retrieved since each detector captures either the DFT coefficient or its complex conjugate. This also means that a single comb, rather than dual Verniered comb topology can be used to retrieve

DFT coefficients by switching signal and LO comb periodically. When a comb with periodically switched frequency pitch is generated, it is split it into two paths, with one path delayed to match the toggle (switching) interval τ between signal and LO combs, guaranteeing dual-comb operation at any time.

Comb-assisted processor relieves both principal challenges, DFT computation and full-rate quantization. Firstly, selected tones can be filtered simultaneously for parallel heterodyne detection so that DFT computation is effectively parallelized, enabling free rate scaling of the aggregate throughput. Secondly, only sub-rate of the detected signal is needed, allowing for a low-rate ADC backplane with correspondingly high resolution. Thirdly, if OSNR of the signal and LO combs are sufficiently high and modulator operates in linear region, an effective precision of DFT generation can be maintained. Finally, when comb pitch can be freely tuned, the resolution and operating frequency range of DFT decomposition can be freely chosen to meet the input signal requirements. This is particularly important in flexible-band applications, where user should be able to change center frequency and instantaneous bandwidth in a rapid manner.

5.1.2 Comb generation and architecture

Physically assisted DFT processor relies on generation of broadband comb that possess sufficiently high power, OSNR, frequency stability and can tune its frequency pitch rapidly. While multiple optical comb generation techniques were explored, ranging from mode-lock lasers to seeding in micro resonators[73]–[75], to the best of the author's knowledge, only a cavityless class of electro-optic frequency combs [24], [40], [76]–[79] are inherently compatible with pitch tuning requirement. Optical parametric combs generated via shock wave engineering,

represent a specific class of cavityless frequency generators and combine these attributes into a single, travelling-wave platform [24].

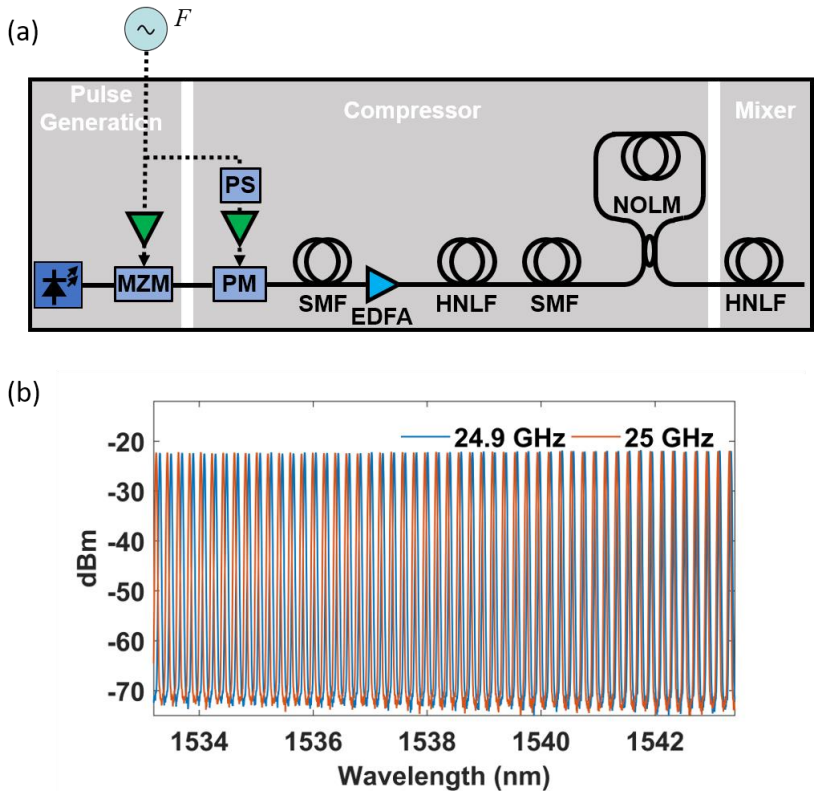

Figure. 5-2 (a) Optical parametric comb generation. MZM: Mach-Zehnder Modulator, PM: Phase modulator, PS: RF phase shifter, SMF: Single mode fiber, EDFA: Erbium doped fiber amplifier, HNLF: Highly nonlinear fiber, NOLM: Nonlinear optical loop mirror. (b) Output comb spectrum with 25 GHz and 24.9 GHz frequency pitch sharing the same setup except for a different clock. The spectral resolution is 0.02 nm and is measured at 1% tap.

Optical parametric combs are generated via four wave mixing process that, when realized in phase-matched regime, operate over wide spectral range exceeding the combined C and L bands. To increase efficiency of FWM process in phase-matching highly nonlinear fiber (HNLF) stage of the parametric mixer, a shock wave with maximized peak power is created, as illustrated in Figure. 5-2 (a). Peak power is scaled by a compressor stage which must precisely manage initial frequency chirp and group velocity dispersion by matching the phase modulation and physical properties of the fiber. Seed mixer pulses are initially generated modulating continuous-wave (CW) master laser harmonics generated by low phase noise clock with

frequency F, using a quadrature biased Mach-Zehnder modulator (MZM). In the front end of this architecture, a phase modulator (PM) driven by a half-wave delayed version of the modulation waveform induces positive chirp. This chirp is matched to negative dispersion in single mode fiber (SMF) in order to take advantage of rising and falling pulse edges with differential group velocity, compressing the original optical pulse width. Subsequently, narrowed pulse train is further compressed in a second stage that combines positive Kerr-induced chirp in high-gamma HNLF and compression in SMF, further scaling the peak power of the optical shock wave. Parasitic side lobes generated in this stage manifest as power fluctuations of the compressed pulse train and are suppressed by regenerative shaping in nonlinear optical loop mirror (NOLM). In final mixer stage that consists of dispersion-flattened HNLF, a broadband comb is generated through efficient, phase-matched FWM process. By changing the clock frequency F, the comb frequency pitch is tuned accordingly with near-instant response. Unlike the conventional electro-optic combs that require complex, precise phase control to generate broadband high-performance combs, shock-wave comb relaxes the complexity as well as strict phase controlling process and allows for a large frequency pitch tunability. More importantly, since both signal-copying and LO combs are generated with identical mixer setup, a stable mutually coherent complementary pair of combs corresponding to dual-comb Vernier is guaranteed. Figure. 5-2 (b) shows two high-OSNR ($OSNR_{0.1nm}$>40dB) combs with minimum -4dBm per tone measured from a 1% output tap. The combs with two different frequency pitches were generated from CW seed laser centered at 1549.3nm with spectral ripple between two being less than 1dB. For the purpose of this report, 50 tones ranging from 1533.3 nm to 1543.3 nm were selected for spectral decomposition of OFDM signal occupying 3 GHz to 7.9 GHz range.

The experiment used an RF switch with 50 ns response time for clock frequency control, as shown in Figure. 5-3. Two complementary rectangular pulse train control signals with $\tau = 1\mu s$ duration were generated from a pulse pattern generator to gate one of the two clocks during the comb generation. The two clocks were set at 24.9 GHz and 25 GHz respectively, corresponding to a DFT resolution of 100MHz. While the scheme eliminates use of the second frequency comb, it also imposes strict requirement with respect to RF switch state leakage (extinction). When isolation between two switched modes is not sufficient, a spurious frequency generates phase noise in either signal-copying or LO comb mode that can be observed as parasitic sidebands adjacent to comb tones. The model corresponding to the architecture in Figure. 5-3 indicates that switched state extinction should be kept above 80dB in order to suppress parasitic sidebands below 40 dB, across 100 generated comb tones. This performance is readily achieved by standard RF switching element and can be easily emulated by concatenating even the lowest-grade commercial devices.

The output of frequency-pitch-switching comb was split by 3dB coupler; a single path incorporated a SMF delay τ in order to guarantee that the frequency pitch offset between two comb modes, defined by two optical paths is 100 MHz, as shown in Figure. 5-3 inset.

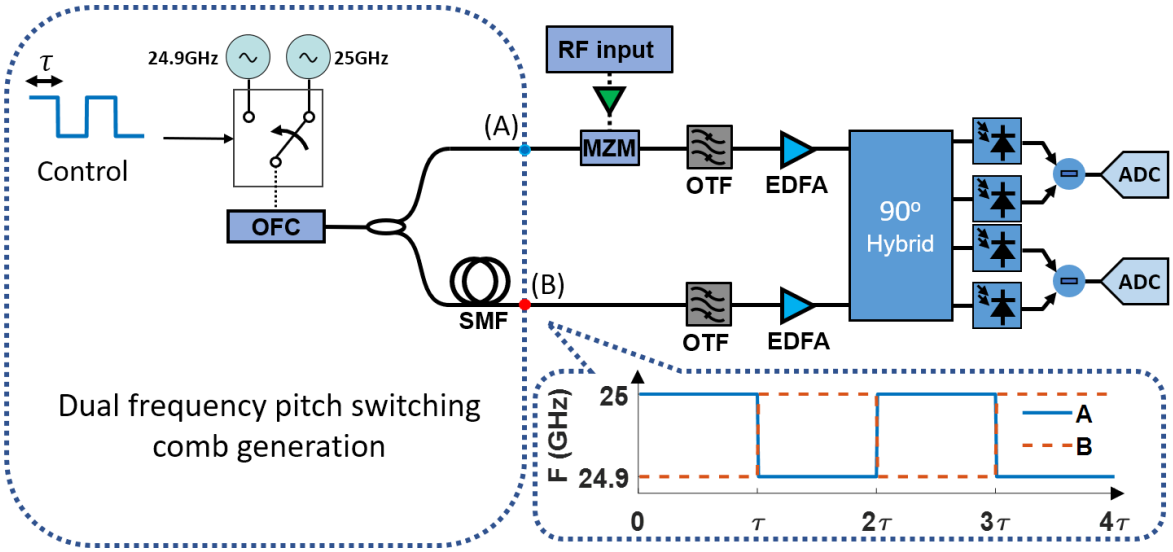

Figure. 5-3 Setups of variable frequency comb assisted OFDM receiver. A control signal with toggling interval τ is generated by a pulse pattern generator to control the driving clock for optical frequency comb (OFC) generation. Frequency pitch offset between two comb modes defined by two optical paths is 100 MHz at any time. OTF: optical tunable filter, EDFA: Erbium doped fiber amplifier, MZM: Mach-Zehnder modulator, SMF: single mode fiber. Inset shows the frequency pitch switching of dual comb at point A (blue solid line) and B (red-dashed line) respectively.

Subsequent to switched comb generation, 50 signal copies were created by modulating comb tones by Mach-Zehnder modulator (MZM), biased at null point. The use of single MZM for all tones raises a potential concern that modulator bias point variance across carrier wavelengths can impose receiver penalty. However, the architecture shown in Figure. 3 was specifically designed to minimize this effect, with no measurable impairment observed, similar to that reported earlier [36]. Indeed, a shifted null-point bias voltage of a signal tone yields a constant additive electric field term with modulated signal copy, allowing for simple backplane compensation for bias correction. Equally important, comb tones possessed sufficiently high OSNR and power, which allowed for highly linear modulation, guaranteeing low-distortion signal replication onto optical carriers.

To demonstrate the operational principle and measure DFT processor performance without fully populated backplane array, WDM block was replaced by optical tunable filter and

used to sweep the band and select corresponding signal-LO tone. By repeating the receiver stimulus, its operation was characterized using a single coherent detector rather than a 50-coherent-detector array, following well-established methodology from lightwave transmission experiments [59], [80] and earlier reports on physically assisted receivers[36]. At the receiver end, an ADC was used to capture the real and imaginary part of frequency-shifted version of the input RF signal. Finally, captured data were synchronized and down-sampled to 100 MS/s using anti-aliasing filter to retrieve the complex DFT coefficients.

5.1.3 OFDM receiver performance

To demonstrate its utility, the new hybrid DFT processor was used for OFDM-encoded signal reception, specifically, it was used for demodulation of 4-QAM OFDM signal with 50 subcarriers separated by 100 MHz, occupying 3 to 7.9 GHz band. OFDM signal was generated using 64 GS/s Digital-to-Analog converter (DAC) with 8-bit resolution, with digital pre-compensation applied to equalize RF power across all subcarriers. To quantify the receiver performance under variable SNR, band-limited Gaussian noise (2.9 GHz to 8 GHz) was injected into the channel, with power controlled by an electrical attenuator. While no cyclic prefix is added to the OFDM signal, the receiver was still compatible with conventional OFDM signals with cyclic prefix by filtering pre-appended prefix in time domain before performing physically assisted DFT decomposition.

For each channel, a waveform block lasting 198 μs were captured and post-processed offline. As an example, Figure. 5-4 shows the reception of the 25th channel within two toggling operation intervals for demodulation at 5.4 GHz at 22.9 dB SNR. Figure. 5-4 (a) showing the in-phase term of frequency-shifted RF signal in one interval and its complex conjugate complements in the other interval. A short blind period of 60 ns occurred and was defined by

the time (~50 ns) required to toggle RF switch, with additional guard band (~10 ns) to account for any optical and electrical path length mismatch. Signal blocks separated by the blind period were used to retrieve DFT coefficients and their complex conjugate complements at 5.4 GHz respectively.

Phase noise causes measurable performance degradation in OFDM systems by inducing common phase error (CPE) and intercarrier interference (ICI). To provide strict performance analysis of the comb-assisted OFDM receiver in presence of phase noise, time and frequency were first synchronized and channel fading was minimized during the measurements. While synchronization and channel estimation[34] are desired in deployed OFDM receivers, with received signal represented in frequency domain[81], [82], such implementation is beyond scope of this section. As a second impairment mechanism inherent to hybrid DFT processor, the phase decorrelation between selected pair of tones can add excess phase noise to the detected OFDM symbol and lead to channel performance degradation, which can be mitigated by applying blind phase compensation algorithms[65]. In addition, phase transition was also observed when comb frequency pitch was switched. The phase transition caused common phase rotation over the subsequent symbols within the switched block period. To address this effect, a single symbol was inserted as a pilot during each switching period to correct discrete phase jump induced by comb toggling. For each switching period lasting $1\mu s$, 93 effective data symbols were captured. With power and phase equalization [29], the constellation comprising of DFT coefficients and their complex conjugate complements are generated and shown in Figure. 5-4 (b) .

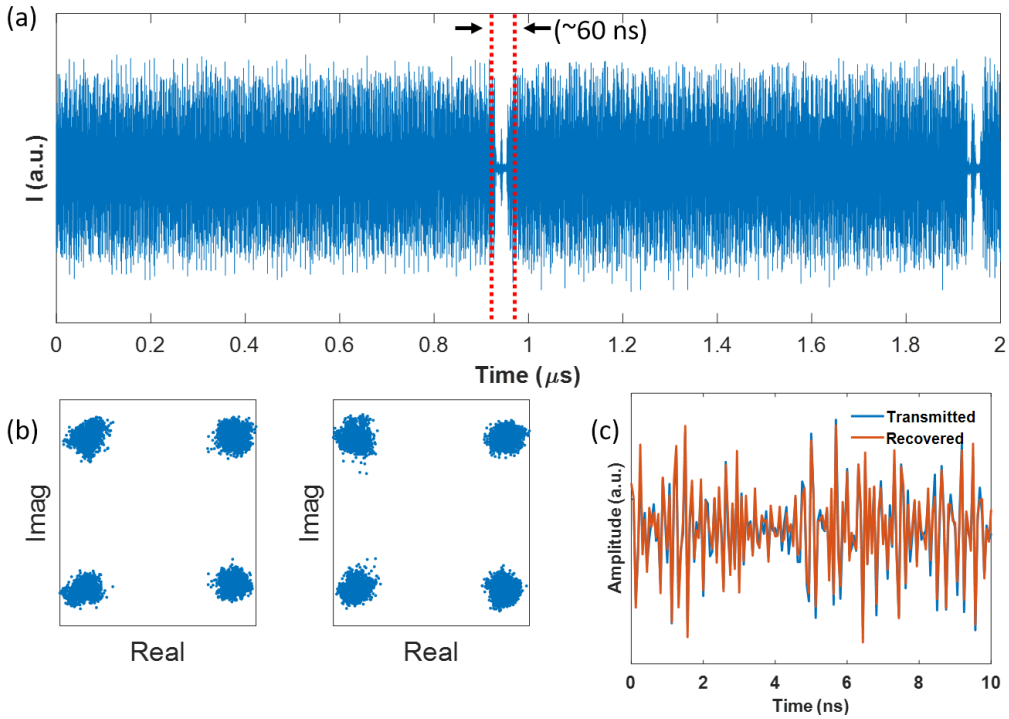

Figure. 5-4 5.5GHz channel reception. (a) Recorded in-phase part of frequency shifted signal within a switch period. The blind period due to frequency switch is around 60ns. (b) captured effective DFT coefficients (left) and complex conjugate DFT coefficients (right) within 198 μs. (c) A recovered OFDM symbol waveform with captured DFT coefficients from 3GHz to 7.9GHz.

The blind period induced by comb toggle comprises an effective 6% overhead of transmitted OFDM signals, reducing the transmission rate by the same amount. The aggregate overhead can be easily decreased by increasing the duration of a switched block period and the length of SMF accordingly. However, this approach is also paid off in terms of increased phase noise between signal and LO pairs. To estimate the decoherence effect, the carrier phase difference $\theta(t+\tau)-\theta(t)$ during an interval τ can be modelled by a Gaussian distribution with a variance[83]:

$$\sigma^2 = 2\pi\Delta\nu\tau \tag{5.1}$$

where $\Delta\nu$ denotes the carrier spectral width. In ideally engineered device, spectral linewidth is conserved across each tone [39] during the parametric comb generation. This means that the phase fluctuation between signal and LO carrier follows Eq. (5.1) and σ then scales as a square

root of switched period duration τ. For 5.4 GHz channel, the measured $\sigma \approx 15°$, which corresponds to an effective linewidth of ~1kHz. With pilot symbol deployment [20], [45], [84] and that enabled DSP technique [46], linewidth requirement can be greatly relaxed, allowing for much longer switched period, also reducing the overall overhead associated with toggled comb architecture. As an alternative, it is also possible to use a faster RF switch that compresses the blind time. The speed of practical RF switch is limited by the physical properties of the switching mechanism or by the limited tuning capability of the resistor inductor capacitor circuits that is being utilized in the switch. Solid-state switches offers nanosecond switching time [85], with state-of-art photonic-enabled switch possessing sub-nanosecond switching time[86].

With capture of all DFT coefficients corresponding to 50 channels, it is possible to recover the time-domain signal with a single inverse Fourier transform (Figure. 5-4 (c)). Comparing with the original waveform, the deviation between recovered and originally transmitted waveform remains remarkably small, indicating that the hybrid OFDM receiver represents a viable alternative to computational (all-electronic) architecture.

The performance of the comb-assisted OFDM receiver was also characterized by error vector magnitude (EVM) measurement. For 4QAM modulated signal, accompanied by white Gaussian noise, the theoretical EVM performance can be directly calculated as $EVM \approx \sqrt{1/_{SNR}}$(Eq. (4.3)) [66]. Since OFDM is a multi-carrier modulation format and all channels are digitally pre-compensated to possess the same SNR, EVM of all channels share the same relationship. In this experiment, EVM of each channel was required by demodulating 18414 symbols and the average value for all channels was plotted in Figure. 5-5 (a) for varying noise

levels. Figure. 5-5 (b) plots the output SNR calculated as $SNR_{out} = 1/EVM^2$ to illustrate SNR penalty of the OFDM receiver.

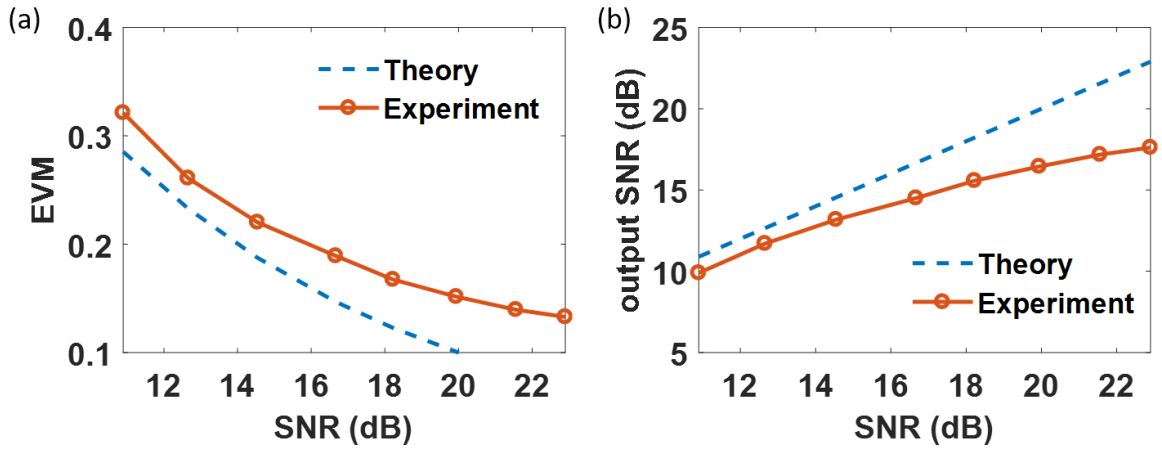

Figure. 5-5 (a) EVM and (b) output SNR performance of OFDM receiver using a variable comb at various SNR conditions.

The SNR penalty increased from 1dB to 5.3dB as input OFDM signal SNR increased from 10.9 dB to 22.9dB. The nonlinear trend of output SNR vs input SNR comes from two folds. On one hand, OFDM is sensitive to phase noise and the SNR degradation is more significant at higher input SNR[87]. The performance can be improved by phase noise suppression in digital domain[44], [88], [89] or physical domain such as using analog or optical phase lock loops (PLLs) or laser source with lower linewidth. On the other hand, at high SNR input regime, measured SNR penalty was dominated by limited receiver carrier power and OSNR. While OFDM signal had high peak-to-average power ratio (PAPR), to avoid modulation-induced distortion, input signal peak-to-peak voltage was maintained within the linear modulation limit (~1.2V), i.e. well below half-wave voltage of modulator (4.5V). As a result, after modulating RF signal onto comb tones, each signal copy had low power, limiting the optical coherent detection sensitivity. The detection was limited by optical noise which was comparable to noise induced at the RF input port. Consequently, the use of optical comb with higher OSNR and

increased tonal power is a straightforward method to improve the receiver performance when operating in high SNR condition. Modern PAPR reduction techniques[90], [91] for wireless OFDM signal can be directly applied to enhance the power of optical signal copy and suppress noise. However, in practical terms, OFDM receivers are expected to operate in low-SNR regime in most applications, nearly eliminating the need for higher performance comb.

5.1.4 Discussion

This section describes the design and test of a novel physically-assisted, hybrid wideband OFDM receiver that relies on single comb to generate DFT coefficients in low hardware complexity manner. The need for a dual, Verniered frequency combs was eliminated by toggling the frequency of a single physical device and harnessing it in split-and-delay topology, realizing the equivalent of dual comb assisted OFDM receiver operation. The receiver circumvents the need for high bandwidth ADCs and high-throughput, high-precision digital DFT processor; instead, Fourier mapping was performed via coherent detection. As a demonstration, the new OFDM receiver was constructed and characterized by measuring its EVM performance and SNR penalty within operational band 3 -7.9GHz, using 4-QAM modulated OFDM signal at varying noise levels. The measurements indicate that the SNR penalty can be reduced to 1dB in low SNR region and becomes considerable in high SNR region where optical noise defined by the carrier spectral purity is dominant. DFT processor throughput can be enhanced in a straightforward manner by simply increasing the number of subcarriers, which means OFDM link reach and capacity can be scaled considerably beyond this report that utilized 50 comb tones. Besides, the proposed hybrid OFDM receiver can potentially share the mature coherent optical transmission techniques[92], [93], to scale to support higher-level modulation format. Indeed, by combining both higher-count tone combs[59] and increasing the

tone OSNR, the performance of OFDM receiver can be scaled well beyond any RF band of interest.

5.2 Sub-Nyquist ultra-wideband sparse signal reception

Ultra-wide-band techniques play an important role in modern wireless communication and detection. Increasing demand for UWB systems with low power consumption motivates the search of innovative analog-to-digital converters (ADCs), which imposes basic dissipation limits and forces tradeoff between speed and quantization precision. One way to overcome this barrier is to design a front-end that combines several low-rate ADCs to provide full-rate operation, such as time-interleaving structure [94] and multi-channel filter-bank approach [11]. In these approaches, the system still operates at Nyquist rate, so the total performance improvement is limited. Apart from the ADC bottleneck, large data volume generated at Nyquist rate quantizer introduces practical challenges for data distribution, both for postprocessing and storage.

To address these, sub-Nyquist sampling architectures based on compressive sensing (CS) has been extensively studied for UWB signal reception and signal processing [95], [96]. The main idea relies on the fact that many UWB signals of interest are sparse [97] and can be recovered from an underdetermined linear system in a computationally efficient way. In this context, "sparse" means that signals x can be decomposed to a sparse representation in certain basis $x = \Psi s$, where the support s only has few non-zero values and Ψ is the decomposition basis. All-electronic hardware systems have been built and demonstrated mainly using non-uniform sampling [98], [99], random demodulation [100], [101] and modulated wideband converter architectures [102], [103]. These efforts aimed at a reduced sampling rate, i.e. sub-Nyquist rate, by designing appropriate underdetermined measurement matrix Φ so that only few

measurements $y = \Phi x = \Phi\Psi s$ are required for recovery of signal x or support s. However, these systems inevitably require high-bandwidth front-end and impose practical difficulties for UWB signal reception. For example, frequency coverage of a CS-based ADC can reconstruct signals at frequencies up to 3.8 GHz [104].

Photonics-based compressive sensing systems extend the maximum bandwidth of operation by using broadband electro-optical components and low-jitter laser sampling sources. For example, photonic random sampling are demonstrated for multi-tone signal recovery up to 20 GHz [105]. Other photonic compressive techniques rely on implementing measurement matrices in optical domain by modulating and mixing the input RF signal with appropriately designed patterns using spatial light modulators (SLM), fiber-coupled modulators, wavelength division multiplexers (WDM) and multi-mode waveguide speckle patterns [106]–[113], operating at sub-Nyquist sampling rate. Early photonic CS recovery demonstrations with an array of SLMs was realized in [106]. This approach requires signals to be periodic and synchronized with low speed SLM modulation, rendering its use in recovery of very limited signal set. Using intensity modulators and WDM band splitters, input signal is modulated, mapped onto various optical carriers and mixed with different encoded patterns via subsequent modulators [107]–[109]. These systems are subject to similar limitations occurred in electronic CS systems due to noise and jitter in the electronic pattern generators. These limitations can be relaxed with time-stretch techniques and optical sampling for UWB signal recovery [110]–[112]. Unfortunately, these schemes are only applicable for long duration signals that allow for collection of enough optical samples for accurate recovery. Recently, photonic CS measurements were taken in parallelized manner using speckle patterns generated through

multimode waveguide [113] and an array of ADCs. However, speckle pattern stability issues limited the signal recovery for high-bandwidth signals.

Recognizing both practical and fundamental limits imposed on these approaches, this report describes new, photonic compressive sensing topology. It introduces first, to the best of the author's knowledge, sparse UWB signal recovery with direct sub-sampling in the frequency domain. The new architecture does not rely on high-bandwidth electronic front-end and is applicable to non-periodic UWB signal reception while retaining sub-Nyquist, high throughput and continuous capture. A variable-pitch frequency comb was used to retrieve DFT coefficients with high fidelity with only sub-rate ADCs. Only a fraction of these coefficients were sufficient for UWB RF signal recovery, sparse in an appropriate domain with compressive sensing. Specifically, our measurement matrix Φ was partial Fourier matrix, which was mathematically proven to be stable for robust signal recovery with CS [114]. The new technique does not rely on high-speed electronic pattern generators or full-rate ADCs, making the proposed scheme immune to electronic noise and jitter, as reported in past studies. In contrast to schemes relying on time-stretch and optical sampling techniques [115], the new receiver operates in a continuous capture mode and is suitable for rapidly varying signal patterns. Finally, since a comb-assisted DFT processor requires only a subset of DFT coefficients, implementation is amenable to reduced hardware complexity, decimating the number of optical carriers, coherent detectors, ADCs and filters.

5.2.1 Principle of operation

Comb assisted CS recovery of UWB signal relies on both comb-assisted DFT processor and CS theory. The principle of comb-assisted DFT processor has been described in chapter 5.1.1. With the aid of dual, mutually coherent and frequency-Verniered combs, complex DFT

coefficients of either optical or electrical signal can be extracted via parallel, sub-rate heterodyne detection arrays as shown in Figure. 5-6 (a). Comb-assisted processor relieves principal and practical challenges of high throughput DFT computation and full-rate quantization. Firstly, selected tones can be filtered simultaneously for parallel heterodyne detection so that DFT computation is effectively parallelized, enabling linear scaling of the aggregate throughput. Secondly, sub-rate ADC backplane are sufficient for high precision operation, when OSNR of the signal and LO combs are sufficiently high and modulator operates in linear region. Finally, with freely tunable comb pitch, the resolution and operating frequency of DFT decomposition can also be freely chosen to meet the input signal requirements. This is particularly important in flexible-band applications, such as the CS receiver of interest here, where a predefined subset of DFT coefficients are required, significantly reducing the hardware complexity in terms of optical carriers and coherent receivers.

Compressed sensing has been successfully applied in multiple disciplines during the last decade. This section briefly reviews the core CS ideas applicable to the new receiver; a more comprehensive description can be found in [116].

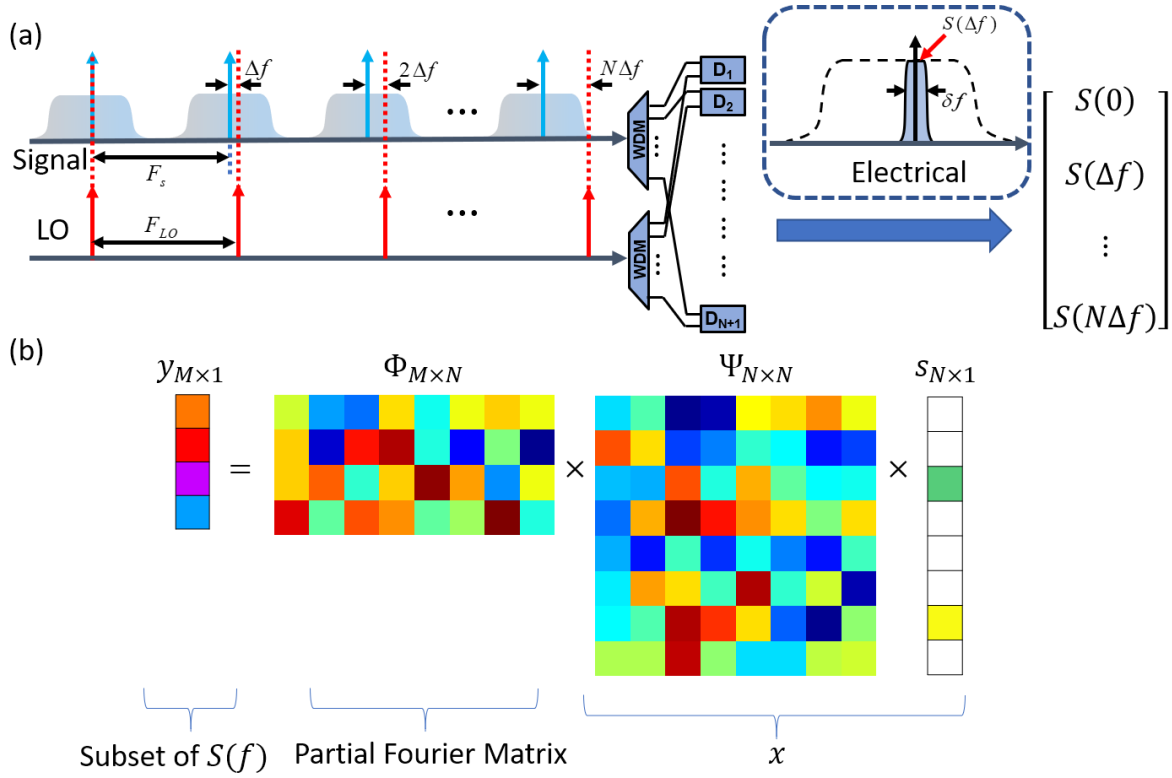

Figure. 5-6 (a)Spectral representation of a DFT processor with dual optical frequency combs. Blue and red arrows are the tones of signal comb with F_s frequency pitch and LO comb with F_{LO} frequency pitch respectively. The input RF signal is modulated on the signal comb and replicated onto each comb tone and the LO comb is used as probe to select which frequency component of the signal to be digitized. Two wavelength division demultiplexers split the replicated signal LO pairs into individual coherent detectors and sub-band filtering is done by detector element response bandwidth (δf). DC term of down-converted signal represents the DFT coefficient (in the inset, $\boldsymbol{S}(\Delta f)$ is shown as an example of DFT coefficient at Δf). (b) compressive sensing model illustration with $K = 2$ nonzero values in support s.

Within the CS framework, real-valued signal $x \in \boldsymbol{R}^{N\times 1}$ can be decomposed to representation in certain basis Ψ, i.e. $x = \sum_{i=1}^{N} s_i \psi_i$ where s is the coefficient sequence of x. In matrix representation, that is $x = \Psi s$ where Ψ is the $N \times N$ matrix with $\psi_1, \dots, .\psi_N$ as columns. Signal is said to be K sparse in the Ψ domain if there are only $K(K \ll N)$ elements in s that are nonzeros. If the signal arrives at the receiver and is processed by linear measurement matrix $\Phi \in \boldsymbol{C}^{M\times N}$ with $M < N$, the received signal is $y = \Phi x = \Phi\Psi s = \Theta s$ where Θ is called sensing matrix. Though recovery of $s(or\ x)$ form y is an underdetermined problem, exact recovery of K-sparse signal can be guaranteed if the sensing matrix Θ satisfy restricted isometry property

(RIP) and incoherence property[117]. The number of measurements required for accurate reconstruction in such way is approximate $K \cdot \log_2(1 + N/K)$[118]. The recovery problem is then formulated to search the sparsest solution of s, i.e.:

$$\min_s \|s\|_0 \text{ subject to } y = \Theta s \tag{5.2}$$

where $\|\cdot\|_0$ is the l_0 norm, counting the nonzero entries.

In the proposed compressed UWB signal receiver, by selecting a subset $y \in \boldsymbol{C}^{M\times 1}$of DFT coefficients, the measurement matrix $\Phi \in \mathbf{C}^{\mathrm{M}\times\mathrm{N}}$ is constructed physically by simply selecting corresponding M rows from a $N \times N$ Fourier matrix (Figure. 5-6 (b)). The sensing matrix can also be constructed for sparse representation in various transform domains [97] or determined by learning from training signals [119], [120] for more general and robust compressed signal reception. In this work, the representation basis Ψ is pre-constructed by selecting ψ_i from bandpass-filtered (3 GHz to7.9 GHz) Gaussian distributed signals to match the operation bandwidth of our receiver. The basis matrix then satisfies the RIP and coherence property with high probability, enabling recovery of the received signal from compressive measurements $y = \Phi\Psi s$ with computational feasible algorithms [116], [121]–[124].

By combing hybrid DFT processor and CS algorithms, physical receiver requirements on UWB signal reception are relaxed. First, with the hybrid DFT processor, information of signal of interest can be fully captured by simultaneously measuring DFT coefficient with sub-rate ADCs, without digitizing the waveform by a full rate ADC. Secondly, without physically constructing a full array of coherent detectors and sub-rate ADCs to capture the complete set of DFT coefficients, the hardware complexity of comb assisted receiver can be greatly reduced by only selecting a subset of DFT coefficients, benefiting from CS techniques. As a result, this approach offers a continuous-time, sub-Nyquist sampled sparse signal recovery without the need

of high bandwidth electronic links in the backend, relaxing the jitter and noise limit imposed on conventional high-speed sparse signal reception systems.

5.2.2 Architecture

In this experiment, the DFT processor uses variable optical frequency combs platforms described in chapter 5.1. Physically assisted DFT processor relies on generation of broadband comb that possess sufficiently high power, OSNR, frequency stability and can tune its frequency pitch in a rapid manner. To meet the requirements, optical parametric combs generated via shock wave engineering, represent a specific class of cavityless frequency generators inherently compatible with pitch tuning requirement.

In contrast to conventional electro-optic combs that require complex, precise phase control to generate broadband high-performance combs, shock-wave comb relaxes the complexity and eliminates strict absolute phase control while simultaneously allowing for a large frequency pitch tunability. More importantly, since both signal-copying and LO combs are generated with identical mixer setup, a stable mutually coherent complement corresponding to dual-comb Vernier is guaranteed. Figure. 5-7 shows two high-OSNR (>40dB) combs with minimum -4dBm per tone measured from a 1% output tap. The 24.9 GHz and 25 GHz combs were generated from a single narrow linewidth (<3kHz) CW seed laser centered at 1549.3nm using clocks working at 24.9GHz and 25GHz respectively. The spectral ripple of both two combs being less than 1dB and the tonal power difference of each signal-LO tone pair are also less than 1dB. For the purpose of this report, 50 tones ranging from 1533.3 nm to 1543.3 nm were selected for capturing DFT coefficients of RF signals occupying 3 GHz to 7.9 GHz range.

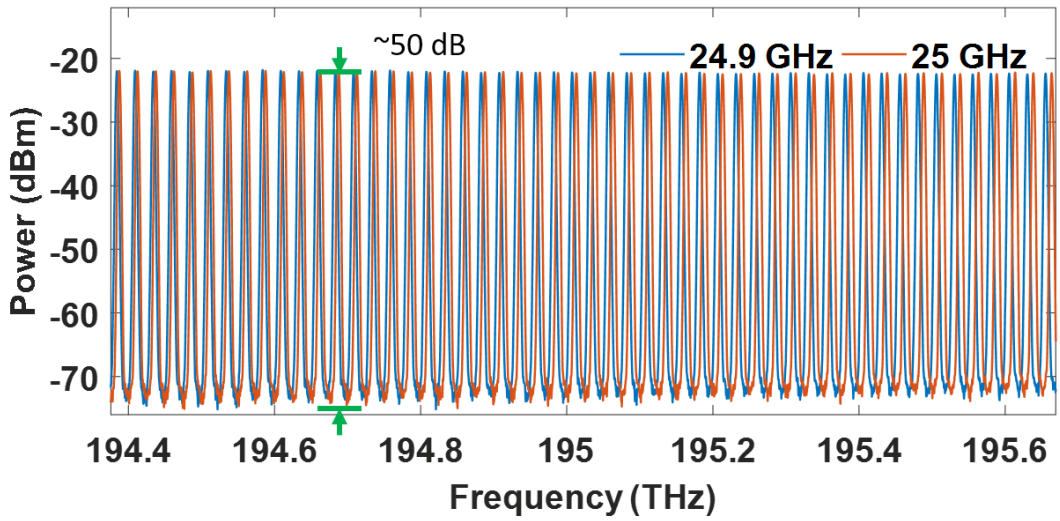

Figure. 5-7 Output comb spectrum with 25 GHz and 24.9 GHz frequency pitch sharing identical setup except for driving clock. The spectral resolution is 0.02 nm and is measured at 1% tap. OSNR is more than $40dB_{0.1nm}$.

In order to enable dual-comb operation with a single variable comb, two RF switches with 50 ns response time are used for clock frequency control as shown in Figure. 5-8. Two complementary rectangular pulse train control signals with $\tau = 1\mu s$ duration were generated from a pulse pattern generator to gate one of the two clocks to drive optical comb periodically. The two clocks were set at 24.9 GHz and 25 GHz respectively, corresponding to a DFT resolution of 100MHz. The output of optical frequency comb with variable frequency was split by 3dB coupler; a single path incorporated a SMF delay τ in order to guarantee that the frequency pitch offset between two comb modes, defined by two optical paths is 100 MHz, as shown in inset of Figure. 5-8.

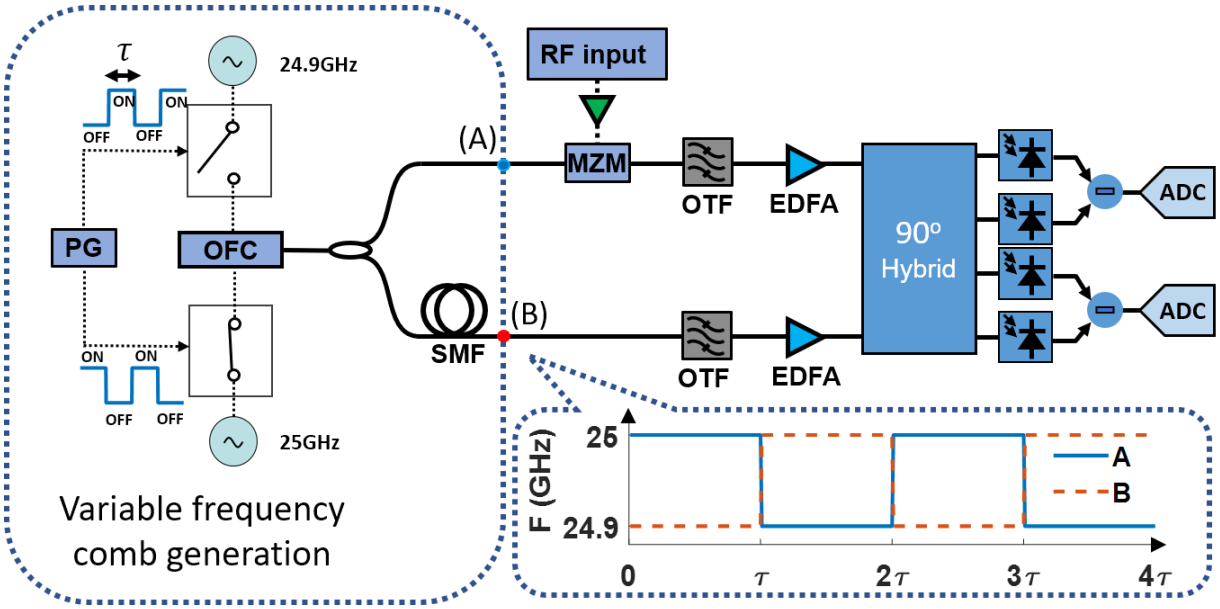

Figure. 5-8 Setups of variable frequency comb assisted CS receiver. A control signal with toggling interval τ is generated by a pulse pattern generator (PG) to control the driving clock for optical frequency comb (OFC) generation. Frequency pitch offset between two comb modes defined by two optical paths is 100 MHz at any time. OTF: optical tunable filter, EDFA: Erbium doped fiber amplifier, MZM: Mach-Zehnder modulator, SMF: single mode fiber. Inset shows the frequency pitch switching of dual comb at point A (blue solid line) and B (red-dashed line) respectively.

Subsequent to switched comb generation, 50 signal copies were created by modulating comb tones by Mach-Zehnder modulator (MZM), biased at null point. The use of single MZM for all tones mandates that modulator bias point variance across carrier wavelengths be managed. However, the architecture shown in Figure. 5-8 was specifically designed to minimize this effect, with no measurable impairment observed, similar to that reported earlier [36]. Indeed, a shifted null-point bias voltage of a signal tone yields a constant additive electric field term with modulated signal copy, allowing for simple backplane compensation for bias correction. Equally important, comb tones possessed sufficiently high OSNR and power, allows for highly linear modulation, guaranteeing low-distortion signal replication onto optical carriers.

To demonstrate the operational principle and measure DFT processor performance without fully populated backplane array, WDM block was replaced by optical tunable filter and used to sweep the band and select corresponding signal-LO tone. By repeating the receiver

stimulus, its operation was characterized using a single coherent detector rather than 50 coherent detector array, following well established methodology from lightwave transmission experiments [59], [80] and from earlier reports on physically assisted receivers [36]. At the receiver end, an ADC was used to capture the real and imaginary part of frequency-shifted version of the input RF signal. Finally, captured data were synchronized first, then digitally lowpass-filtered and down-sampled to 100 MS/s to retrieve the complex DFT coefficients with phase and power equalization using pilot symbols.

With a split-and-delay topology demonstrated here, the phase noise mainly comes from decoherence effect due to path length mismatch between signal and LO combs. To estimate the decoherence effect, the carrier phase difference during an interval τ can be modelled by a Gaussian distribution with a variance where $\delta\nu$ denotes the carrier spectral width. For 5.4 GHz channel, the measured $\sigma \approx 15^{\circ}$, which corresponds to an effective linewidth of ~1kHz. With pilot symbol deployment, the common phase error caused by phase noise can be compensated.

5.2.3 CS receiver performance

To demonstrate the operation of the new receiver, the hybrid DFT processor was used for sparse RF signal reception. As stated earlier, Ψ was pre-constructed with 640 columns selected from bandpass-filtered (3 GHz to 7.9 GHz) Gaussian distributed samples with size of 640. Each symbol lasting 10ns was constructed by selecting K columns from the basis of Ψ so that the signal was represented as $x = \Psi s$ where K indicated sparsity. The sparse signal was generated using 64 GS/s Digital-to-Analog converter (DAC) with 8-bit resolution and modulated onto the optical combs as RF input in Figure. 5-3. The hybrid comb assisted DFT engine was used to capture the DFT coefficients spanning from 3 GHz to 7.9 GHz with 100

MHz frequency spacing. Only a subset of the 50 captured DFT coefficients are used for signal recovery.

In the first set of experiments, we sent identical symbols to test the consistency of our hybrid CS receiver. Different from dual Vernier comb operation, comb frequency toggling induced a short blind period lasting about 60 ns, which was defined by the time (~50ns) required to toggle RF switch, with additional guard interval (~10ns) to account for any optical and electrical path length mismatch. The blind period comprises an effective 6% overhead of transmitted RF signals; it can be decreased in straightforward manner by increasing the duration of a switched block period and the length of SMF. Alternatively, a faster RF switch can effectively reduce the duration of the blind capture period.

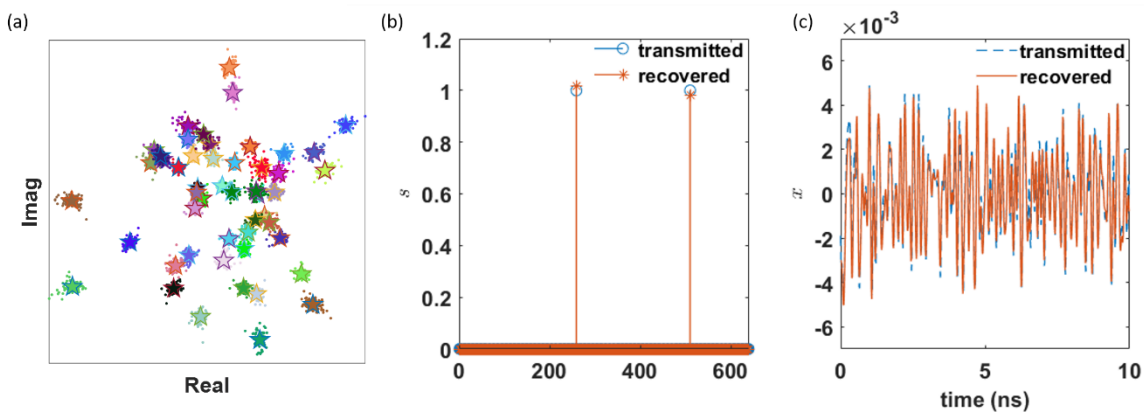

Figure. 5-9 Sparse signal recovery of identical symbols. (a)50 complex DFT coefficients of identical symbols within a frequency toggling period with sparsity $K = 2$. Distinct clusters with various colors indicate DFT coefficients at separate frequencies. Stars indicate the ideal DFT coefficients of the input RF symbol. (b) support recovery with only 17 randomly chosen DFT coefficients. Blue circles are support of transmitted symbols and red circles are recovered support. (c) waveform recovery with the 17 DFT coefficients selected in (b). blue dashed line are input symbol waveform and red solid line is the recovered waveform.

The phase shift between signal-LO tone pair was observed when comb frequency pitch was switched, causing common phase rotation over the subsequent symbols within the switched block period. To correct this discrete phase jump induced by comb toggling, as well as increase DFT precision, 4 symbols of equally distributed DFT coefficients over all 50 channels are

inserted as pilots during each switching period ($1\mu s$). For each switching period lasting $1\mu s$, 89 effective data symbols were captured. We captured 89 effective symbols within a single switching period and the extracted DFT coefficients of all 50 channels matched the ideal DFT coefficients well (Figure. 5-9 (a)). Distinct clusters with various colors indicate measured DFT coefficients at separate frequencies. We recovered support (s) and waveform (x) of one random symbol with randomly chosen 17 DFT coefficients (Figure. 5-9 (b) and (c)) with matching pursuit algorithm [117]. An excellent agreement between input and recovered signal indicated that comb assisted DFT coefficient capture had both sufficient precision and high consistency when combined with compressive sensing.

In the second set of experiments, we used the same sparse representation basis (i.e., Ψ) but each symbol had a randomly chosen support with specified K nonzeros. Four pilot symbols were inserted within every toggling period for improved accuracy of DFT coefficients measurement. Mean-square error (MSE) of recovered waveform (x) was used to characterize the CS receiver performance.

Prior to the experiment, Monte Carlo simulations were performed to test the proposed receiver performance at various sparsity (K) condition, SNR and the number of selected DFT coefficients (M) as shown in Figure. 5-10 and Figure. 5-11. In each sparsity condition, 400 symbols of randomly chosen support and additive white Gaussian noise were generated and their DFT coefficients were retrieved over all 50 channels. For each symbol, M out of the 50 DFT coefficients were selected in a random manner and the corresponding waveform was recovered. We repeated this step 10 times with various random DFT coefficients selections for each symbol and the average MSE of all 10 selections is reported as MSE here. Figure. 5-10 (a) and (b) illustrates simulated MSE over a broad range of SNR with various number of DFT

coefficients (M) for sparsity $K = 2$ and $K = 4$ respectively. With a fixed number of DFT coefficients, as SNR increased the recovery performance improved and MSE drastically dropped to yield a precise recovery. MSE did not change much by further increasing SNR in the high SNR region. In the proposed hybrid receiver, residual phase noise, as well as other system noise including shot noise and thermal noise from the receiver side, add SNR penalty to the measured DFT coefficients. However, compressed sensing algorithm is generally robust over measurement noise so that the receiver is tolerable to system noise when operating at moderate SNR conditions with enough DFT coefficients.

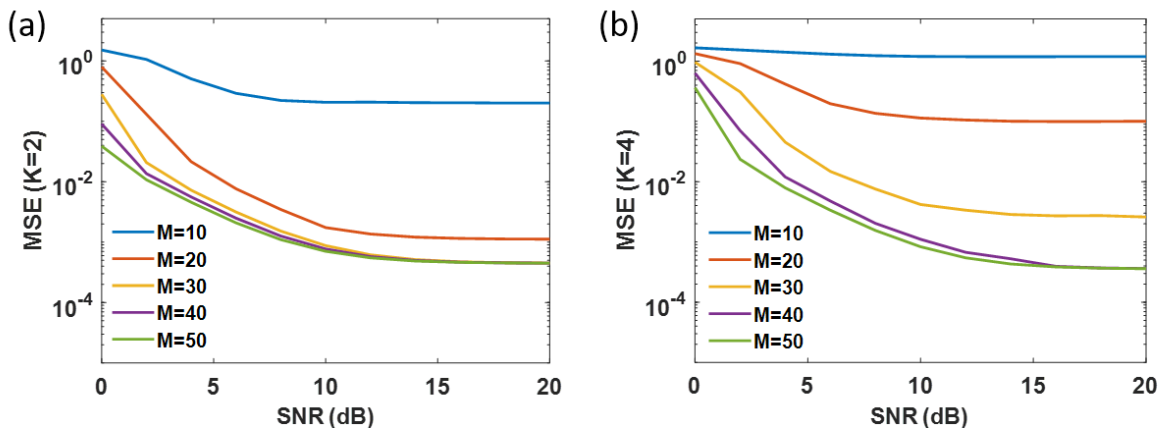

Figure. 5-10 Simulated mean square error (MSE) of the recovered waveform from proposed CS receiver at various SNR and number of DFT coefficients (M) for sparsity (a) $K = 2$ and (b) $K = 4$ respectively.

In Figure. 5-11 as sparsity K increased, more DFT coefficients are required for successful recovery, which agrees on CS theory. Noting that the recovered waveform was digitized at 640 samples per symbol, the required DFT coefficients were much less than the number of samples defined by Nyquist-sampling theory.

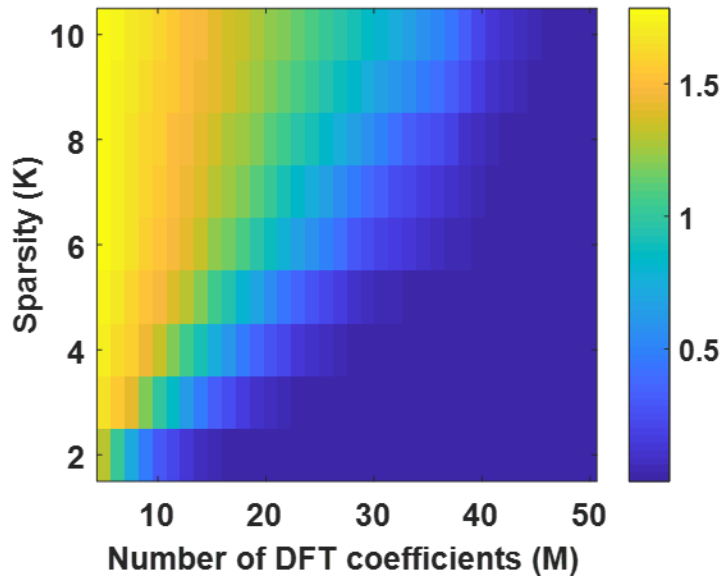

Figure. 5-11 Simulated mean square error (MSE) of the recovered waveform from proposed CS receiver at various sparsity (K) and number of DFT coefficients (M). SNR is fixed at 20dB.

Finally, we set K to 2 and 4 respectively, generating RF signal from the DAC and captured DFT coefficients over all 50 channels. For each channel, DFT coefficients of 1602 symbols were captured and post-processed offline. We used 10 randomly chosen subset of these DFT coefficients for signal waveform recovery and calculated the average MSE (Figure. 5-12). For $K = 2$, only 17 DFT coefficients, rather than all 50 DFT coefficients, were sufficient for high precision recovery, which means only 17 optical comb tones, coherent receivers, filters and corresponding ADCs are guaranteed for high precision signal reception, reducing the current physical implementation complexity to 1/3 compared to previously proposed dual-comb assisted RF receiver [20]. For $K = 4$, 25 DFT coefficients were sufficient and physical implementation complexity is reduced by half. On the other hand, compressed sensing algorithm added computation complexity in the digital domain, which can be compensated with advanced algorithms and parallel computing. In fact, with compressed sensing, the recovered waveform is even more precise than directly inverse Fourier transform the 50 captured DFT coefficients

due to inevitable spectral leakage out of the 3 to 7.9 GHz band. Calculated MSE of recovered waveform with direct inverse Fourier transform method is 0.54 and 0.49 for $K = 2$ and 4 respectively, while MSE was close to zero in both cases with CS recovery. The experimental MSE matched Monte Carlo simulation result well, proving sufficient precision of the CS receiver, which relies both on high performance comb-assisted DFT processor and robust recovery capability from compressed sensing.

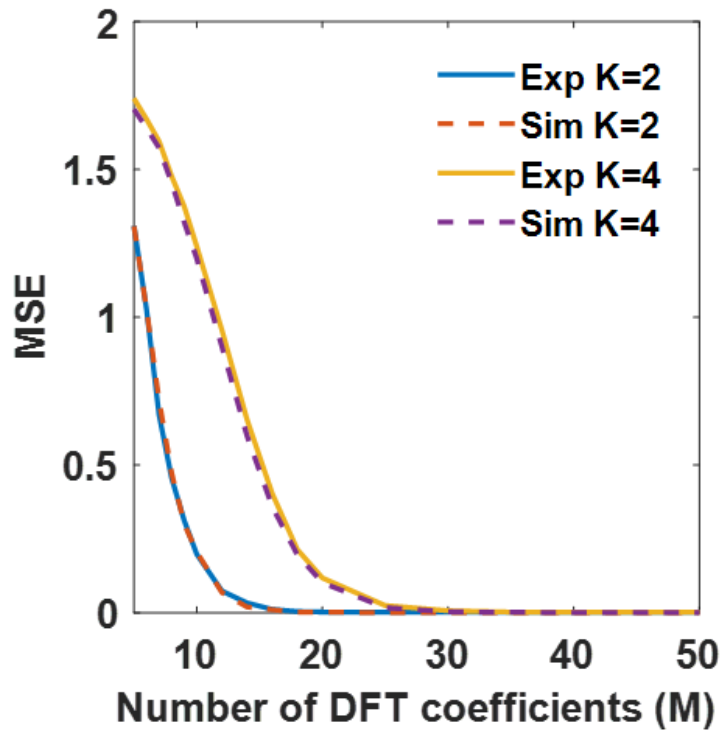

Figure. 5-12 Mean square error (MSE) vs. number of DFT coefficients for recovered signals of different sparsity (K). Solid lines indicate experimental results and dashed lines are from Monte Carlo simulations.

5.2.4 Discussion

This section describes the design and demonstration of a new class of physically-assisted wideband sub-Nyquist RF signal receiver that relies on sub-rate, high precision DFT coefficients sampling and variable-pitch frequency comb. High reception accuracy was achieved in two stages. In the first stage, high rate DFT decomposition of received RF signal was performed in

continuous capture mode by toggling the frequency of a single optical comb in split-and-delay topology. This approach allowed CS receiver to circumvent the need for high-speed electronic pattern generators or full-rate ADCs, eliminating main contributions to electronic noise and jitter in conventional techniques. In the second stage, compressed sensing techniques were applied to achieve high precision recovery of input RF signal waveform, requiring only a subset of the DFT coefficients. As a consequence, the new receiver significantly reduced the physical complexity by eliminating more than 50% of the preprocessor components, depending on the sparsity of the input signal. In the demonstration, a CS receiver was constructed and characterized by measuring MSE of recovered signal waveform. The measurements were in excellent agreement with Monte Carlo simulations, indicating that robust and accurate signal reception is viable with the new architecture. While here it was demonstrated the reception of signals within 3 GHz to 7.9 GHz band, the bandwidth of operation is mainly limited by comb frequency pitch, so that the proposed scheme is viable to scale to tens of GHz bandwidth [125] by simply using higher frequency pitch combs, without increasing hardware complexity.

5.3 Summary

This chapter describes the application of a hybrid DFT processor with reduced complexity. Firstly, a variable frequency comb assisted DFT processor with split and delay topology was proposed to replace the previous hybrid DFT processor using two mutually coherent combs. While halving the resources for dual-comb generation, the new architecture is more stable and consistent due to the fact that two combs are generated through an identical setup driven by two distinct RF oscillators. Based on this new topology, an ultra-wide-band OFDM receiver was characterized and tested using the new architecture.

Secondly, when used as a sampler in frequency domain, the new DFT engine is demonstrated in ultra-wide-band sparse signal reception combined with compressed sensing techniques. The new CS receiver directly sampled the complex DFT coefficients of UWB signals without using high-speed ADCs and only a subset of these DFT coefficients is sufficient for signal recovery. While no high bandwidth electronic components are required, the new receiver stands out with high precision and low complexity compared to conventional all-electronic and optoelectronic sub-Nyquist receivers. Besides, since only a subset of these DFT coefficients is required for successful recovery of sparse RF signals, the implementation complexity is significantly reduced compared to the standard hybrid DFT engine described previously.

Chapter 5, in part, is a reprint of the materials as it appears in *Optics Express* volume 28, issue 4, 5658 (2020), titled "Hybrid OFDM receiver assisted by a variable frequency comb" authored by Huan Hu and Stojan Radic. The dissertation author was the primary investigator and the primary author of this article.

Chapter 5, in part, is a reprint of the materials as it appears in IEEE/OSA *Journal of Lightwave Technology* early access (2020), titled "Sub-Nyquist Ultra-wideband Sparse Signal Reception via Variable Frequency Comb" authored by Huan Hu and Stojan Radic. The dissertation author was the primary investigator and the primary author of this article.

Chapter 6 Conclusion

To meet the exponentially growing trend of data traffic, current and future broadband communication systems require higher bandwidth and spectrally efficient modulation formats such as OFDM. The high-speed discrete Fourier transform processor serves as the core in OFDM, and signal processing in other broadband systems. However, it is both fundamentally and practically challenging to perform DFT operations on broadband signals with all-electronic DFT processor due to the bandwidth-precision tradeoff of electronic quantizers and fundamentally limited processing speed of conventional silicon processors. This dissertation contributes to a hybrid optical frequency combs (OFCs) assisted DFT processor, circumventing the need for high-speed quantizers and perform DFT computation in optical domain in a computation-free manner.

The principle of operation of the OFCs assisted DFT processor was introduced in Chapter 2, starting with an introduction to all-electronic digital DFT implementation. Without the need for full-rate quantization of incoming radio-frequency signals, this processor relies on dual mutually coherent, high-fidelity combs for spectral decomposition with parallel heterodyne detection and low-rate quantizers. Such OFCs are the cornerstone of the DFT processor such that the detailed theoretical background and practical implementation of parametric OFC generation through shockwave engineering is introduced in chapter 2.3.

Followed by the principle of operation, a direct experimental demonstration of the proposed hybrid DFT processor is discussed in Chapter 3. In practical scenarios, system impairments such as I-Q skew, DC offset and receiver imbalance are critical to DFT processing precision. The nonlinear response of Mach-Zehnder modulator and electrical amplifier caused distortion and had to be compensated. After compensating the experimental impairments, DFT operation on time-

limited sinc-shaped signal and binary-phase-shift-key (BPSK) signals were demonstrated. This set of experiments validate the operation of the proposed hybrid DFT processor.

It is natural to extend the application of the hybrid DFT processor to an OFDM receiver, in which DFT operation is the key functionality. As the core of this dissertation, a new wideband OFDM receiver relying on a comb assisted DFT processor is proposed and tested in Chapter 4. Without the need for high bandwidth ADCs and high-throughput, high-precision digital DFT processor, DFT generation was performed during coherent detection with two high fidelity combs, circumventing full-rate quantization. Sample-and-hold circuits were used to digitize simultaneously generated DFT coefficients and time-multiplex the output before decoding the payload. The precision of our DFT processor was first characterized by reconstructing and demodulating an 8-PPM signal under varied SNR conditions. When the new hybrid DFT processor served as a core of the OFDM receiver, phase noise due to optical tone decoherence hindered the 4-QAM modulated symbol recovery performance. To compensate the phase noise, three methods were proposed for high-performance OFDM signal demodulation. All these methods relied on the high correlation of phase noise of all channels. The sequential nulling method is easy to implement and has low complexity. However it was only applicable at high SNR conditions. To achieve robust recovery performance, two channels were set to be pilot channels and a linear estimator was used to recover phase noise of all channels but at the sacrifice of transmission rate penalty and complexity. In the end, a new joint phase noise compensation scheme was proposed, with similar performance to the pilot-aided method without pilot channels. This method was robust over all SNR conditions and easy to implement and adapt to other modulation mapping format. While no physical mechanisms were used to suppress inherent phase noise across signal-LO combs, the throughput of such (raw) OFDM

receiver can be further enhanced by deploying significantly more subcarriers and higher modulation format while maintaining flexibility and tunability.

Chapter 5 aims at reducing the implementation complexity of the DFT processor with two approaches. Firstly, the need for dual, Verniered frequency combs was eliminated by toggling the frequency of a single physical device and harnessing it in split-and-delay topology, realizing the equivalent of dual combs assisted DFT processor. The new DFT architecture using a variable frequency comb was demonstrated in a broadband OFDM receiver. This approach can be easily modified to address other applications that rely on use of dual-combs in detection ranging and spectrometry. Secondly, without the need of full spectral information, a subset of DFT coefficients was sufficient for signal reception and processing, reducing the system complexity. Based on the variable frequency comb assisted DFT processor, a new class of physically-assisted wideband sub-Nyquist RF signal receiver that relies on sub-rate, high precision DFT coefficients sampling and variable-pitch frequency comb was demonstrated. This approach allowed for a sub-Nyquist receiver to circumvent the need for high-speed electronic pattern generators or full-rate ADCs, eliminating main contributions to electronic noise and jitter in conventional techniques. With compressed sensing techniques, the new receiver significantly reduced the physical complexity by eliminating more than 50% of the preprocessor components such as filters, receivers, digitizers, etc., depending on the sparsity of input signal. Consequently, robust and accurate signal reception is viable with the new architecture.

6.1 Future work

This dissertation proposed, implemented, characterized, and improved a hybrid DFT processor and demonstrated its application in broadband RF systems. However, there are still many open questions to be answered and possible further directions.

6.1.1 OFDM receiver

In this thesis broadband OFDM receiver was demonstrated using the hybrid DFT processor relying on optical combs. The major motivation is to overcome the quantization and computation challenges for high-speed RF receivers. While the receiver was validated up to 16GHz with only tens of subcarriers, the overall throughput can be easily scaled in principle. Firstly, the bandwidth of operation can be scaled to tens of GHz with hundreds of subcarriers to achieve the full potential of optical frequency combs. Secondly, the modulation format of 4-QAM was used to simplify the analysis in this thesis. It is desirable to use advanced modulation formats such as 16-QAM, 64-QAM, and 256-QAM, which all pertain to LTE and are now being considered for the future evolution of LTE/LTE-Advanced Pro and 5G. An in-depth analysis of scaling up the throughput of the proposed OFDM receivers is highly valuable in current and future broadband systems to meet the communication data transmission growth.

To simplify the analysis of the new receiver, time and frequency synchronization are achieved in advance and minimal channel fading was held during all measurements. However, a true practical OFDM receiver is much more complex than described here and it must consider the whole signal processing pipeline such as clock recovery, time synchronization, channel estimation, etc [34]. In conventional broadband wireless communication, such a DSP pipeline has already been extensively studied based on a high-speed sampler and applying advanced DSP algorithms. Many such algorithms are considered in the frequency domain. Since in the comb-assisted OFDM receiver, the DFT coefficients rather than the temporal waveform are digitized, it is worth applying advanced frequency domain DSP algorithms to study the overall performance of the new OFDM receiver. Since the system is hybrid, consisting of both electrical

and optical components, the optimal hybrid DSP algorithm design is of both theoretical and practical impact.

6.1.2 Signal processing with machine learning and deep learning

In chapter 3 and chapter 4, the system impairments such as receiver quadrature imbalance, link nonlinearity, etc. are discussed, with a focus on phase noise compensation. While conventional signal processing techniques are viable to suppress such impairments, full compensation for system impairments with nonlinearity and memory effects is challenging and complicated. Machine learning and deep learning (ML/DL) techniques have demonstrated substantial success in a variety of applications such as computer vision, speech recognition, robotics, and autonomous driving. Compared to conventional digital signal processing techniques, ML/DL offered a more powerful approach for nonlinear statistical models. Applying machine learning and deep learning algorithms to improve the signal processing performance of the hybrid OFDM receiver is of great interest and potential.

For phase noise compensation in optical systems, previous studies show that phase noise estimation based on ML outperforms conventional time-domain approaches in the presence of moderate measurement noise [126]. More and more ML/DL approaches have been proposed to cope with the complex systematic defects in photonics systems[127]–[129]. In the area of wireless communications, ML/DL also plays an important role. For example, DL has been exploited for OFDM channel estimation and signal detection, with performance comparable to the minimum mean square error estimator and is more robust than conventional methods in scenarios with complicated channel distortion and interference[130]. The proposed hybrid OFDM receiver will benefit from state-of-the-art ML/DL techniques in both optical and wireless communication communities.

6.1.3 Spectrally sparse RF signal detection

In Chapter 5.2 a sub-Nyquist ultra-wideband sparse signal receiver was demonstrated with a comb assisted DFT processor. The successful reception relies on the fact that the incoming signal is sparse in an appropriate domain. However, when a signal is sparse in frequency domain, it is not possible to recover the waveform without fully populated detection backend, violating the purpose of system complexity reduction. When coping with spectrally sparse UWB RF signals, it is still viable to construct a receiver with dual combs. Instead of using the LO comb as multiple LO carriers, external modulation on LO comb could decompose the signal information into an appropriate domain. Recall the operation principle of hybrid DFT processor, when signal $p(t)$ is modulated on LO comb and signal $s(t)$ is modulated on the signal comb, the output after coherent detection of a signal-LO pair is $s(t) \cdot p(t)e^{j2\pi f_{IF}t}$, where f_{IF} is the frequency offset between signal and LO comb tone. The output of an array of coherent receivers is simply DFT coefficients of $s(t) \cdot p(t)$. By choosing appropriate $p(t)$ it is easy to linearly transform the spectrally sparse signal to an appropriate domain for sub-Nyquist reception. This approach is a complement for sparse UWB signal reception architecture, making the proposed comb assisted receiver suitable for arbitrary incoming sparse signals.

Chapter 7 Bibliography

[1] Index, Cisco Visual Networking, "Cisco Visual Networking Index: Forecast and Methodology, 2016–2021." [Online]. Available: https://www.cisco.com/c/en/us/solutions/collateral/service-provider/visual-networking-index-vni/complete-white-paper-c11-481360.html.

[2] I. L. Markov, "Limits on fundamental limits to computation," Nature, vol. 512, no. 7513, pp. 147–154, Aug. 2014, doi: 10.1038/nature13570.

[3] B. Murmann, "ADC Performance Survey 1997-2017." [Online]. Available: http://web.stanford.edu/~murmann/adcsurvey.html.

[4] M. A. Muriel, J. Azaña, and A. Carballar, "Real-time Fourier transformer based on fiber gratings," Opt. Lett., vol. 24, no. 1, p. 1, Jan. 1999, doi: 10.1364/OL.24.000001.

[5] M. Nakazawa, T. Hirooka, F. Futami, and S. Watanabe, "Ideal distortion-free transmission using optical Fourier transformation and Fourier transform-limited optical pulses," IEEE Photonics Technol. Lett., vol. 16, no. 4, pp. 1059–1061, Apr. 2004, doi: 10.1109/LPT.2004.824969.

[6] Guan P, Røge KM, Lillieholm M, Galili M, Hu H, Morioka T, Oxenløwe LK, "Time Lens-Based Optical Fourier Transformation for All-Optical Signal Processing of Spectrally-Efficient Data," J. Light. Technol., vol. 35, no. 4, pp. 799–806, Feb. 2017.

[7] Hillerkuss D, Winter M, Teschke M, Marculescu A, Li J, Sigurdsson G, Worms K, Ezra SB, Narkiss N, Freude W, Leuthold J, "Simple all-optical FFT scheme enabling Tbit/s real-time signal processing," Opt. Express, vol. 18, no. 9, p. 9324, Apr. 2010, doi: 10.1364/OE.18.009324.

[8] A. J. Lowery, "Design of arrayed-waveguide grating routers for use as optical OFDM demultiplexers," Opt. Express, vol. 18, no. 13, p. 14129, Jun. 2010, doi: 10.1364/OE.18.014129.

[9] Z. Wang, K. S. Kravtsov, Y.-K. Huang, and P. R. Prucnal, "Optical FFT/IFFT circuit realization using arrayed waveguide gratings and the applications in all-optical OFDM system," Opt. Express, vol. 19, no. 5, p. 4501, Feb. 2011, doi: 10.1364/OE.19.004501.

[10] H. Nejadriahi, D. HillerKuss, J. K. George, and V. J. Sorger, "Integrated All-Optical Fast Fourier Transform: Design and Sensitivity Analysis," ArXiv171102500 Phys., Oct. 2017, Accessed: Apr. 11, 2018. [Online]. Available: http://arxiv.org/abs/1711.02500.

[11] S. R. Velazquez, T. Q. Nguyen, and S. R. Broadstone, "Design of hybrid filter banks for analog/digital conversion," IEEE Trans. Signal Process., vol. 46, no. 4, pp. 956–967, Apr. 1998, doi: 10.1109/78.668549.

[12] A. Medi and W. Namgoong, “A High Data-Rate Energy-Efficient Interference-Tolerant Fully Integrated CMOS Frequency Channelized UWB Transceiver for Impulse Radio,” IEEE J. Solid-State Circuits, vol. 43, no. 4, pp. 974–980, Apr. 2008, doi: 10.1109/JSSC.2008.917513.

[13] Khilo A, Spector SJ, Grein ME, Nejadmalayeri AH, Holzwarth CW, Sander MY, Dahlem MS, Peng MY, Geis MW, DiLello NA, Yoon JU, “Photonic ADC: overcoming the bottleneck of electronic jitter,” Opt. Express, vol. 20, no. 4, pp. 4454–4469, Feb. 2012, doi: 10.1364/OE.20.004454.

[14] A. M. Fard, S. Gupta, and B. Jalali, “Photonic time-stretch digitizer and its extension to real-time spectroscopy and imaging,” Laser Photonics Rev., vol. 7, no. 2, pp. 207–263, Mar. 2013, doi: 10.1002/lpor.201200015.

[15] G. C. Valley, “Photonic analog-to-digital converters,” Opt. Express, vol. 15, no. 5, pp. 1955–1982, Mar. 2007, doi: 10.1364/OE.15.001955.

[16] D. J. Esman, A. O. J. Wiberg, N. Alic, and S. Radic, “Highly Linear Broadband Photonic-Assisted Q-Band ADC,” J. Light. Technol., vol. 33, no. 11, pp. 2256–2262, Jun. 2015.

[17] J. G. Proakis, Digital signal processing: principles algorithms and applications. Pearson Education India, 2001.

[18] C. Laperle and M. O’Sullivan, “Advances in High-Speed DACs, ADCs, and DSP for Optical Coherent Transceivers,” J. Light. Technol., vol. 32, no. 4, pp. 629–643, Feb. 2014.

[19] H. Hu, V. Ataie, E. Myslivets, and S. Radic, “Realtime Comb-Assisted Discrete Fourier Transform Processor,” in CLEO Pacific Rim Conference 2018 (2018), paper Tu2D.6, Jul. 2018, p. Tu2D.6, doi: 10.1364/CLEOPR.2018.Tu2D.6.

[20] H. Hu, V. Ataie, E. Myslivets, and S. Radic, “Optical Comb Assisted OFDM RF Receiver,” J. Light. Technol., vol. 37, no. 4, pp. 1280–1287, Feb. 2019, doi: 10.1109/JLT.2019.2892147.

[21] Y.-W. Lin, H.-Y. Liu, and C.-Y. Lee, “A 1-GS/s FFT/IFFT processor for UWB applications,” IEEE J. Solid-State Circuits, vol. 40, no. 8, pp. 1726–1735, Aug. 2005, doi: 10.1109/JSSC.2005.852007.

[22] M. Garrido, J. Grajal, M. A. Sanchez, and O. Gustafsson, “Pipelined Radix- Feedforward FFT Architectures,” IEEE Trans. Very Large Scale Integr. VLSI Syst., vol. 21, no. 1, pp. 23–32, Jan. 2013, doi: 10.1109/TVLSI.2011.2178275.

[23] S.-N. Tang, J.-W. Tsai, and T.-Y. Chang, “A 2.4-GS/s FFT Processor for OFDM-Based WPAN Applications,” IEEE Trans. Circuits Syst. II Express Briefs, vol. 57, no. 6, pp. 451–455, Jun. 2010, doi: 10.1109/TCSII.2010.2048373.

[24] E. Myslivets, B. P. P. Kuo, N. Alic, and S. Radic, “Generation of wideband frequency combs by continuous-wave seeding of multistage mixers with synthesized dispersion,” Opt. Express, vol. 20, no. 3, p. 3331, Jan. 2012, doi: 10.1364/OE.20.003331.

[25] Y. Yue, Q. Wang, and J. Anderson, “Transmitter skew tolerance and spectral efficiency tradeoff in high baud-rate QAM optical communication systems,” Opt. Express, vol. 26, no. 12, pp. 15045–15058, Jun. 2018, doi: 10.1364/OE.26.015045.

[26] E. P. da Silva and D. Zibar, “Widely Linear Equalization for IQ Imbalance and Skew Compensation in Optical Coherent Receivers,” J. Light. Technol., vol. 34, no. 15, pp. 3577–3586, Aug. 2016.

[27] T. Tanimura, S. Oda, T. Tanaka, T. Hoshida, Z. Tao, and J. C. Rasmussen, “A simple digital skew compensator for coherent receiver,” in 2009 35th European Conference on Optical Communication, Sep. 2009, pp. 1–2.

[28] M. Seimetz and C.-M. Weinert, “Options, feasibility, and availability of 2 /spl times/ 4 90/spl deg/ hybrids for coherent optical systems,” J. Light. Technol., vol. 24, no. 3, pp. 1317–1322, Mar. 2006, doi: 10.1109/JLT.2005.863251.

[29] S. H. Chang, H. S. Chung, and K. Kim, “Impact of Quadrature Imbalance in Optical Coherent QPSK Receiver,” IEEE Photonics Technol. Lett., vol. 21, no. 11, pp. 709–711, Jun. 2009, doi: 10.1109/LPT.2009.2016759.

[30] W. Gander, G. H. Golub, and R. Strebel, “Least-squares fitting of circles and ellipses,” BIT Numer. Math., vol. 34, no. 4, pp. 558–578, Dec. 1994, doi: 10.1007/BF01934268.

[31] K. M. Gharaibeh, Nonlinear Distortion in Wireless Systems: Modeling and Simulation with MATLAB. John Wiley & Sons, 2011.

[32] Jaehyok Yi, Youngoo Yang, Myungkyu Park, Wonwoo Kang, and Bumman Kim, “Analog predistortion linearizer for high-power RF amplifiers,” IEEE Trans. Microw. Theory Tech., vol. 48, no. 12, pp. 2709–2713, Dec. 2000, doi: 10.1109/22.899034.

[33] R. E. Pidgeon, “Adaptive predistortion control for optical external modulation,” US5850305A, Dec. 15, 1998.

[34] Y. G. Li and G. L. Stuber, Orthogonal Frequency Division Multiplexing for Wireless Communications. Springer, 2006.

[35] S. Roy and Chengyang Li, “A subspace blind channel estimation method for OFDM systems without cyclic prefix,” IEEE Trans. Wirel. Commun., vol. 1, no. 4, pp. 572–579, Oct. 2002, doi: 10.1109/TWC.2002.804160.

[36] D. J. Esman, V. Ataie, B. P.-P. Kuo, E. Temprana, N. Alic, and S. Radic, “Detection of Fast Transient Events in a Noisy Background,” J. Light. Technol., vol. 34, no. 24, pp. 5669–5674, Dec. 2016.

[37] K. Kikuchi and S. Tsukamoto, “Evaluation of Sensitivity of the Digital Coherent Receiver,” J. Light. Technol., vol. 26, no. 13, pp. 1817–1822, Jul. 2008.

[38] M. Sjodin, P. Johannisson, M. Karlsson, Z. Tong, and P. A. Andrekson, “OSNR Requirements for Self-Homodyne Coherent Systems,” IEEE Photonics Technol. Lett., vol. 22, no. 2, pp. 91–93, Jan. 2010, doi: 10.1109/LPT.2009.2036376.

[39] Z. Tong, A. O. J. Wiberg, E. Myslivets, B. P. P. Kuo, N. Alic, and S. Radic, “Spectral linewidth preservation in parametric frequency combs seeded by dual pumps,” Opt. Express, vol. 20, no. 16, pp. 17610–17619, Jul. 2012, doi: 10.1364/OE.20.017610.

[40] A. J. Metcalf, V. Torres-Company, D. E. Leaird, and A. M. Weiner, “High-Power Broadly Tunable Electrooptic Frequency Comb Generator,” IEEE J. Sel. Top. Quantum Electron., vol. 19, no. 6, pp. 231–236, Nov. 2013, doi: 10.1109/JSTQE.2013.2268384.

[41] E. Temprana, V. Ataie, B. P.-P. Kuo, E. Myslivets, N. Alic, and S. Radic, “Low-noise parametric frequency comb for continuous C-plus-L-band 16-QAM channels generation,” Opt. Express, vol. 22, no. 6, pp. 6822–6828, Mar. 2014, doi: 10.1364/OE.22.006822.

[42] D. Petrovic, W. Rave, and G. Fettweis, “Effects of Phase Noise on OFDM Systems With and Without PLL: Characterization and Compensation,” IEEE Trans. Commun., vol. 55, no. 8, pp. 1607–1616, Aug. 2007, doi: 10.1109/TCOMM.2007.902593.

[43] Tubbax J, Come B, Van der Perre L, Donnay S, Engels M, De Man H, Moonen M, “Compensation of IQ imbalance and phase noise in OFDM systems,” IEEE Trans. Wirel. Commun., vol. 4, no. 3, pp. 872–877, May 2005, doi: 10.1109/TWC.2004.843057.

[44] Q. Zou, A. Tarighat, and A. H. Sayed, “Compensation of Phase Noise in OFDM Wireless Systems,” IEEE Trans. Signal Process., vol. 55, no. 11, pp. 5407–5424, Nov. 2007, doi: 10.1109/TSP.2007.899583.

[45] S. L. Jansen, I. Morita, N. Takeda, and H. Tanaka, “20-Gb/s OFDM Transmission over 4,160-km SSMF Enabled by RF-Pilot Tone Phase Noise Compensation,” in Optical Fiber Communication Conference and Exposition and The National Fiber Optic Engineers Conference (2007), paper PDP15, Mar. 2007, p. PDP15, Accessed: Apr. 11, 2018. [Online]. Available: https://www.osapublishing.org/abstract.cfm?uri=NFOEC-2007-PDP15.

[46] E. Ip and J. M. Kahn, “Feedforward Carrier Recovery for Coherent Optical Communications,” J. Light. Technol., vol. 25, no. 9, pp. 2675–2692, Sep. 2007.

[47] J. Armstrong, “OFDM for Optical Communications,” J. Light. Technol., vol. 27, no. 3, pp. 189–204, Feb. 2009, doi: 10.1109/JLT.2008.2010061.

[48] Ataie V, Kuo BP, Wiberg AO, Tong Z, Huynh CH, Alic N, Radic S, “Ultrafast absolute ranging by coherent parametric comb,” in Optical Fiber Communication Conference and Exposition and the National Fiber Optic Engineers Conference (OFC/NFOEC), 2013, Mar. 2013, pp. 1–3, doi: 10.1364/OFC.2013.OTh3D.2.

[49] I. Coddington, N. Newbury, and W. Swann, “Dual-comb spectroscopy,” Optica, vol. 3, no. 4, p. 414, Apr. 2016, doi: 10.1364/OPTICA.3.000414.

[50] V. Ataie, D. Esman, B. P.-P. Kuo, N. Alic, and S. Radic, “Subnoise detection of a fast random event,” Science, vol. 350, no. 6266, pp. 1343–1346, Dec. 2015, doi: 10.1126/science.aac8446.

[51] A. Parriaux, K. Hammani, and G. Millot, “Electro-optic frequency combs,” Adv. Opt. Photonics, vol. 12, no. 1, pp. 223–287, Mar. 2020, doi: 10.1364/AOP.382052.

[52] K. Beha, D. C. Cole, P. Del’Haye, A. Coillet, S. A. Diddams, and S. B. Papp, “Electronic synthesis of light,” Optica, vol. 4, no. 4, pp. 406–411, Apr. 2017, doi: 10.1364/OPTICA.4.000406.

[53] Ishizawa A, Nishikawa T, Mizutori A, Takara H, Takada A, Sogawa T, Koga M, “Phase-noise characteristics of a 25-GHz-spaced optical frequency comb based on a phase- and intensity-modulated laser,” Opt. Express, vol. 21, no. 24, p. 29186, Dec. 2013, doi: 10.1364/OE.21.029186.

[54] L. Lundberg, M. Mazur, A. Fülöp, V. Torres-Company, M. Karlsson, and P. A. Andrekson, “Phase Correlation Between Lines of Electro-Optical Frequency Combs,” in Conference on Lasers and Electro-Optics, San Jose, California, 2018, p. JW2A.149, doi: 10.1364/CLEO_AT.2018.JW2A.149.

[55] Torres-Company Victor and Weiner Andrew M., “Optical frequency comb technology for ultra-broadband radio-frequency photonics,” Laser Photonics Rev., vol. 8, no. 3, pp. 368–393, Dec. 2013, doi: 10.1002/lpor.201300126.

[56] R. T. Watts, S. G. Murdoch, and L. P. Barry, “Phase Noise Reduction of an Optical Frequency Comb Using a Feed-Forward Heterodyne Detection Scheme,” IEEE Photonics J., vol. 8, no. 1, pp. 1–7, Feb. 2016, doi: 10.1109/JPHOT.2016.2515518.

[57] B. P. P. Kuo, E. Myslivets, N. Alic, and S. Radic, “Laser Coherence Enhancement by Extra-Cavity Parametric Mixing,” in Optical Fiber Communication Conference (2012), paper PDP5A.3, Mar. 2012, p. PDP5A.3, doi: 10.1364/OFC.2012.PDP5A.3.

[58] Schröder J, Fülöp A, Mazur M, Lundberg L, Helgason ÓB, Karlsson M, Andrekson PA, “Laser Frequency Combs for Coherent Optical Communications,” J. Light. Technol., vol. 37, no. 7, pp. 1663–1670, Apr. 2019, doi: 10.1109/JLT.2019.2894170.

[64] Lundberg L, Karlsson M, Lorences-Riesgo A, Mazur M, Schröder J, Andrekson PA, “Frequency Comb-Based WDM Transmission Systems Enabling Joint Signal Processing,” Appl. Sci., vol. 8, no. 5, p. 718, May 2018, doi: 10.3390/app8050718.

[60] I. Fatadin, D. Ives, and S. J. Savory, “Laser Linewidth Tolerance for 16-QAM Coherent Optical Systems Using QPSK Partitioning,” IEEE Photonics Technol. Lett., vol. 22, no. 9, pp. 631–633, May 2010, doi: 10.1109/LPT.2010.2043524.

[61] W. Weber, “Differential Encoding for Multiple Amplitude and Phase Shift Keying Systems,” IEEE Trans. Commun., vol. 26, no. 3, pp. 385–391, Mar. 1978, doi: 10.1109/TCOM.1978.1094074.

[62] Y. Gao, A. P. T. Lau, C. Lu, Y. Dai, and X. Xu, “Blind cycle-slip detection and correction for coherent communication systems,” in 39th European Conference and Exhibition on Optical Communication (ECOC 2013), Sep. 2013, pp. 1–3, doi: 10.1049/cp.2013.1604.

[63] T. Pfau, S. Hoffmann, and R. Noé, “Hardware-Efficient Coherent Digital Receiver Concept With Feedforward Carrier Recovery for M-QAM Constellations,” J. Light. Technol., vol. 27, no. 8, pp. 989–999, Apr. 2009.

[64] Lundberg L, Karlsson M, Lorences-Riesgo A, Mazur M, Schröder J, Andrekson PA, “Frequency Comb-Based WDM Transmission Systems Enabling Joint Signal Processing,” Appl. Sci., vol. 8, no. 5, p. 718, May 2018, doi: 10.3390/app8050718.

[65] D.-S. Ly-Gagnon, S. Tsukamoto, K. Katoh, and K. Kikuchi, “Coherent Detection of Optical Quadrature Phase-Shift Keying Signals With Carrier Phase Estimation,” J. Light. Technol., vol. 24, no. 1, p. 12, Jan. 2006.

[66] R. A. Shafik, M. S. Rahman, and A. R. Islam, “On the Extended Relationships Among EVM, BER and SNR as Performance Metrics,” in 2006 International Conference on Electrical and Computer Engineering, Dec. 2006, pp. 408–411, doi: 10.1109/ICECE.2006.355657.

[67] L. Sit, C. Sturm, T. Zwick, L. Reichardt, and W. Wiesbeck, The OFDM Joint Radar-Communication System: An Overview. 2011.

[68] D. Garmatyuk, J. Schuerger, K. Kauffman, and S. Spalding, “Wideband OFDM system for radar and communications,” in 2009 IEEE Radar Conference, May 2009, pp. 1–6, doi: 10.1109/RADAR.2009.4977024.

[69] C. H. Hwang, G. L. Lai, and S. C. Chen, “Spectrum Sensing in Wideband OFDM Cognitive Radios,” IEEE Trans. Signal Process., vol. 58, no. 2, pp. 709–719, Feb. 2010, doi: 10.1109/TSP.2009.2032453.

[70] Trocha P, Karpov M, Ganin D, Pfeiffer MH, Kordts A, Wolf S, Krockenberger J, Marin-Palomo P, Weimann C, Randel S, Freude W, “Ultrafast optical ranging using microresonator soliton frequency combs,” Science, vol. 359, no. 6378, pp. 887–891, Feb. 2018, doi: 10.1126/science.aao3924.

[71] Znakovskaya I, Fill E, Forget N, Tournois P, Seidel M, Pronin O, Krausz F, Apolonski A, “Dual frequency comb spectroscopy with a single laser,” Opt. Lett., vol. 39, no. 19, pp. 5471–5474, Oct. 2014, doi: 10.1364/OL.39.005471.

[72] N. Picqué and T. W. Hänsch, “Frequency comb spectroscopy,” Nat. Photonics, vol. 13, no. 3, p. 146, Mar. 2019, doi: 10.1038/s41566-018-0347-5.

[73] S. A. Diddams, “The evolving optical frequency comb [Invited],” JOSA B, vol. 27, no. 11, pp. B51–B62, Nov. 2010, doi: 10.1364/JOSAB.27.000B51.

[74] A. L. Gaeta, M. Lipson, and T. J. Kippenberg, “Photonic-chip-based frequency combs,” Nat. Photonics, vol. 13, no. 3, p. 158, Mar. 2019, doi: 10.1038/s41566-019-0358-x.

[75] S. T. Cundiff and J. Ye, “Colloquium: Femtosecond optical frequency combs,” Rev. Mod. Phys., vol. 75, no. 1, pp. 325–342, Mar. 2003, doi: 10.1103/RevModPhys.75.325.

[76] R. Wu, V. R. Supradeepa, C. M. Long, D. E. Leaird, and A. M. Weiner, “Generation of very flat optical frequency combs from continuous-wave lasers using cascaded intensity and phase modulators driven by tailored radio frequency waveforms,” Opt. Lett., vol. 35, no. 19, pp. 3234–3236, Oct. 2010, doi: 10.1364/OL.35.003234.

[77] T. Sakamoto, T. Kawanishi, and M. Izutsu, “Asymptotic formalism for ultraflat optical frequency comb generation using a Mach-Zehnder modulator,” Opt. Lett., vol. 32, no. 11, pp. 1515–1517, Jun. 2007, doi: 10.1364/OL.32.001515.

[78] Mishra AK, Schmogrow R, Tomkos I, Hillerkuss D, Koos C, Freude W, Leuthold J, “Flexible RF-Based Comb Generator,” IEEE Photonics Technol. Lett., vol. 25, no. 7, pp. 701–704, Apr. 2013, doi: 10.1109/LPT.2013.2249509.

[79] H.-J. Song, N. Shimizu, T. Furuta, K. Suizu, H. Ito, and T. Nagatsuma, “Broadband-Frequency-Tunable Sub-Terahertz Wave Generation Using an Optical Comb, AWGs, Optical Switches, and a Uni-Traveling Carrier Photodiode for Spectroscopic Applications,” J. Light. Technol., vol. 26, no. 15, pp. 2521–2530, Aug. 2008.

[80] Roberts K, O'Sullivan M, Wu KT, Sun H, Awadalla A, Krause DJ, Laperle C, “Performance of Dual-Polarization QPSK for Optical Transport Systems,” J. Light. Technol., vol. 27, no. 16, pp. 3546–3559, Aug. 2009.

[81] D. Esman, V. Ataie, B. P.-P. Kuo, N. Alic, and S. Radic, “Subnoise Signal Detection and Communication,” J. Light. Technol., vol. 34, no. 22, pp. 5214–5219, Nov. 2016.

[82] S. Hoyos and B. M. Sadler, “Ultra-wideband analog-to-digital conversion via signal expansion,” IEEE Trans. Veh. Technol., vol. 54, no. 5, pp. 1609–1622, Sep. 2005, doi: 10.1109/TVT.2005.856195.

[83] K. Kikuchi, T. Okoshi, M. Nagamatsu, and N. Henmi, “Degradation of bit-error rate in coherent optical communications due to spectral spread of the transmitter and the local oscillator,” J. Light. Technol., vol. 2, no. 6, pp. 1024–1033, Dec. 1984, doi: 10.1109/JLT.1984.1073700.

[84] A. Spalvieri and L. Barletta, “Pilot-Aided Carrier Recovery in the Presence of Phase Noise,” IEEE Trans. Commun., vol. 59, no. 7, pp. 1966–1974, Jul. 2011, doi: 10.1109/TCOMM.2011.051311.100047.

[85] P. Bacon, D. Fischer, and R. Lourens, “Overview of RF Switch Technology and Applications,” Microw. J., vol. 57, no. 7, pp. 76–88, Jul. 2014.

[86] J. Ge and M. P. Fok, “Ultra High-Speed Radio Frequency Switch Based on Photonics,” Sci. Rep., vol. 5, no. 1, Dec. 2015, doi: 10.1038/srep17263.

[87] T. Pollet, M. Van Bladel, and M. Moeneclaey, “BER sensitivity of OFDM systems to carrier frequency offset and Wiener phase noise,” IEEE Trans. Commun., vol. 43, no. 2/3/4, pp. 191–193, Feb. 1995, doi: 10.1109/26.380034.

[88] Songping Wu and Y. Bar-Ness, “OFDM systems in the presence of phase noise: consequences and solutions,” IEEE Trans. Commun., vol. 52, no. 11, pp. 1988–1996, Nov. 2004, doi: 10.1109/TCOMM.2004.836441.

[89] Songping Wu and Y. Bar-Ness, “A phase noise suppression algorithm for OFDM-based WLANs,” IEEE Commun. Lett., vol. 6, no. 12, pp. 535–537, Dec. 2002, doi: 10.1109/LCOMM.2002.806468.

[90] Han SH, Lee JH, “PAPR reduction of OFDM signals using a reduced complexity PTS technique,” IEEE Signal Process. Lett., vol. 11, no. 11, pp. 887–890, Nov. 2004, doi: 10.1109/LSP.2004.833490.

[91] J. Armstrong, “Peak-to-average power reduction for OFDM by repeated clipping and frequency domain filtering,” Electron. Lett., vol. 38, no. 5, pp. 246–247, Feb. 2002, doi: 10.1049/el:20020175.

[92] Shi J, Zhang J, Li X, Chi N, Zhang Y, Zhang Q, Yu J., “Improved Performance of high-order QAM OFDM Based on Probabilistically Shaping in the Datacom,” in 2018 Optical Fiber Communications Conference and Exposition (OFC), Mar. 2018, pp. 1–3.

[93] C.-T. Tsai, Y.-C. Chi, and G.-R. Lin, “Power fading mitigation of 40-Gbit/s 256-QAM OFDM carried by colorless laser diode under injection-locking,” Opt. Express, vol. 23, no. 22, p. 29065, Nov. 2015, doi: 10.1364/OE.23.029065.

[94] C. Vogel and H. Johansson, “Time-interleaved analog-to-digital converters: status and future directions,” in 2006 IEEE International Symposium on Circuits and Systems, May 2006, p. 4 pp. – 3389, doi: 10.1109/ISCAS.2006.1693352.

[95] J. W. Choi, B. Shim, Y. Ding, B. Rao, and D. I. Kim, “Compressed Sensing for Wireless Communications: Useful Tips and Tricks,” IEEE Commun. Surv. Tutor., vol. 19, no. 3, pp. 1527–1550, thirdquarter 2017, doi: 10.1109/COMST.2017.2664421.

[96] Z. Tian and G. B. Giannakis, “Compressed Sensing for Wideband Cognitive Radios,” in 2007 IEEE International Conference on Acoustics, Speech and Signal Processing - ICASSP ’07, Apr. 2007, vol. 4, p. IV-1357-IV–1360, doi: 10.1109/ICASSP.2007.367330.

[97] Z. Qin, J. Fan, Y. Liu, Y. Gao, and G. Y. Li, “Sparse Representation for Wireless Communications: A Compressive Sensing Approach,” IEEE Signal Process. Mag., vol. 35, no. 3, pp. 40–58, May 2018, doi: 10.1109/MSP.2018.2789521.

[98] Y. Yang and S. Nagarajaiah, “Output-only modal identification by compressed sensing: Non-uniform low-rate random sampling,” Mech. Syst. Signal Process., vol. 56–57, pp. 15–34, May 2015, doi: 10.1016/j.ymssp.2014.10.015.

[99] Wakin M, Becker S, Nakamura E, Grant M, Sovero E, Ching D, Yoo J, Romberg J, Emami-Neyestanak A, Candes E, “A Nonuniform Sampler for Wideband Spectrally-Sparse Environments,” IEEE J. Emerg. Sel. Top. Circuits Syst., vol. 2, no. 3, pp. 516–529, Sep. 2012, doi: 10.1109/JETCAS.2012.2214635.

[100] J. N. Laska, S. Kirolos, M. F. Duarte, T. S. Ragheb, R. G. Baraniuk, and Y. Massoud, “Theory and Implementation of an Analog-to-Information Converter using Random Demodulation,” in 2007 IEEE International Symposium on Circuits and Systems, May 2007, pp. 1959–1962, doi: 10.1109/ISCAS.2007.378360.

[101] J. A. Tropp, J. N. Laska, M. F. Duarte, J. K. Romberg, and R. G. Baraniuk, “Beyond Nyquist: Efficient Sampling of Sparse Bandlimited Signals,” IEEE Trans Inf Theor, vol. 56, no. 1, pp. 520–544, Jan. 2010, doi: 10.1109/TIT.2009.2034811.

[102] M. Mishali and Y. C. Eldar, “From Theory to Practice: Sub-Nyquist Sampling of Sparse Wideband Analog Signals,” IEEE J. Sel. Top. Signal Process., vol. 4, no. 2, pp. 375–391, Apr. 2010, doi: 10.1109/JSTSP.2010.2042414.

[103] T. Haque, R. T. Yazicigil, K. J. Pan, J. Wright, and P. R. Kinget, “Theory and Design of a Quadrature Analog-to-Information Converter for Energy-Efficient Wideband Spectrum Sensing,” IEEE Trans. Circuits Syst. Regul. Pap., vol. 62, no. 2, pp. 527–535, Feb. 2015, doi: 10.1109/TCSI.2014.2360756.

[104] D. Bellasi, L. Bettini, T. Burger, Q. Huang, C. Benkeser, and C. Studer, “A 1.9 GS/s 4-bit sub-Nyquist flash ADC for 3.8 GHz compressive spectrum sensing in 28 nm CMOS,” in 2014 IEEE 57th International Midwest Symposium on Circuits and Systems (MWSCAS), Aug. 2014, pp. 101–104, doi: 10.1109/MWSCAS.2014.6908362.

[105] Q. Guo, Y. Liang, M. Chen, H. Chen, S. Yang, and S. Xie, “Time-Interleaved 20-GHz Modulated Wideband Converter Based on Random Optical Sampling,” IEEE Photonics Technol. Lett., vol. 27, no. 9, pp. 1022–1025, May 2015, doi: 10.1109/LPT.2015.2405535.

[106] G. C. Valley, G. A. Sefler, and T. J. Shaw, “Compressive sensing of sparse radio frequency signals using optical mixing,” Opt. Lett., vol. 37, no. 22, pp. 4675–4677, Nov. 2012, doi: 10.1364/OL.37.004675.

[107] H. Nan, Y. Gu, and H. Zhang, “Optical Analog-to-Digital Conversion System Based on Compressive Sampling,” IEEE Photonics Technol. Lett., vol. 23, no. 2, pp. 67–69, Jan. 2011, doi: 10.1109/LPT.2010.2086442.

[108] J. M. Nichols and F. Bucholtz, “Beating Nyquist with light: a compressively sampled photonic link,” Opt. Express, vol. 19, no. 8, pp. 7339–7348, Apr. 2011, doi: 10.1364/OE.19.007339.

[109] Chi H, Mei Y, Chen Y, Wang D, Zheng S, Jin X, Zhang X, “Microwave spectral analysis based on photonic compressive sampling with random demodulation,” Opt. Lett., vol. 37, no. 22, pp. 4636–4638, Nov. 2012, doi: 10.1364/OL.37.004636.

[110] B. T. Bosworth and M. A. Foster, “High-speed ultrawideband photonically enabled compressed sensing of sparse radio frequency signals,” Opt. Lett., vol. 38, no. 22, pp. 4892–4895, Nov. 2013, doi: 10.1364/OL.38.004892.

[111] B. T. Bosworth, J. R. Stroud, D. N. Tran, T. D. Tran, S. Chin, and M. A. Foster, “Ultrawideband compressed sensing of arbitrary multi-tone sparse radio frequencies using spectrally encoded ultrafast laser pulses,” Opt. Lett., vol. 40, no. 13, pp. 3045–3048, Jul. 2015, doi: 10.1364/OL.40.003045.

[112] Y. Chen, H. Chi, T. Jin, S. Zheng, X. Jin, and X. Zhang, “Sub-Nyquist Sampled Analog-to-Digital Conversion Based on Photonic Time Stretch and Compressive Sensing With Optical Random Mixing,” J. Light. Technol., vol. 31, no. 21, pp. 3395–3401, Nov. 2013, doi: 10.1109/JLT.2013.2282088.

[113] G. C. Valley, G. A. Sefler, and T. J. Shaw, “Multimode waveguide speckle patterns for compressive sensing,” Opt. Lett., vol. 41, no. 11, pp. 2529–2532, Jun. 2016, doi: 10.1364/OL.41.002529.

[114] I. Haviv and O. Regev, “The Restricted Isometry Property of Subsampled Fourier Matrices,” in Geometric Aspects of Functional Analysis: Israel Seminar (GAFA) 2014–2016, B. Klartag and E. Milman, Eds. Cham: Springer International Publishing, 2017, pp. 163–179.

[115] H. Chi, Y. Chen, Y. Mei, X. Jin, S. Zheng, and X. Zhang, “Microwave spectrum sensing based on photonic time stretch and compressive sampling,” Opt. Lett., vol. 38, no. 2, pp. 136–138, Jan. 2013, doi: 10.1364/OL.38.000136.

[116] E. J. Candes and M. B. Wakin, “An Introduction To Compressive Sampling,” IEEE Signal Process. Mag., vol. 25, no. 2, pp. 21–30, Mar. 2008, doi: 10.1109/MSP.2007.914731.

[117] M. Elad, Sparse and Redundant Representations: From Theory to Applications in Signal and Image Processing. Springer Science & Business Media, 2010.

[118] M. F. Duarte, M. A. Davenport, M. B. Wakin, and R. G. Baraniuk, “Sparse Signal Detection from Incoherent Projections,” in 2006 IEEE International Conference on

Acoustics Speech and Signal Processing Proceedings, May 2006, vol. 3, p. III–III, doi: 10.1109/ICASSP.2006.1660651.

[119] M. Aharon, M. Elad, and A. Bruckstein, "$rm K$-SVD: An Algorithm for Designing Overcomplete Dictionaries for Sparse Representation," IEEE Trans. Signal Process., vol. 54, no. 11, pp. 4311–4322, Nov. 2006, doi: 10.1109/TSP.2006.881199.

[120] Z. Zhang, Y. Xu, J. Yang, X. Li, and D. Zhang, "A Survey of Sparse Representation: Algorithms and Applications," IEEE Access, vol. 3, pp. 490–530, 2015, doi: 10.1109/ACCESS.2015.2430359.

[121] S. Mallat and Z. Zhang, "Matching pursuits with time-frequency dictionaries," IEEE Trans Signal Process., vol. 41, no. 12, pp. 3397–3415, 1993, doi: 10.1109/78.258082.

[122] Y. C. Pati, R. Rezaiifar, and P. S. Krishnaprasad, "Orthogonal matching pursuit: recursive function approximation with applications to wavelet decomposition," in Proceedings of 27th Asilomar Conference on Signals, Systems and Computers, Nov. 1993, pp. 40–44 vol.1, doi: 10.1109/ACSSC.1993.342465.

[123] D. Needell and J. A. Tropp, "CoSaMP: Iterative signal recovery from incomplete and inaccurate samples," Appl. Comput. Harmon. Anal., vol. 26, no. 3, pp. 301–321, May 2009, doi: 10.1016/j.acha.2008.07.002.

[124] D. L. Donoho, "Compressed sensing," IEEE Trans Inf. Theory, vol. 52, pp. 1289–1306, 2006.

[125] Xu X, Wu J, Nguyen TG, Chu ST, Little BE, Morandotti R, Mitchell A, Moss DJ., "Broadband RF Channelizer Based on an Integrated Optical Frequency Kerr Comb Source," J. Light. Technol., vol. 36, no. 19, pp. 4519–4526, Oct. 2018, doi: 10.1109/JLT.2018.2819172.

[126] Zibar D, de Carvalho LH, Piels M, Doberstein A, Diniz J, Nebendahl B, Franciscangelis C, Estaran J, Haisch H, Gonzalez NG, de Oliveira JC., "Application of Machine Learning Techniques for Amplitude and Phase Noise Characterization," J. Light. Technol., vol. 33, no. 7, pp. 1333–1343, Apr. 2015.

[127] D. Zibar, M. Piels, R. Jones, and C. G. Schäeffer, "Machine Learning Techniques in Optical Communication," J. Light. Technol., vol. 34, no. 6, pp. 1442–1452, Mar. 2016, doi: 10.1109/JLT.2015.2508502.

[128] C. Häger and H. D. Pfister, "Deep Learning of the Nonlinear Schrödinger Equation in Fiber-Optic Communications," in 2018 IEEE International Symposium on Information Theory (ISIT), Jun. 2018, pp. 1590–1594, doi: 10.1109/ISIT.2018.8437734.

[129] S. Xu, X. Zou, B. Ma, J. Chen, L. Yu, and W. Zou, "Deep-learning-powered photonic analog-to-digital conversion," Light Sci. Appl., vol. 8, no. 1, p. 66, Dec. 2019, doi: 10.1038/s41377-019-0176-4.

[130] H. Ye, G. Y. Li, and B. H. Juang, “Power of Deep Learning for Channel Estimation and Signal Detection in OFDM Systems,” IEEE Wirel. Commun. Lett., vol. 7, no. 1, pp. 114–117, Feb. 2018, doi: 10.1109/LWC.2017.2757490.